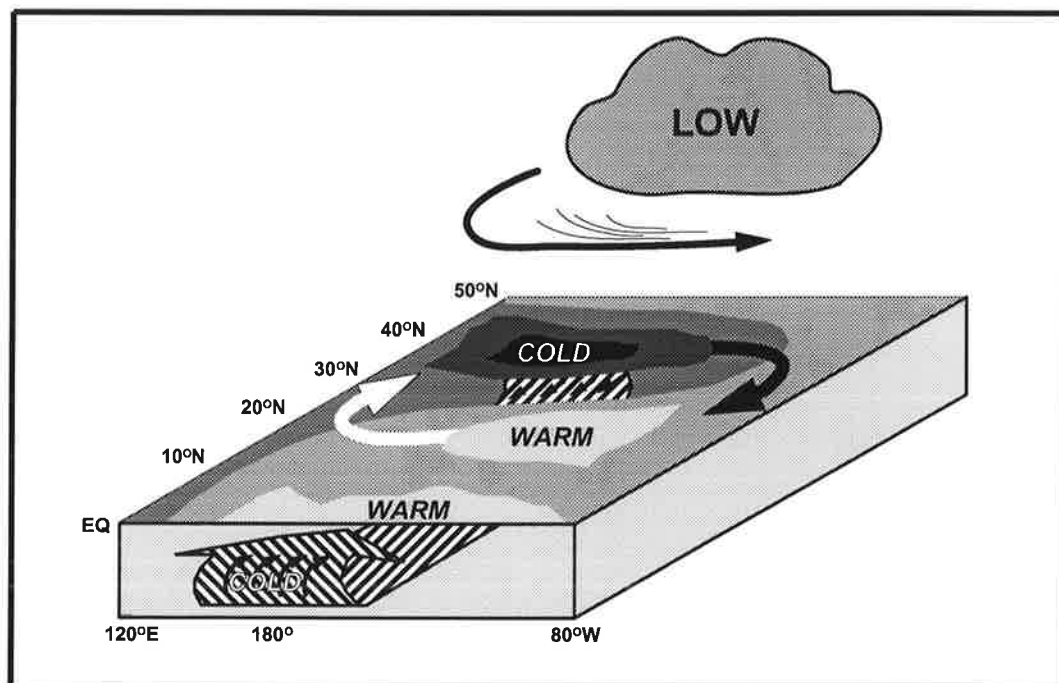




# Max-Planck-Institut für Meteorologie

## EXAMENSARBEIT Nr. 63



## OCEAN-ATMOSPHERE INTERACTIONS ON DECADAL TIMESCALES

VON

Stephan Venzke

HAMBURG, Januar 1999

Dissertation zur Erlangung des Doktorgrades

Autor:

Stephan Venzke

Max-Planck-Institut  
für Meteorologie

MAX-PLANCK-INSTITUT  
FÜR METEOROLOGIE  
BUNDESSTRASSE 55  
D - 20146 HAMBURG  
GERMANY

Tel.: +49-(0)40-4 11 73-0  
Telefax: +49-(0)40-4 11 73-298  
E-Mail: <name> @ dkrz.de



# Ocean-atmosphere interactions on decadal timescales

Dissertation  
zur Erlangung des Doktorgrades  
der Naturwissenschaften im Fachbereich  
Geowissenschaften  
der  
Universität Hamburg

vorgelegt  
von  
Stephan Venzke  
aus Ahrensböök

Hamburg  
1999

**ISSN 0938-5177**



## Abstract

In this thesis, different processes that might contribute to the generation of decadal climate variability were investigated using general circulation models (GCMs) of the atmosphere and the ocean. First, the sensitivity of the atmospheric circulation to decadal changes in the underlying sea surface temperatures (SSTs) was estimated from an ensemble of six integrations of the Hadley Centre atmospheric GCM HadAM1, all forced by observed SSTs and sea-ice extents for the period 1949-93. Using a novel approach to estimate the 'true' SST-forced atmospheric response in the presence of spatially correlated internal atmospheric variability, the decadal atmospheric variability was studied over the North Atlantic and North Pacific regions. After filtering out the atmospheric circulation changes associated with the El Niño - Southern Oscillation (ENSO) phenomenon, the dominant mode of forced variability over the North Atlantic exhibits a meridional dipole in the mean sea level pressure (MSLP) field and is related to a tripole in the anomalous North Atlantic SSTs. Over large parts of the North Atlantic region, however, the atmospheric response is not consistent enough to provide feedbacks to the underlying ocean that could cause self-sustained decadal oscillations. Over the North Pacific the atmospheric response is dominated by ENSO. In addition to the ENSO-related response an independent decadal atmospheric signal was detected. It consistently involves large-scale wind stress curl anomalies over the North Pacific region. The effect of such wind stress curl anomalies on the ocean was studied in the second part of this thesis using the Hamburg Ocean Primitive Equation model (HOPE). It is shown how the adjustment of the North Pacific gyre circulation to large-scale wind stress curl anomalies determines the decadal timescale and how it may be exploited for predictions of decadal upper-ocean temperature changes in the central North Pacific. The HOPE model was also used to investigate a mechanism for the generation of decadal climate variability in the tropical Pacific which relies on subduction of midlatitudinal North Pacific SST anomalies and their equatorward propagation within the oceanic thermocline. It is demonstrated that such a mechanism is unlikely to cause decadal climate variability in the tropical Pacific.



## Acknowledgements

At the Max-Planck-Institut für Meteorologie I found excellent conditions for working in climate research. I wish to thank Prof. Klaus Hasselmann for giving me the opportunity to prepare this thesis in his department. I am grateful to my supervisor Mojib Latif for his guidance and advice throughout my research. I would also like to thank Prof. Hartmut Graßl, who agreed to be the co-examiner of this dissertation, and Ernst Maier-Reimer, who developed the HOPE model and helped me to set it up. The promotion of my summer-project in Oxford by David Anderson and Chris Folland as well as the support of the Studienstiftung and the DAAD are also very much appreciated.

Furthermore, I would like to thank my friends and colleagues who contributed in one way or the other to this thesis: Without the scientific and technical advice of Matthias I often would have been completely lost. His comments on the manuscript were also very useful. Willi was always there to help and frequently reminded me when it was time for lunch. I enjoyed many interesting discussions with Anselm, Axel and Christian. The collaboration with Myles, Rowan and Dave was extremely fruitful. Niklas' thorough analysis of observed ocean temperatures was essential to confirm the results of my simulations. Keith helped me with various scientific and language problems. Gerrit and Detlev kept on asking the difficult questions. Norbert and Joachim not only provided graphical assistance, but they and all the other teammates from the *Max-Planck-Betriebssportmannschaft* also showed me that men and football belong together. Hans kept the team going. In tough times, the friendship of Marcüse, Paul, Øley, Martin, Falk and Scheiti proved to be especially valuable. Most of all, however, I thank my wife Anja for always being there for me with her love, support and encouragement through all the ups and downs in the course of this work, and my parents for their confidence in me.

# Contents

<b>1</b>	<b>Introduction</b>	<b>1</b>
<b>2</b>	<b>Atmospheric model experiments</b>	<b>6</b>
2.1	Experimental design and data processing . . . . .	7
2.2	Detection of SST-forced variability . . . . .	9
2.3	The response over the North Atlantic . . . . .	12
2.3.1	Limitations of conventional methods . . . . .	12
2.3.2	Application of the optimal detection algorithm . . . . .	15
2.3.3	Comparison with observations . . . . .	20
2.3.4	Spatial characteristics of the response . . . . .	23
2.4	The response over the North Pacific . . . . .	28
2.4.1	ENSO-related atmospheric variability . . . . .	29
2.4.2	ENSO-independent atmospheric response . . . . .	32
<b>3</b>	<b>Ocean model experiments</b>	<b>38</b>
3.1	Dynamics of the subtropical gyre circulation . . . . .	39
3.1.1	The steady circulation . . . . .	39
3.1.2	The spin-up . . . . .	42
3.2	Ocean model and experimental design . . . . .	44
3.2.1	The ocean model . . . . .	44
3.2.2	Atmospheric forcing . . . . .	46
3.3	Decadal gyre circulation changes . . . . .	49
3.3.1	Spin-up by suddenly applied anomalous wind stress . . . . .	49
3.3.2	North Pacific response to decadal wind stress changes . . . . .	51
3.3.3	Predictability of observed decadal North Pacific temperature changes . . . . .	56
3.4	Decadal coupling via the oceanic thermocline . . . . .	66

<i>CONTENTS</i>	iii
3.4.1 Maps of potential vorticity . . . . .	66
3.4.2 Propagation of diabatically forced temperature anomalies . . . . .	69
3.4.3 Observational findings and sensitivity study . . . . .	73
<b>4 Summary, conclusions, and outlook</b>	<b>79</b>
<b>A The optimal detection algorithm</b>	<b>85</b>

# Chapter 1

## Introduction

Evidence for human awareness of decadal climate variations can be found in records from more than three thousand years ago:

*"Seven years of great abundance are coming throughout the land of Egypt, but seven years of famine will follow them."* (1.Moses, 41)

Recognising the danger of decade-long droughts, the ancient Jewish nation stored food in the good (wet) years in reserve for bad (dry) years. Although people have been concerned about climate fluctuations since so many centuries, the mechanisms giving rise to decadal climate variations are still poorly understood.

In general, climate variability is generated by astronomical processes external to the earth's climate system as well as a complex interplay of the different internal components of the earth's climate system: the atmosphere, the oceans, the cryosphere, the lithosphere and the biosphere. Each of these is relevant for a different range of time and space scales. Changes in one subsystem may eventually affect all other parts of the climate system, and feedback processes from the slower subsystems, such as the oceans and the glaciers, can initiate fluctuations with a long timescale in the faster subsystems, such as the atmosphere. In fact, these feedback mechanisms may lead to climatic cycles on different timescales. Only when we identify these cycles and understand the governing physical processes leading to them are we able to make forecasts about long-term changes in a key variable like precipitation which for millions of people is still as crucial as it was for the people of Egypt three and a half thousand years ago.

Various hypotheses have been put forward to explain the observed climate variability. Neither the search for external forcing mechanisms (e.g White et al., 1997; Lean et al., 1995; Robock and Mao, 1995) nor the search for non-linear interac-

tions in individual subsystems (e.g. James and James, 1989; Yin and Sarachik, 1995) have been convincingly successful in explaining the general characteristics of the spectra of observed variability. The most successful theory for the generation of climate variability to date is the stochastic climate model scenario introduced by Hasselmann (1976). It may be regarded as the null hypothesis for the generation of climate variability in general and decadal variability in particular. Slow changes of the climate system are explained as the integral response to continuous random excitation by short period “weather” disturbances. The coupled ocean-atmosphere-cryosphere-land system is divided into a rapidly varying *weather* system (essentially the atmosphere) and a slowly responding *climate* system (the ocean, cryosphere, land vegetation etc.). The main idea is that the climate system acts as an integrator of the short-period weather excitation and thereby exhibits the same random-walk response characteristics as large particles interacting with an ensemble of much smaller particles in the analogous Brownian motion problem (e.g. Wang and Uhlenbek, 1945). One may view the sea surface temperature (SST) variability, for instance, as the result of the integration of surface heat flux anomalies within the oceanic mixed layer. The stochastic climate model predicts red variance spectra, in qualitative agreement with observations: The temporal evolution of a typical oceanic quantity  $y$  (such as SST) may be described by a Langevin equation

$$\frac{dy(t)}{dt} = -\lambda y(t) + \zeta(t) \quad (1.1)$$

with  $\lambda$  representing a damping parameter and  $\zeta$  the atmospheric forcing that is assumed to be white noise. Within the concept of the stochastic climate model the oceanic response  $G(\omega)$  is given by

$$G(\omega) = \frac{\sigma^2}{\lambda^2 + \omega^2} \quad (1.2)$$

Here,  $\omega$  denotes the frequency and  $\sigma$  the standard deviation of the white noise forcing. Fig. 1.1a shows schematically the variance spectra that result from this simplest version of the stochastic climate model. The spectral density of the atmospheric forcing (white noise)  $F(\omega)$  does not depend on frequency. The oceanic response  $G(\omega)$  is red, with a slope  $\omega^{-2}$  down to a frequency that depends on the damping  $\lambda$ . At frequencies lower than  $\lambda$  the oceanic spectrum is flat (white).

Substantial deviations from this null hypothesis of climate variability can be found also. It has been shown that peaks in the spectra can also be explained by the stochastic climate model concept when resonant interactions between the ocean and

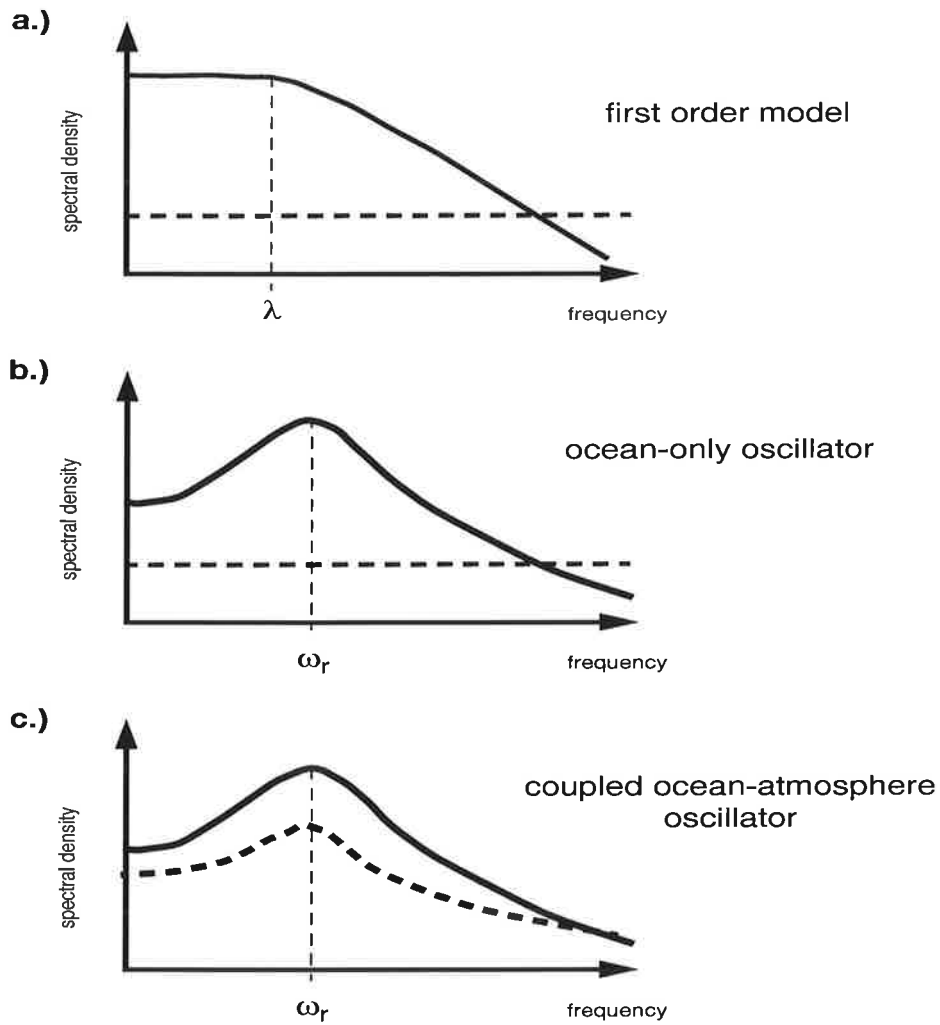


Figure 1.1: Schematic variance spectrum of input  $F(\omega)$  (dashed line) and response  $G(\omega)$  (solid line) according to (a) the simplest version of the stochastic climate model, (b) the stochastically forced harmonic oscillator and (c) the coupled ocean-atmosphere oscillator.

the atmosphere play a key role (e.g. Mikolajewicz and Maier-Reimer, 1990) and damped eigenoscillations of the climate system are excited by the stochastic forcing. A good prototype for such a scenario is the damped stochastically forced harmonic oscillator

$$\frac{d^2y(t)}{dt^2} + \lambda \frac{dy(t)}{dt} + \omega_0^2 y(t) = \zeta(t) \quad (1.3)$$

Here,  $\omega_0$  is the eigenfrequency of the free undamped harmonic oscillator. The oceanic response  $G(\omega)$  is given by

$$G(\omega) = \frac{\sigma^2}{(\omega^2 - \omega_0^2)^2 + \omega^2 \lambda^2} \quad (1.4)$$

Such a generalised concept yields peaks at resonant frequencies

$$\omega_r = \sqrt{\omega_0^2 - \frac{\lambda^2}{2}} \quad (1.5)$$

Hence, around  $\omega_r$  the spectral density of a climate variable (such as SST) will be higher than that predicted by the simple stochastic climate model, while the atmospheric spectrum is still white (Fig. 1.1b). In both the simple version of the stochastic climate model and the stochastically forced harmonic oscillator, there may be a weak feedback from the slow climate component to the atmosphere but it is needed to sustain the oscillation.

This also applies to the concept that was recently articulated by Saravanan and McWilliams (1998). Following the ideas of Lemke et al. (1980) and Frankignoul and Reynolds (1983), they developed a simple analytical one-dimensional stochastic model of the interaction between spatially coherent but temporarily white atmospheric forcing and an advective ocean. Their simple ocean-atmosphere system shows enhanced variability on preferred timescales, although there is no underlying oscillatory mechanism. The timescale is determined by both the advective velocity of the upper ocean and the length scale associated with the atmospheric variability. There are, however, other types of climate oscillations which require a consistent feedback from the slow climate component to the atmosphere. The most prominent example of such a climate oscillation relying on two way ocean-atmosphere interactions is the El Niño/Southern Oscillation (ENSO) phenomenon, which is the dominant source of climate fluctuation on interannual timescales. The dynamics of ENSO are meanwhile fairly well understood (see Philander, 1990, and Neelin et al., 1994, for an introduction and overview of research activities). Extra-tropical ocean-atmosphere interactions were already studied by Bjerknes in 1964, but they have only recently been suggested as a possible origin for decadal climate variability (Latif and Barnett, 1994; Gu and Philander, 1997; Grötzner et al., 1998). The spectra resulting from a coupled ocean-atmosphere mode, in which the state of the ocean and the atmosphere are controlled by the boundary conditions given by the respective other component, is shown in Fig. 1.1c. Enhanced spectral density at a certain frequency is found in both the ocean and the atmosphere. The main objective of this thesis is to study a variety of physical processes in the ocean-atmosphere system that may generate this kind of decadal climate variability.

The coupled scenario is most interesting in terms of long-term climate predictions, as it implies that decadal climate fluctuations are mostly deterministic. It would

allow one to predict long-term atmospheric changes, which is highly relevant to society. Predictability could arise from the influence of ocean dynamics on the SST and the subsequent influence of the SST changes on the atmosphere. During El Niño, for example, the behaviour of the atmosphere can be fairly well predicted in many regions.

As observations covering a multi-decadal period are sparse, coupled ocean-atmosphere general circulation models (GCMs) are often used to get further insight into possible mechanisms that may give rise to decadal climate variability. Numerical integrations with these models provide multi-century long consistent data sets which are not available from the real world. Nevertheless, they share one deficiency with observations: both do not allow for conclusions about cause and effect within ocean-atmosphere interactions. These can be better resolved in separate integrations of the individual subsystems.

In this thesis, first the atmospheric response to observed decadal SST changes in the North Atlantic and Pacific regions is discussed on the basis of results from an ensemble of multi-decadal atmospheric GCM runs. The dynamics which govern the oceanic variability on decadal timescales are then addressed using integrations of an oceanic GCM of the Pacific Ocean. In the final chapter the main findings are summarised and conclusions are drawn in reply to the central question of this thesis: How do ocean-atmosphere interactions contribute to the generation of decadal climate fluctuations ?

## Chapter 2

# Atmospheric model experiments

A coupled ocean-atmosphere mode of climate variability requires a consistent atmospheric response to changes in the underlying SSTs. In the tropical Pacific, atmosphere and ocean act in concert to maintain a coupled process (ENSO) generating interannual climate fluctuations. A theoretical explanation for the ENSO phenomenon was first given by Bjerknes (1966, 1969). It was also Bjerknes (1964) who performed a pioneering study of extra-tropical air-sea interactions. Following his early ideas, Latif and Barnett (1994) proposed a mechanism for decadal variability in the North Pacific, in which the atmospheric response involves surface heat flux anomalies producing a positive feedback on SST anomalies and anomalies in wind stress curl producing a delayed negative feedback via adjustment of the subtropical gyre circulation, with the delay time set by the propagation of baroclinic Rossby waves across the ocean basin. Grötzner et al. (1998), studying the Atlantic variability in the same coupled model integration found a similar mechanism as Latif and Barnett (1994). They furthermore noted that advection in the ocean could be as important as Rossby wave adjustment in providing the delayed negative feedback.

The decisive factor that allows one to discriminate between the uncoupled and coupled scenarios is the nature of the atmospheric response to the underlying SST anomalies. The coupled scenario places stringent requirements on the characteristics of the response. First, it must be sufficiently strong, so that the atmosphere's influence on the ocean is not dominated by the internal atmospheric variability. Secondly, it must involve changes in surface wind stress and/or heat flux that have an appropriate form to provide a feedback that will change, with a lag, the SST anomaly to which the atmosphere is responding.

The nature of the atmospheric response to various idealised extra-tropical SST

anomalies has been investigated in several model studies (Palmer and Sun, 1985; Pitcher et al., 1988; Kushnir and Held, 1996; Peng et al., 1997). The results from these studies are not consistent with each other in all respects, but tend to suggest that the response is rather weak relative to the internal variability. Fixed idealised SST anomalies do not allow a realistic estimate of the strength of the response compared to the internal atmospheric variability. To estimate the atmospheric response reliably one needs an ensemble of atmospheric GCM integrations forced by observed SSTs, which provides information about the spatio-temporal structure of the forced response and the internal variability. In this way, however, it becomes harder to distinguish between the forced response and the internal atmospheric variability. Hasselmann (1979) suggested treating the problem of identifying the mean atmospheric response to external forcing in the presence of natural variability of the atmosphere as a pattern-detection problem. This idea was further developed into “optimal fingerprinting” used for the detection of a given time-dependent climate change signal in the presence of natural climate variability noise (Hasselmann, 1993). Allen and Smith (1996, 1997) recently presented a generalization of principal component (or singular spectrum) analysis (PCA or SSA) which yields an optimal multivariate filter to discriminate between a signal and some arbitrary colored noise. Their ideas are based on those of Hasselmann (1979, 1993), generalised to the situation in which one does not know the spatio-temporal characteristics of the response pattern one is looking for.

In this chapter, an ensemble of multi-decadal atmospheric GCM runs forced by observed SSTs is used in conjunction with an optimal detection algorithm to study the atmospheric response over the North Atlantic and North Pacific sectors to observed decadal SST changes.

## 2.1 Experimental design and data processing

The GCM used in this study is known as HadAM1, the version of the Hadley Centre Atmosphere Model that was submitted to the Atmospheric Model Intercomparison Project (AMIP – Gates, 1992). It is a gridpoint model with a horizontal resolution of  $2.5^\circ$  latitude by  $3.75^\circ$  longitude and 19 hybrid levels in the vertical. Physical parametrisations include: a gravity wave drag scheme; a radiation scheme which computes fluxes in four long-wave bands and six short-wave bands and responds to prognostic cloud variables; a penetrative convection scheme with stability-dependent

closure and a land surface scheme. Further details about the model development and the physics and dynamics of the precise version used here are given by Cullen (1993) and Phillips (1994).

The simulations used here are the same six-member ensemble employed by Rowell (1998) and Davies et al. (1998). Each member was integrated from 1st October 1948 to 1st December 1993 with lower boundary forcing supplied by version 1.1 of the specifically-designed GISST (Global sea-Ice and Sea Surface Temperature) data set, described by Parker et al. (1995). The initial atmospheric state and surface temperatures were taken from UK Meteorological Office analyses for six different dates, arbitrarily chosen, but all close to October 1st. Soil moisture and snow depth were initialised from an adaption of the Willmott et al. (1985) climatology. Due to likely spin-up effects, the first two months of each integration were discarded, leaving a set of six integrations, each 45 years long (December 1st 1948 – November 30th 1993), giving a total of 270 years of model data.

Whether the model's response to SST is realistic or not depends in part on the accuracy of various aspects of its climatology. The climatologies of model variables of interest in this study were computed for each month by averaging that month over all 270 model years. As shown by Davies et al. (1998), the seasonal ensemble mean climatology of mean sea level pressure (MSLP) compared very well with that inferred from the observational data set of Basnett and Parker (1995).

Monthly anomalies have been obtained by subtracting the climatology from the monthly data. Standard seasonal means (DJF, MAM, JJA, SON) were constructed by averaging over three-month periods, and each season has been analysed separately. Since the focus in this thesis is on low frequency atmospheric changes, this timescale has been emphasised by removing any linear trend and smoothing each set of seasonal means with a three-point (i.e. 3-year) running mean filter.

Most studies of coupled air-sea modes in midlatitudes restrict their analyses to wintertime when the oceanic mixed layer is deepest and SST anomalies are most likely to express deeper subsurface anomalies (e.g. Deser and Blackmon, 1993; Grötzner et al., 1998; Sutton and Allen, 1997; Latif and Barnett, 1994). Studies of seasonal predictability over the North Atlantic and European region by Davies et al. (1998) as well as Palmer and Anderson (1994), however, have suggested that the MSLP predictability may be higher in spring (MAM) than in winter (DJF). Therefore, the focus will be on winter (DJF) as well as spring (MAM) data.

## 2.2 Detection of SST-forced atmospheric variability

In this section a technique is presented which allows one to characterise the time-varying atmospheric response to a time-varying external forcing in a system which is subject to internal chaotic variability. The exact derivation of the algorithm is given in the appendix.

The *forced response* is defined here as the component of the evolution of the system which is determined by the external forcing, independent of the initial conditions, and would therefore be common to all members of a hypothetical infinite ensemble. If such an infinite ensemble were available, the forced response would simply be the time-varying component of the ensemble mean. As only finite ensembles (here with only six members) are available, one needs to make the most efficient use of the information provided by this relatively small ensemble that displays substantial inter-member variability.

At this point it shall be noted that not all possible atmospheric responses to SST and sea-ice forcing would be captured by the above definition of the forced response. It is assumed that, on the timescales of interest, the data may be treated as a linear superposition of a deterministic and predictable forced response with additive internal variability. This picture is clearly incomplete, since in a non-linear system the internal variability and forced response can interact. For example, the response to a particular pattern of SST anomalies could be enhanced variability in the storm track accompanied by little change in the mean flow. However, focusing on the first-order response seems a logical starting point.

In the language of weather regimes (e.g. Lorenz, 1963; Robertson et al., 1998; Renshaw et al., 1998), the first-order forced response corresponds to either (a) changes in the characteristics of the regimes themselves, or perhaps more likely (b) changes in the fraction of time the system spends in particular regimes, in response to changes in the state (or phase) of the external forcing. Note that the definition of the forced response is applicable regardless of whether the response consists in the excitation of a pre-existing mode of internal variability or the generation of a new mode.

Since the seasonal means were sampled annually the *atmospheric noise* (internal variability which is independent of SST and sea ice forcing) can be assumed to be uncorrelated in time: each season is effectively independent of the same season the following year. This noise is, however, highly correlated in space – that is, certain

spatial patterns contain much more internal variability than others.

The signal-to-noise analysis has largely been formulated in previous studies in terms of individual gridpoint statistics using e.g. the Analysis of Variance (ANOVA) approach (Davies et al., 1998; Rowell, 1998), rather than the pattern response. The question of whether or not the response pattern as a whole is statistically significant can not be resolved by such an approach. According to Hasselmann (1979), it is necessary to regard the signal and the noise fields as multi-dimensional vector quantities and to carry out the significance analysis with respect to this multi-variate field, rather than in terms of individual gridpoint statistics.

The data in the  $k^{\text{th}}$  ensemble member is therefore represented as the matrix  $\mathbf{X}_k$ , where  $X_{ijk}$  is the DJF or MAM seasonal mean at spatial location  $i$  ( $i = 1, \dots, \ell$ ) in year  $j$  ( $j = 1, \dots, m$ ) from ensemble-member  $k$  ( $k = 1, \dots, n$ ). The seasons are analysed independently, so  $m$  is the number of years in the series.

Each ensemble member  $\mathbf{X}_k$  is decomposed into the ensemble-mean component  $\mathbf{X}_M$  and the departures from that mean,  $\mathbf{X}_{Nk}$ :

$$\mathbf{X}_k = \mathbf{X}_M + \mathbf{X}_{Nk}. \quad (2.1)$$

By definition, the forced response discussed above,  $\mathbf{X}_F = \mathcal{E}(\mathbf{X}_M)$ , where the expectation operator refers to an average taken over an hypothetical infinite ensemble, not over time.  $\mathbf{X}_F$  is therefore time-dependent, having the same dimensions as the  $\mathbf{X}_k$ . The ensemble mean,  $\mathbf{X}_M$ , is the best estimate one has of the full spatio-temporal evolution of the forced response, but it will be heavily contaminated by noise due to the small size of the ensemble. This is illustrated in Fig. 2.1.

Estimating the dominant mode of the forced response from the ensemble mean in terms of Empirical Orthogonal Functions (EOFs – Lorenz, 1956), the obtained leading EOF of the ensemble mean will be biased towards the direction of the leading EOF of the noise. It is therefore not the best estimate for the true forced response but is governed by the dominant internal variance pattern, as formally derived in the appendix.

The aim of the algorithm summarised below is to identify the dominant characteristics of  $\mathbf{X}_F$  despite the noise-contamination of the ensemble mean. This is achieved as follows:

First, the fields of  $\mathbf{X}_{Nk}$  are appended to a set of  $6 \times 45 = 270$  fields making up  $\mathbf{X}_N$  which provides an estimate of the internal atmospheric variability. On this data set  $\mathbf{X}_N$  an EOF analysis is performed by using singular value decomposition (SVD):

$$\mathbf{X}_N = \mathbf{E}_N \mathbf{\Lambda}_N \mathbf{P}_N^T, \quad (2.2)$$

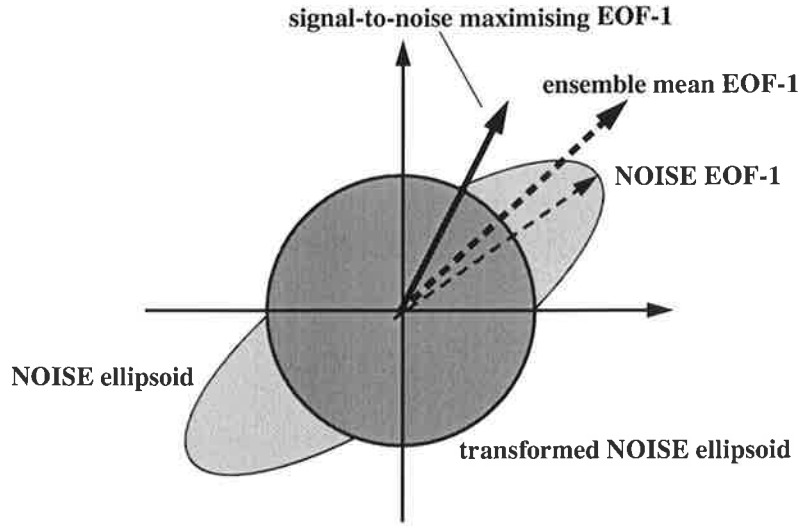


Figure 2.1: Schematic diagram of variance distribution of internal atmospheric variability in a two-dimensional EOF-space before (light shading) and after (dark shading) the “pre-whitening transformation” together with the leading EOFs of the ensemble mean and the estimated internal atmospheric variability (NOISE).

ranking the elements of  $\Lambda_N$  (i.e. the singular values) in decreasing order.

Second, the ensemble mean  $\mathbf{X}_M$  is projected onto the  $\kappa$  highest-ranked EOFs of the noise (that is, the first  $\kappa$  columns of the matrix  $\mathbf{E}_N$ , being the left singular vectors of  $\mathbf{X}_N$ ), weighting by the inverse of the corresponding noise singular values:

$$\mathbf{X}'_M = n^{\frac{1}{2}} (\Lambda_N^{(\kappa)})^{-1} \mathbf{E}_N^{(\kappa)T} \mathbf{X}_M := \mathbf{F}^T \mathbf{X}_M. \quad (2.3)$$

The effect of the *pre-whitening operator*  $\mathbf{F}$  is to give all patterns of internal variability contaminating  $\mathbf{X}_M$  the same expected variance in  $\mathbf{X}'_M$ . This is illustrated by the dark grey sphere in Fig. 2.1. The factor of  $n^{\frac{1}{2}}$  ensures that, in the absence of any true forced response,  $\mathbf{X}'_M$  will appear as unit-variance white noise. The truncation level  $\kappa$  is determined in a heuristic way (see Venzke et al., 1998a, for details).

Third, an EOF analysis is performed on the pre-whitened ensemble mean:

$$\mathbf{X}'_M = \mathbf{E}' \Lambda' \mathbf{P}'^T. \quad (2.4)$$

The convolution of  $\mathbf{E}'$  with the pre-whitening operator,  $\tilde{\mathbf{E}} = \mathbf{F} \mathbf{E}'$ , gives a set of optimal spatial filters. The highest ranked filter,  $\tilde{\mathbf{e}}_1$ , is the spatial pattern which maximises the ratio of ensemble-mean to within-ensemble variance (see equations (A.9) and (A.10) in the appendix). The time series obtained by projecting  $\mathbf{X}_M$  onto

$\tilde{\mathbf{e}}_1$  and normalising,

$$\mathbf{p}_1 = \frac{\mathbf{X}_M^T \tilde{\mathbf{e}}_1}{\lambda'_1}, \quad (2.5)$$

characterises the temporal evolution of the dominant mode of the forced response. Fourth, the spatial pattern of variability associated with the dominant forced response is obtained by regressing  $\mathbf{X}_M$  onto the “optimised PC”  $\mathbf{p}_1$  :

$$\hat{\mathbf{e}}_1 \simeq \frac{\mathbf{X}_M \mathbf{p}_1}{\lambda'_1}. \quad (2.6)$$

This is equivalent to a backtransformation as proved in equation A.23 of the appendix.

In the following section the superiority of the above algorithm over conventionally used analysis methods is demonstrated by applying it to the ensemble data over the North Atlantic. Thereafter, it is used to detect and characterise the forced response over the North Pacific.

## 2.3 The atmospheric response over the North Atlantic to decadal SST changes

### 2.3.1 Limitations of conventional methods

The simplest way of understanding how the optimal filtering procedure works, and why it is necessary, is in the context of EOF analysis which is the conventional method of analysing spatio-temporal datasets. The basic assumption of EOF analysis is that  $\mathbf{X}_M$  may be represented by a small number of spatial patterns, or EOFs, modulated by corresponding time series of pattern-amplitudes, or principle components (PCs). In this section the focus is on MSLP but other atmospheric variables were also considered (see Venzke et al., 1998a, for details).

Fig. 2.2a and Fig. 2.2b show the leading EOFs and associated normalised PCs of the ensemble mean MSLP over the North Atlantic for winter and spring. They account for 40% and 50% of the total variance in each season, respectively. The PCs suggest variations on a decadal timescale, while the EOF-patterns display the dipole structure of the atmospheric part of the decadal mode described by Deser and Blackmon (1993) and Grötzner et al. (1998). This kind of dipole is often associated with the North Atlantic Oscillation (NAO – Hurrell, 1995). The seasonal difference

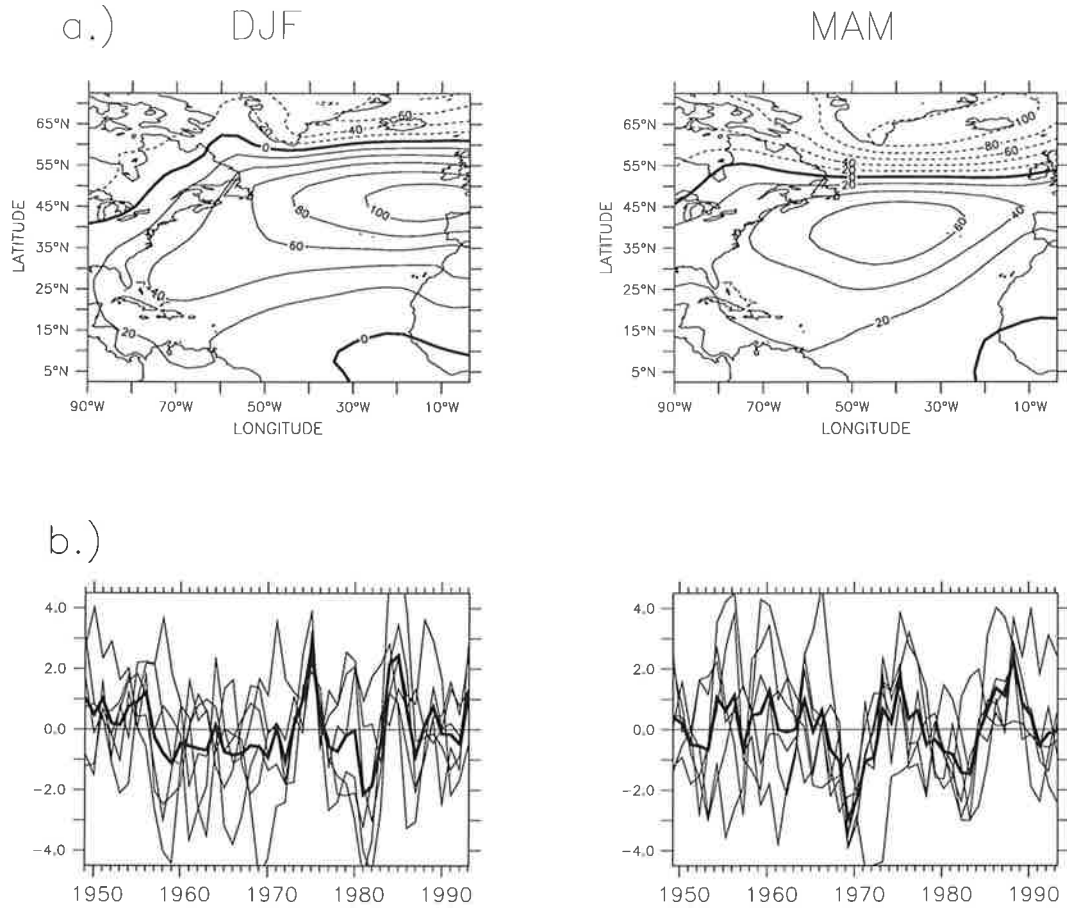


Figure 2.2: (a) First EOF of winter (DJF) and spring (MAM) MSLP [Pa] for the ensemble mean (explaining 40% and 50% of the total variance, respectively). (b) Projections of MSLP from ensemble members (thin lines) and ensemble mean (thick line) onto patterns shown in (a).

between the patterns is similar to that observed by Rogers (1990) and Davies et al. (1998).

These EOF/PC pairs, by construction, account for the maximum possible variance in the ensemble mean MSLP,  $\mathbf{X}_M$ . However, they also account for a substantial fraction of the internal atmospheric variability, whose characteristics may be estimated from the deviations from the ensemble mean,  $\mathbf{X}_{Nk}$ . As a result, projections of the individual ensemble members onto these EOFs, shown as thin lines in Fig. 2.2b, display a large spread, raising the question of whether the true forced response in this pattern might be zero, and the ensemble-mean variability that is described by the thick line in Fig. 2.2b is simply due to sampling noise in a finite ensemble.

This question can be addressed straightforwardly, using the Analysis of Variance (ANOVA) approach of Davies et al. (1998) and Rowell (1998). If the true forced response in this pattern is zero and the ensemble members are independent then the expected variance of the ensemble mean time series  $\sigma_M^2$  would be  $1/n$  times the expected variance of the internal variability  $\sigma_N^2$ . This can be couched in terms of a statistical test, as follows: if  $\mathbf{x}_k$  is the time series of amplitude coefficients of a normalised pattern  $\mathbf{e}$  (the first EOF of the ensemble mean in this case) in the  $k^{\text{th}}$  ensemble member, so  $\mathbf{x}_k = \mathbf{X}_k^T \mathbf{e}$ , then

$$n \frac{\hat{\sigma}_M^2}{\hat{\sigma}_N^2} \equiv n \frac{\frac{1}{m-1} \mathbf{x}_M^T \mathbf{x}_M}{\frac{1}{m(n-1)} \sum_k \mathbf{x}_{Nk}^T \mathbf{x}_{Nk}} \sim F_{m'-1, m'(n-1)} \quad (2.7)$$

where  $F_{m'-1, m'(n-1)}$  is the standard  $F$ -distribution with  $m' = m/3$  to take into account the 3-year running mean smoothing, and  $\hat{\sigma}_M^2$  and  $\hat{\sigma}_N^2$  are unbiased estimates of  $\sigma_M^2$  and  $\sigma_N^2$ , respectively.

The top two lines of Tab. 2.1 show  $\hat{\sigma}_M^2$ ,  $\hat{\sigma}_N^2$ , their ratio and  $n$  times their ratio for the projection of the ensemble members onto the first EOF of the ensemble mean as shown in Fig. 2.2b. Since  $n\hat{\sigma}_M^2/\hat{\sigma}_N^2$  exceeds the 95% critical value of the  $F$ -distribution,  $F_{0.05}$ , one can conclude at this confidence level that there is a non-zero forced response in this pattern (or “state space direction”). The spread of the thin lines in Fig. 2.2b, however, indicates that even though this response is non-zero, it is far from robust.

Results from ANOVA are critically dependent on the size of the ensemble. It will always be possible to detect a non-zero but arbitrarily weak forced response given a sufficiently large ensemble. Since the real world represents an ensemble of size one, it has to be distinguished between a response which is strong enough to be detectable only in an ensemble mean, and a response which is strong enough that one would expect (with more than 95% chance) its temporal evolution in an individual ensemble member to be positively correlated with the time series of the true response (this condition will be referred to in the following as “the temporal evolution being of the correct sign”). It will therefore be distinguished between a *detectable* response, in which  $n\hat{\sigma}_M^2/\hat{\sigma}_N^2 > F_{0.05}$ , and a *consistent* response, in which  $\hat{\sigma}_M^2/\hat{\sigma}_N^2 > F_{0.05}$ .

The requirement of consistency is not satisfied by the dipole obtained by standard EOF analysis. Thus one should not expect (at the 95% level) to get even the sign of the temporal evolution of this pattern correct in an individual ensemble member. From conventional EOF analysis one would hence conclude that the forced response in the direction of the first EOF is non-zero but is not consistent enough to be

Diagnostic: Projection on ...	$\hat{\sigma}_M^2$	$\hat{\sigma}_N^2$	ratio	$n \times \text{ratio}$
ens. mean EOF-1 (DJF, detrended)	9.15e+5	2.58e+6	0.354	<b>2.128</b>
ens. mean EOF-1 (MAM, detrended)	8.58e+5	2.45e+6	0.350	<b>2.101</b>
S/N max. EOF-1 (DJF, detrended)	17.558	6.000	<b>2.926</b>	<b>17.558</b>
S/N max. EOF-1 (MAM, detrended)	24.184	6.000	<b>4.031</b>	<b>24.184</b>
ens. mean EOF-1 (DJF, no ENSO)	7.48e+5	2.80e+6	0.264	1.586
ens. mean EOF-1 (MAM, no ENSO)	8.25e+5	2.39e+6	0.345	<b>2.071</b>
S/N max. EOF-1 (DJF, no ENSO)	6.658	6.000	1.109	<b>6.658</b>
S/N max. EOF-1 (MAM, no ENSO)	14.918	6.000	<b>2.486</b>	<b>14.918</b>

Table 2.1: *Estimated ensemble-mean and within-ensemble variances,  $\hat{\sigma}_M^2$  and  $\hat{\sigma}_N^2$  in selected diagnostics discussed in the text. The 5% cut-off value of the  $F_{m'-1, m'(n-1)}$  distribution,  $F_{0.05} = 1.83$ . Ratios, shown bold, in column 5 which exceed this cutoff value indicate a response in the corresponding diagnostic which is detectable at the 95% level. Bold ratios in column 4 indicate a response which is both detectable and consistent at this level.*

reproduced in an additional ensemble member. The optimal detection algorithm, however, successfully reveals a consistent forced response as will be shown next.

### 2.3.2 Application of the optimal detection algorithm

As introduced above, the optimal detection algorithm provides three diagnostics to describe the basic spatio-temporal characteristics of the forced response:

- (i) the spatial pattern which represents an optimal filter to discriminate between the forced response and internal variability
- (ii) the time series characterising the temporal evolution of the dominant mode of the forced response (“optimised principle component”)
- (iii) the pattern showing the variance characteristics of the dominant mode of the forced response

These three diagnostics are shown for the case of MSLP over the North Atlantic in Fig. 2.3.

The optimal filter patterns (Fig. 2.3a) reveal large-scale coherent regions over the tropical and subtropical Atlantic Ocean whereas in midlatitudes the patterns are

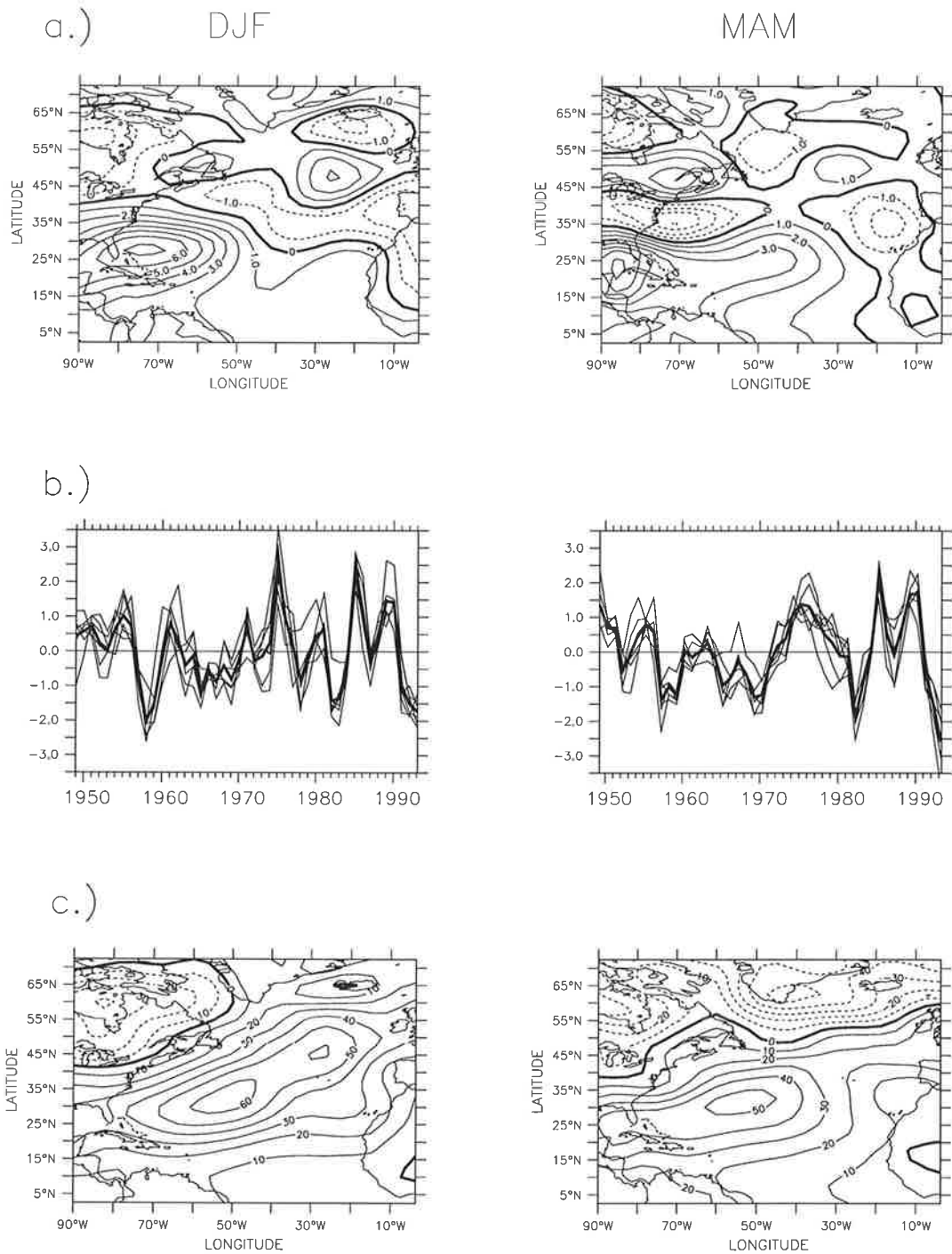


Figure 2.3: (a) Normalised optimal filter patterns,  $\tilde{\mathbf{e}}_1$ , for winter (DJF) and spring (MAM) MSLP. (b) Projections of ensemble mean (heavy line) and individual ensemble members (thin lines) MSLP onto the patterns shown in (a). (c) Signal-to-noise maximising dominant eigenvector,  $\hat{\mathbf{e}}_1$  estimating the true forced MSLP response [Pa].

broken up into small-scale structures of lower amplitude. Thus the time series of the amplitude of these patterns in any dataset will be dominated by what happens at low latitudes. This is consistent with the picture provided by a local ANOVA – see Rowell (1998). The advantage of the method presented here over a local ANOVA is that it allows to delineate the spatio-temporal characteristics of the dominant forced response, in addition to identifying the regions where such a response may exist.

The normalised pattern-amplitude time series of  $\tilde{\mathbf{e}}_1$  in the ensemble mean  $\mathbf{X}_M$ , that is  $\mathbf{p}_1 = \lambda_1^{-1} \mathbf{X}_M^T \tilde{\mathbf{e}}_1$ , is shown as the thick line in Fig. 2.3b. The thin lines in Fig. 2.3b show the projections of the individual ensemble members onto  $\tilde{\mathbf{e}}_1$ , that is:  $\mathbf{p}_k = \lambda_1^{-1} \mathbf{X}_k^T \tilde{\mathbf{e}}_1$ . The algorithm has clearly been extremely successful in reducing the spread between ensemble members: in the direction defined by  $\tilde{\mathbf{e}}_1$ , the response is both detectable and consistent, in the sense defined above (Tab. 2.1, line 3 and 4).

The vector  $\tilde{\mathbf{e}}_1$  (Fig. 2.3a) represents an optimal filter for extracting the time evolution of the forced response, but it is not itself an estimate of the leading mode of the forced response. This is given by the vector  $\hat{\mathbf{e}}_1$  (Fig. 2.3c) which provides an estimate of the first EOF of  $\mathbf{X}_F$ , the mean evolution of a hypothetical infinite ensemble.

The principal origin of the dominant signal is the remote response to El Niño. The characteristic time series (Fig. 2.3b) contain strong interannual fluctuations and the optimal filter patterns (Fig. 2.3a) which extract these from the ensemble mean MSLP are most pronounced over Central America where the atmosphere is strongly influenced by the Southern Oscillation. If one maps the regression coefficients of SST anomalies on the characteristic time series (Fig. 2.4a, contour lines) and the fraction of total SST variance explained by the regression (shaded), the tropical Pacific origin of the detected signal becomes clear.

As in this section the focus of interest is on the atmospheric response to decadal changes in Atlantic Ocean SSTs, the component of atmospheric variability that is due to the remote impact of tropical Pacific SST anomalies (especially those that are associated with the ENSO) is reduced by computing the regression of the seasonal mean MSLP, wind stress and heat flux anomalies from every ensemble member with the Niño-3 SST index (5°N-5°S, 150°W-90°W) time series and retaining only the residual part of the data for the detection analysis.

Repeating the signal-to-noise maximising analysis with the *ENSO-removed* MSLP data, the characteristic time series (Fig. 2.5b) change considerably. They contain much less interannual and more pronounced decadal fluctuations than before. As can be inferred from Fig. 2.4b, the detected atmospheric response can now mainly

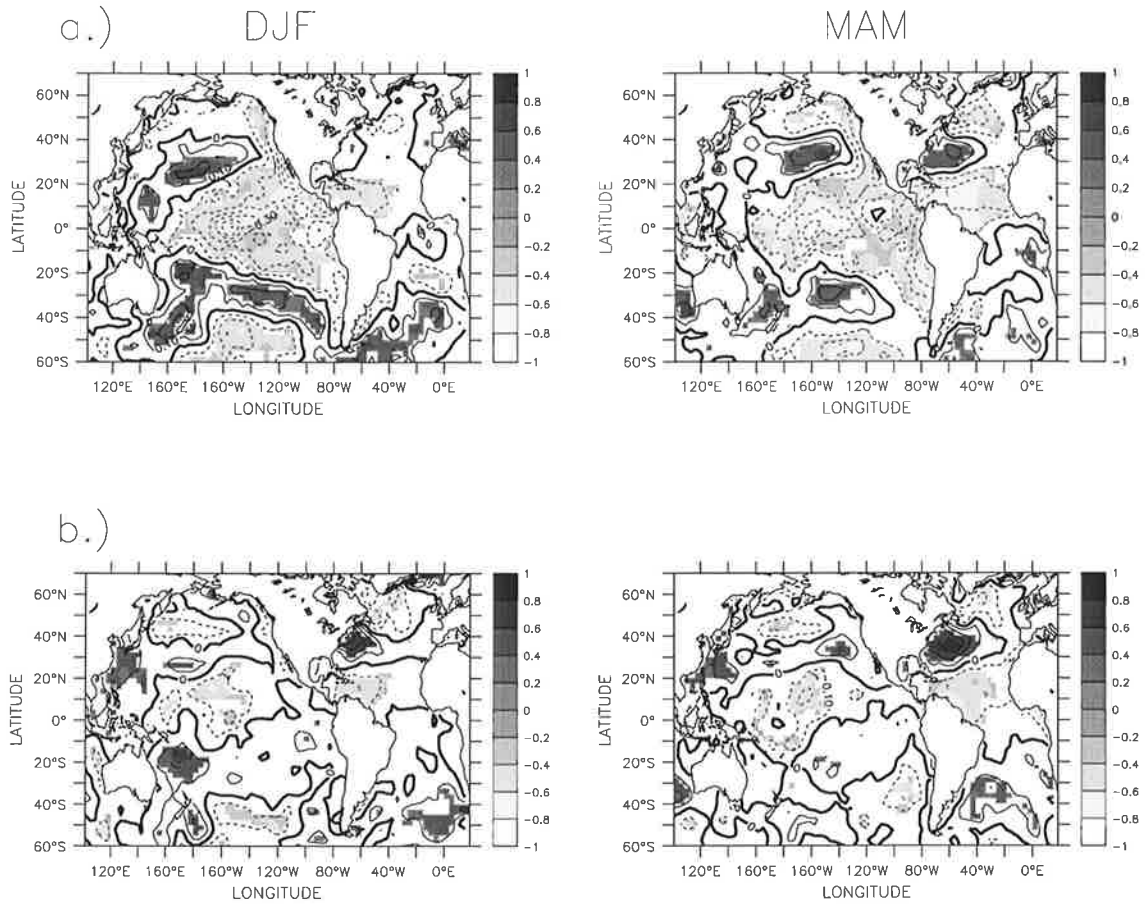


Figure 2.4: (a) Regression coefficients [K] (contour lines) and fraction of total variance explained (shaded contours, - plotted only where significant at the 95% confidence level and with sign appropriate to the sign of the correlation) by the regression of sea surface temperature anomalies onto time series shown in Fig. 2.3b (heavy line). (b) Same as (a) but for the regression onto time series shown in Fig. 2.5b.

be attributed to Atlantic Ocean SST anomalies which exhibit the tripole structure reported in various other studies of model data and observations (e.g. Deser and Blackmon, 1993; Grötzner et al., 1998; Sutton and Allen, 1997). The remote effect of ENSO-related SST anomalies in the tropical Pacific Ocean was successfully removed. In so doing a portion of the common signal was also removed from the data, causing a slight decrease in the signal-to-noise ratios. However, the variance of  $\mathbf{X}_M$  in the direction of  $\tilde{\mathbf{e}}_1$  is still almost one order of magnitude larger than the corresponding variances of the  $\mathbf{X}_{Nk}$ . The estimate of the dominant MSLP response,  $\hat{\mathbf{e}}_1$ , (Fig. 2.5c) again has a dipole-structure similar to that shown in Fig. 2.2a. One now knows,

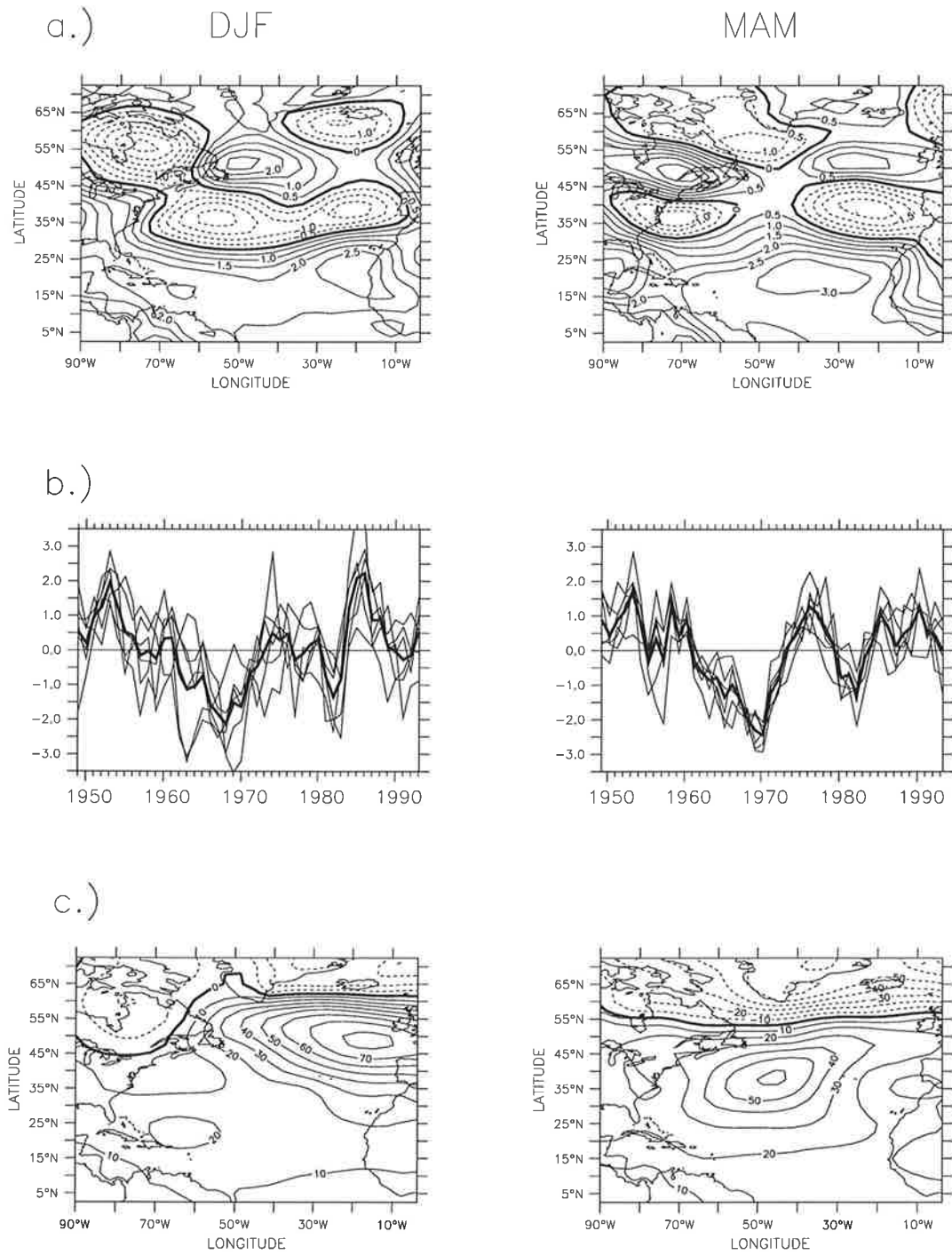


Figure 2.5: Same as Fig. 2.3 but for ENSO-removed MSLP data.

however, that different parts of this pattern are associated with very different levels of predictability. The most predictable variability is found over the tropical and subtropical Atlantic, as shown by the optimal filter pattern,  $\tilde{e}_1$ . The temporal evolution of  $\tilde{e}_1$  is, in both winter and spring, detectable at the 95% level. In spring, in contrast to the estimated forced response from standard EOF analysis, the evolution of this pattern is even consistent between the individual ensemble members, in the sense defined above (Tab. 2.1, lines 7 and 8).

The main result to stress here is that a detectable, and in spring even consistent, response to SST and sea-ice anomalies in the modelled North Atlantic MSLP data was detected. Regression analysis suggests this signal arises as a response to fluctuations in a tripole pattern of North Atlantic SST. At this point it should also be mentioned that the same temporal evolution can be detected in other atmospheric variables such as wind stress and surface heat flux (see Venzke et al. (1998a) for details). The spatial characteristics of the detected response and its implications for coupled mechanisms of decadal climate variability will be discussed in detail below (section 2.3.4). Before that, it shall be demonstrated that the identified model response relates well to observations.

### 2.3.3 Comparison with observations

Does the MSLP response detected above in the model bear any resemblance to fluctuations in MSLP seen in the real world? MSLP observations for the period considered have been compiled in the COADS data set (da Silva et al., 1994).

Fig. 2.6a shows the time series obtained when one projects these observations onto the first EOFs of the ensemble mean from standard EOF analysis, and the time series obtained when one projects the ensemble mean and the ensemble members onto the same EOFs. There is little agreement between the time series derived from the observations and that derived from the ensemble mean. Projections onto the optimal filter patterns, however, yield time series that are well correlated, both in the case of full MSLP fields (Fig. 2.6b) and in the ENSO-removed case (Fig. 2.6c). These results show that not only is there a detectable and consistent response of the atmosphere model to oceanic forcing, but that this response is well matched in the observations.

The comparisons shown in Fig. 2.6 are influenced by both the temporal and the spatial characteristics of our model's response. As a consequence of small systematic errors in the model mean state it is possible that the model responds to the same SST

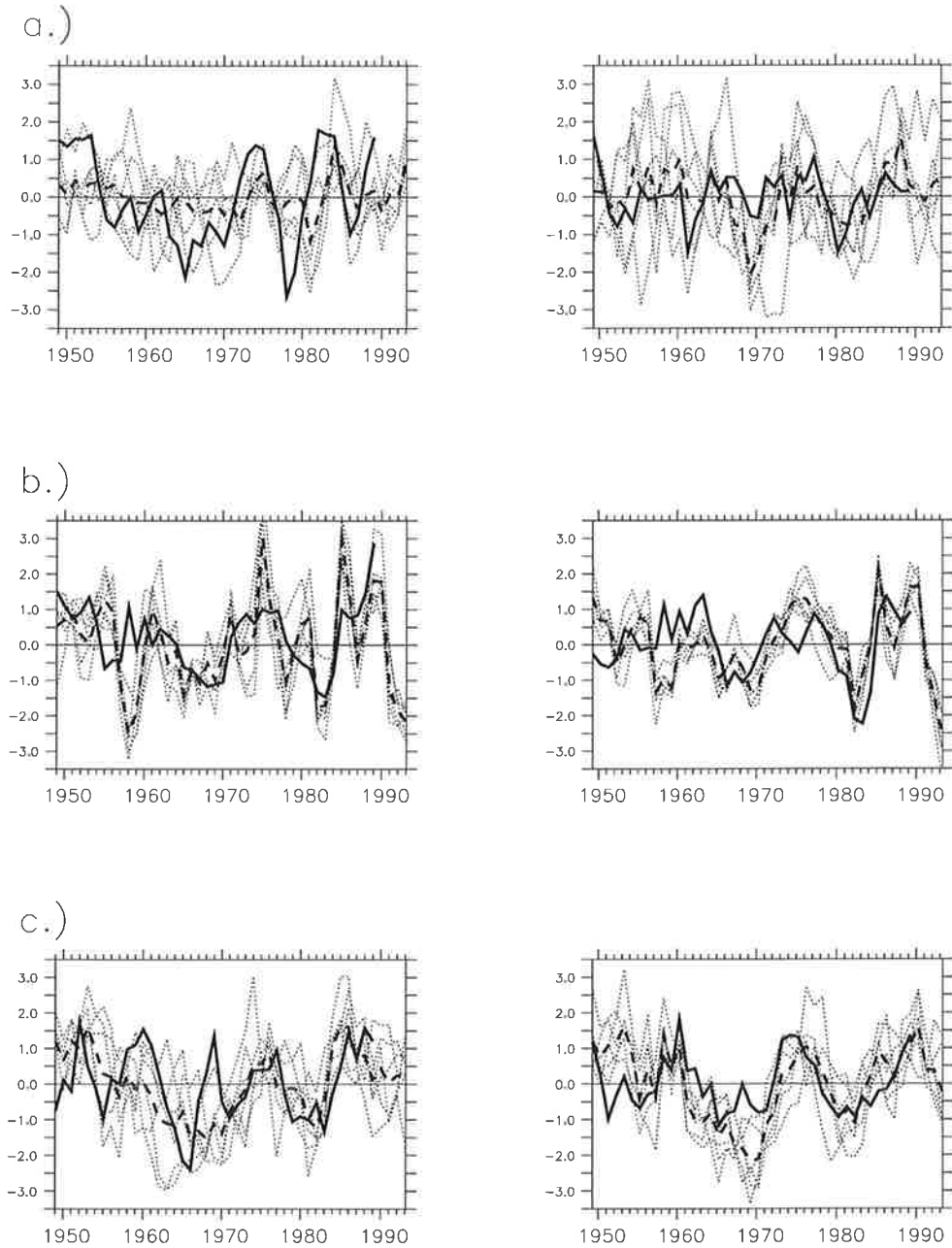


Figure 2.6: Projections of winter (left panels) and spring (right panels) mean sea level pressure from individual ensemble members (thin dotted lines), the ensemble mean (dashed line) and observations (COADS - solid line) onto (a) patterns show in Fig. 2.2a, (b) patterns shown in Fig. 2.3a and (c) after “ENSO removing” onto patterns shown in Fig. 2.5a. As the COADS data set contains only data over sea, all projections were computed over sea-points only.

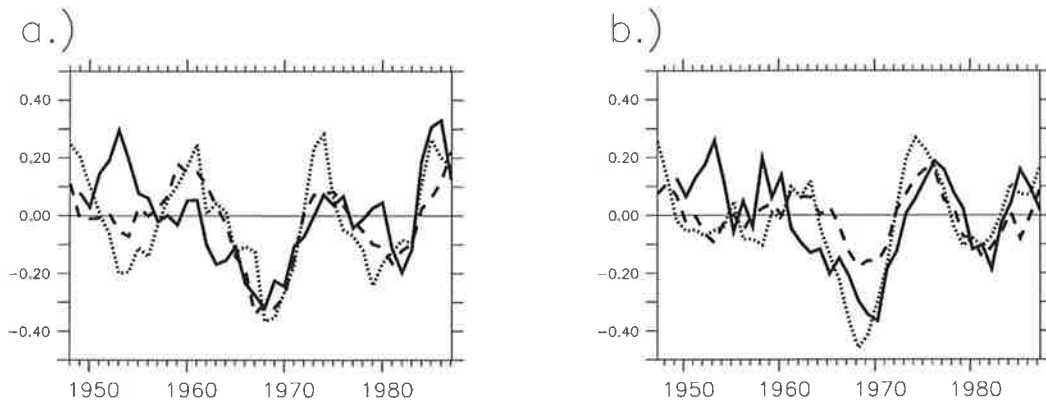


Figure 2.7: Characteristic time series of dominant MSLP response (solid line) in (a) winter and (b) spring together with index time series (averaged over 15-25N; 40-60W) of low-pass filtered observed MSLP anomalies (dashed line) and index time series (averaged over 25-35N; 70-80W) of observed SST anomalies (dotted line). The magnitude of the curves has been scaled.

fluctuation as the real atmosphere (so that the temporal evolution of the response is correct), but produces a spatial pattern of MSLP which is somewhat in error. Such errors may be a cause of some of the discrepancies between the projections of the observed data and the model data onto the optimal filter patterns. Fig. 2.7 shows a comparison between the model and observations that is not influenced by such errors. Here the time series associated with the most predictable mode of HadAM1 MSLP variability ( $p_1$  obtained from the optimal filter) are compared with the index time series of observed SST and MSLP variations that were found by Sutton and Allen (1997) to be characteristic of the propagation of temperature anomalies across the North Atlantic. It shall be noted again that no observational data (other than, indirectly, the SSTs used to force the model) have been used to derive the HadAM1 MSLP optimised time series (in contrast, for example, to a Canonical Correlation Analysis).

The agreement shows that the common pattern obtained through the signal-to-noise maximising analysis of model MSLP exhibits a temporal evolution that is characteristic of the underlying ocean variations. It suggests that the observed correlations between SST and MSLP fluctuations must reflect, at least in part, an influence of the ocean on the atmosphere. The nature of this influence will be discussed next.

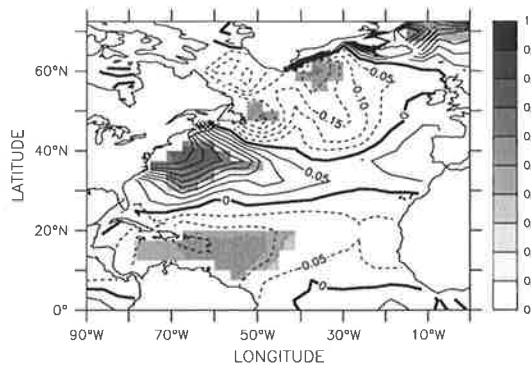
### 2.3.4 Spatial characteristics of the response

Above, it has been established that the ensemble of atmospheric model integrations exhibits common decadal fluctuations in the subtropical North Atlantic region. The temporal evolution of the common signal resembles the time series that have been related to the slow propagation of observed temperature anomalies across the North Atlantic. The implication is that dynamical processes in the North Atlantic Ocean may be influencing decadal fluctuations in the atmosphere above. One needs to ask next how the atmospheric fluctuations might feed back to the ocean, and to consider in particular whether the above results support the possibility of a coupled ocean-atmosphere mode of decadal variability. To address these questions the spatial characteristics of the response are examined in several different variables.

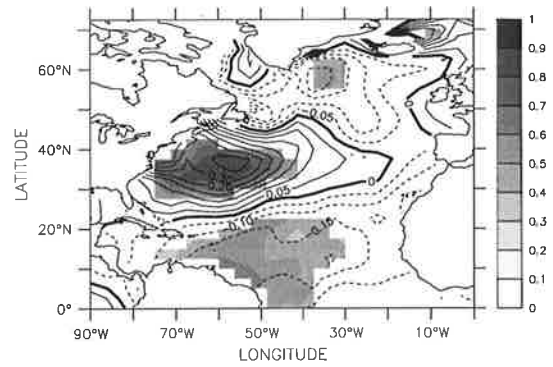
Fig. 2.8 shows maps of the regression coefficients (contour lines) from a regression onto the characteristic temporal evolution of the forced response (Fig. 2.5b) for anomalous SSTs and ensemble means of: MSLP; wind stress; net surface heat flux; and wind stress curl. The shading indicates the fraction of total ensemble mean variance explained by the regression. Corresponding regression maps were also computed for the individual ensemble members. Shaded areas indicate regions where regression coefficients of the ensemble mean were found to be significantly different from zero (i.e. 'detectable') at the 95% confidence level based on a Student's *t*-test. In line with the findings of Grötzner et al. (1998), MSLP fluctuations associated with the detected response are dominated by a large-scale dipole structure (Fig. 2.5c and Fig. 2.8b). In DJF the dipole is located in the north eastern part of the Atlantic basin, while in MAM it is shifted southwestward. The fraction of total MSLP variance explained by the regression is largest over the tropical and subtropical North Atlantic, in line with the observational analysis of Sutton and Allen (1997). The higher level of internal variability at high latitudes means that the atmospheric response is less strong here and in many regions not detectably different from zero. A gridpoint based analysis of variance, ANOVA, yields the same regions of significantly non-zero MSLP response (not shown). However, an estimate of the spatial characteristics and temporal evolution of the response could not have been inferred from the gridpoint based ANOVA statistic.

The wind stress response (Fig. 2.8c) shows the main features one would anticipate from the MSLP response assuming geostrophic balance. In spring, when the response is most consistent, there is a tendency for intensified westerlies (around 55°N) and, more consistently, for intensified trades (around 15°N) in association with

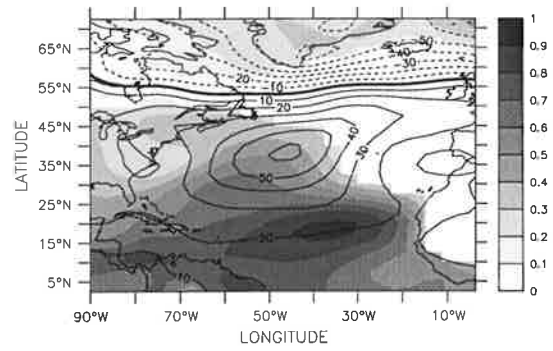
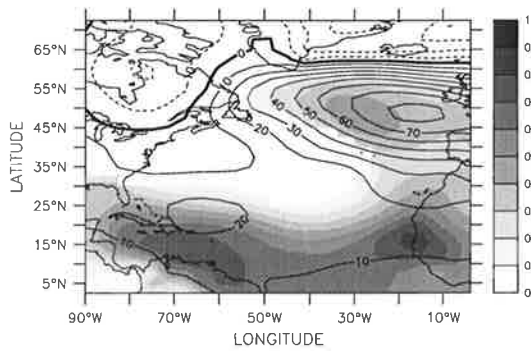
a.) SST DJF



MAM



b.) SLP



c.) TAU

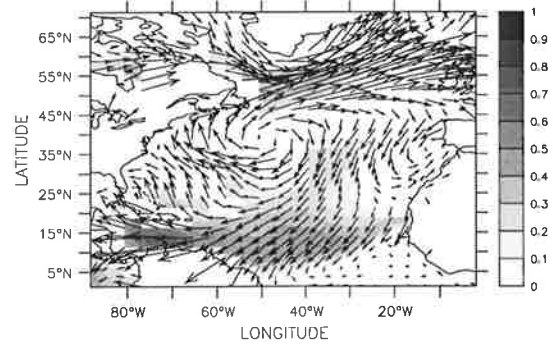
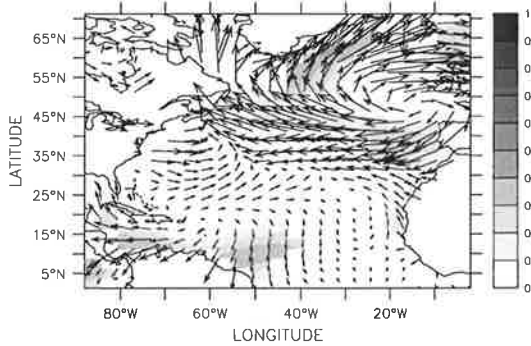
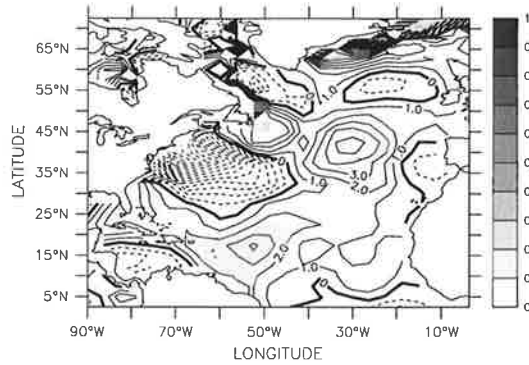
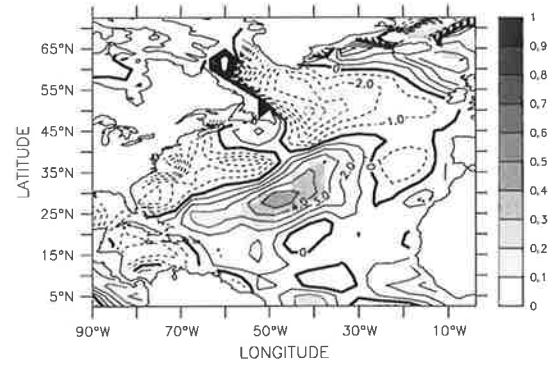


Figure 2.8: Regression coefficients (contour lines) and fraction of total variance explained (shaded contours, - plotted only where significant on the 95% confidence level) by regression of observed sea surface temperature anomalies [K] onto time series shown in Fig. 2.5b (heavy line). Regression coefficients (contour lines) and fraction of total ensemble mean variance explained (shaded contours, - plotted only where detectable on the 95% confidence level) of ENSO-removed (b) mean sea level pressure [Pa], (c) wind stress [Pa], (d) net surface heat flux [ $W/m^2$ ] and (e) wind stress curl [ $10^{-8} Pa/m$ ] onto time series shown in Fig. 2.5b (heavy line).

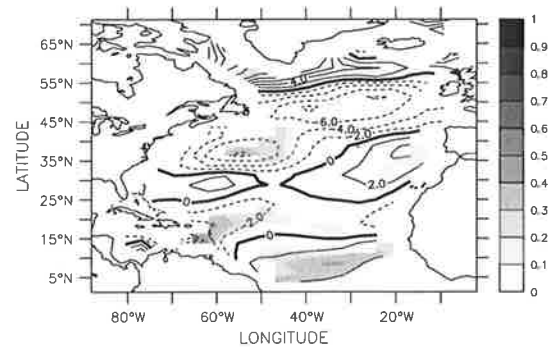
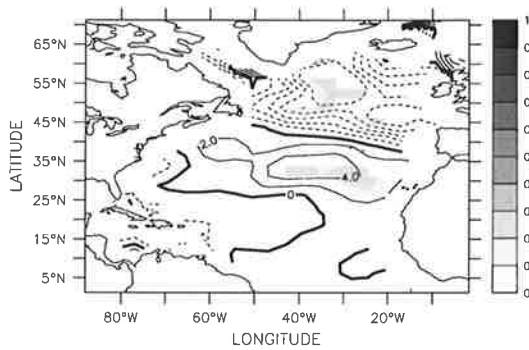
d.) net Q DJF



MAM



e.) curl



anomalously warm SSTs off the U.S. coast and anomalously cold SSTs in the tropical/subtropical Atlantic, and in the North Atlantic south of Greenland (Fig. 2.8a). Through their effects on surface heat fluxes and Ekman fluxes one would expect these wind anomalies to affect local SSTs. The heat fluxes associated with the common response are shown in Fig. 2.8d. In considering these, however, one needs to keep in mind that in these experiments the SST was prescribed. This artificial constraint could possibly lead to an overestimation of heat flux anomalies (see Barsugli and Battisti, 1998; Saravanan and McWilliams, 1998). It is also important to note that one cannot establish from these experiments whether the atmospheric response is induced by the whole SST tripole pattern or only by some part of it. If it is the latter, then correlated SST fluctuations in one part of the tripole could, in the real world, be forced by the atmospheric response to SST fluctuations in the other parts. The enhanced westerlies around 55°N in spring will act to cool the local ocean surface through enhanced extraction of heat by turbulent fluxes associated with enhanced advection of cold air from the Labrador Sea and Canada and enhanced

wind speeds, and through advection of the mean temperature field by anomalous Ekman currents. Even though the SSTs in this region are (i.e. are prescribed to be) anomalously cold, Fig. 2.8d shows that there is nonetheless an anomalous heat flux out of the ocean in MAM. A break-down of the surface heat flux into its individual components (not shown) shows that the major contributions are from sensible and latent heat fluxes, as anticipated above.

If this northern component of the SST tripole is playing an active role in the forcing, then the atmospheric response in this region seems to indicate a weak positive feedback, as noted by Grötzner et al.(1998). Based on the *t*-test, the ensemble mean response in the shaded area is readily detectable (significantly different from zero at the 95% confidence level). The much more stringent test of consistency indicates that, if the atmosphere model was forced again with the same SSTs, one would obtain zonal wind stress (net surface heat flux) anomalies in this region positively (negatively) correlated with the characteristic temporal evolution shown in Fig. 2.5b in approximately 90% of cases.

If, on the other hand, the atmospheric response is forced entirely by the more southerly components of the SST tripole, then these results should not be interpreted as evidence of an atmospheric feedback. Rather, they would suggest that forced fluctuations in high latitude North Atlantic SST could arise as a remote response to lower latitude SST changes.

In phase with the enhanced westerlies around 55°N, enhanced trade winds are found over the tropical/subtropical ocean, again especially in spring (Fig. 2.8c). Here, even the sign of the zonal and meridional wind stress regression coefficients is found to be consistent at the 95% confidence level. One would expect that stronger trades bring cooler air from higher latitudes and enhance the turbulent heat fluxes, leading to anomalous cooling of the upper tropical/subtropical ocean. In Fig. 2.8d there is little evidence in MAM of surface heat loss in this region. This is presumably because the anomalously cold SSTs offset the effect on the heat fluxes of the enhanced trades. In the trade belt, therefore, the heat flux fields suggest that the atmospheric response does not generate a positive feedback on SST anomalies. Neither, however, is there clear indication in MAM of a negative feedback. Without the changes in atmospheric circulation (i.e. the changes in the strength of the trades) damping of the prescribed anomalous SSTs would be expected (as is found in DJF). Therefore one can reasonably argue that the atmospheric circulation response has served to decrease, or even eliminate, the damping of tropical Atlantic SST anomalies by anomalous surface heat fluxes. This effect should in turn increase the persistence

of SST anomalies in this region compared to their persistence in a scenario where there is no atmospheric circulation response.

Over the final lobe of the SST tripole, the western Atlantic around 30-40°N, the wind fluctuations in the atmospheric response are not reliably detectable either in DJF or MAM. In line with the results of Grötzner et al. (1998), the heat flux fields suggest a weak negative feedback. In winter, advection of cold air from the North American continent over anomalously warm water leads to enhanced latent and sensible heat loss.

An interesting feature in spring is found at around 50°W, 30°N. Here, surface heat flux anomalies arise that are both detectable and consistent. These anomalies are mainly due to reduced latent heat loss and enhanced solar radiation. The location and sign suggests that these heat flux anomalies might help to propagate SST anomalies from the Gulf Stream region eastwards.

The local feedbacks of the atmospheric response onto the SST tripole can be summarised as follows: a weak positive feedback south of Greenland and a weak negative feedback in the western Atlantic off the U.S. coast were detected. In the tropical Atlantic a negative feedback was found in DJF, but in MAM the anomalous heat fluxes are close to zero. The latter suggests that the atmospheric response acts to enhance the persistence of SST anomalies in this region. In all three regions the consistency of these local feedbacks is marginal.

As well as providing local instantaneous feedbacks, it has also been proposed (Latif and Barnett, 1994; Grötzner et al., 1998) that the atmospheric response could give a delayed nonlocal feedback to the ocean. Grötzner et al. (1998) describe two possible mechanisms for the delayed feedback to Gulf Stream SSTs. In the first, temperature anomalies in the tropical ocean are advected westward along the southern branch of the subtropical gyre and feed into the western boundary current. There they replace anomalies of the opposite sign, giving a phase reversal. As shown above the detected local feedbacks would support this mechanism. The second hypothesis requires the atmospheric response to include anomalies in wind stress curl. After a lag associated with the propagation of baroclinic Rossby waves, these anomalies force variations in the strength of the subtropical gyre circulation which modulate SST especially in the Gulf Stream region. The regression pattern of the ensemble mean wind stress curl (Fig. 2.8e) is characterised by small scale structures. To generate Rossby-waves that spin down the subtropical gyre circulation (giving a negative feedback), positive wind stress curl anomalies are required south of about 35°N. There is a little evidence for anomalies of the right sign in Fig. 2.8e but these are of

small spatial extent, in general are not detectable, and are nowhere consistent. The results from this experiment therefore do not support the hypothesis of a delayed negative feedback supplied by changes in wind stress curl in the North Atlantic.

The marginal consistency of all the feedbacks that were identified suggests that if they play a role in any coupled ocean-atmosphere mode of decadal North Atlantic climate variability, such a mode would not be robust against disruption by internal atmospheric variability and perturbations by other climate fluctuations external to the North Atlantic ocean-atmosphere system like those associated with ENSO. Further implications of this conclusion will be discussed in the course of this thesis.

## 2.4 The atmospheric response over the North Pacific to interannual and decadal SST changes

In the previous section an optimal detection algorithm was introduced that proved to be a powerful tool for the characterisation of SST-forced atmospheric variability. The most dominant SST-forced changes of the atmospheric circulation over the North Atlantic were caused by teleconnections from the tropical Pacific. Only after removing this ENSO-induced part of the variability was a decadal signal detected that is mainly related to decadal North Atlantic SST changes.

In the Pacific region the impact of tropical SST changes on the extra-tropical atmosphere seems to be even more dominant over the effect of extra-tropical SST changes. Lau and Nath (1994) argued that tropical SST anomalies associated with ENSO can induce large-scale atmospheric circulation anomalies over the extra-tropical Pacific and that North Pacific SST anomalies fail to do so. Alexander (1992a, b) showed that in turn atmospheric anomalies induced by tropical SST anomalies are capable of forcing large-scale SST anomalies in the extra-tropical Pacific. In a more quantitative manner, Cayan (1992a, b) demonstrated that the atmospheric circulation forces the extra-tropical ocean through the modulation of sensible and latent heat fluxes. These studies support the view that North Pacific SST anomalies are mainly a remote response to ENSO. The possibility of such a linkage has also been raised in connection with decadal variability. Trenberth and Hurrell (1994) as well as Graham (1994) argued that the North Pacific cooling which occurred from the 1970s to the 1980s can be interpreted as an extra-tropical response to a rise in eastern equatorial Pacific SSTs that took place at the same time. If one, alternatively, likes to interpret such long-term North Pacific SST changes in the concept of a decadal oscillation

based on extra-tropical air-sea interactions (Latif and Barnett, 1994, 1996), atmospheric variability must also exhibit some sensitivity to extra-tropical SST anomalies and therefore contain a consistent decadal signal that is independent from ENSO. Whether this is supported by the ensemble of HadAM1 integrations will be addressed in the following.

### 2.4.1 ENSO-related atmospheric variability

As stressed in many studies (e.g. Horel and Wallace, 1981; Ropelewski and Halpert, 1989), the atmospheric circulation over the North Pacific/American sector shows a very pronounced ENSO response which appears as the so-called Pacific North American pattern (PNA). Applying the optimal detection algorithm to North Pacific MSLP data ( $0^{\circ}\text{N}$ - $70^{\circ}\text{N}$ ,  $100^{\circ}\text{E}$ - $70^{\circ}\text{W}$ ) from the HadAM1 ensemble hence yields a consistent signal in winter ( $\hat{\sigma}_M^2/\hat{\sigma}_N^2 = 5.17$ ) and spring ( $\hat{\sigma}_M^2/\hat{\sigma}_N^2 = 5.19$ ) (Fig. 2.9a and 2.10a).

The detected signal can be clearly attributed to interannual SST anomalies in the central and eastern equatorial Pacific which are accompanied by SST anomalies of opposite sign in the central North Pacific (Fig. 2.9c and 2.10c). The MSLP response resembles the PNA pattern. Studies with simplified models (e.g. Hoskins and Karoly, 1981) provided a framework for understanding the PNA response: Warm SST anomalies in the eastern equatorial Pacific enhance local precipitation and give rise to upper level divergence; advection of vorticity by the divergent flow gives an effective Rossby wave generator in the western subtropical Pacific. Wave trains emanating from this region carry energy into the extra-tropics in a great circle path, which arches over the North Pacific and North America to give the PNA-like pattern in MSLP variability as seen in Fig. 2.9b and 2.10b.

Warm SST anomalies in the eastern and central equatorial Pacific are associated with westerly wind stress anomalies over the western and central equatorial Pacific, as well as increased westerlies in midlatitudes (Fig. 2.9d and 2.10d). It shall be noted that wind stress anomalies over the central North Pacific have in winter a stronger northerly component than in spring. Hence, enhanced meridional advection of cold air results in winter in a more effective cooling of central North Pacific SSTs than in spring. This is reflected very well by the associated net surface heat flux anomalies shown in Fig. 2.9e and 2.10e. Cayan (1992a, b) furthermore shows that the cooling is most effective in winter when the latent and the sensitive fluxes and their variability are greatest, while the radiative fluxes are weakest. A break-down of the simulated

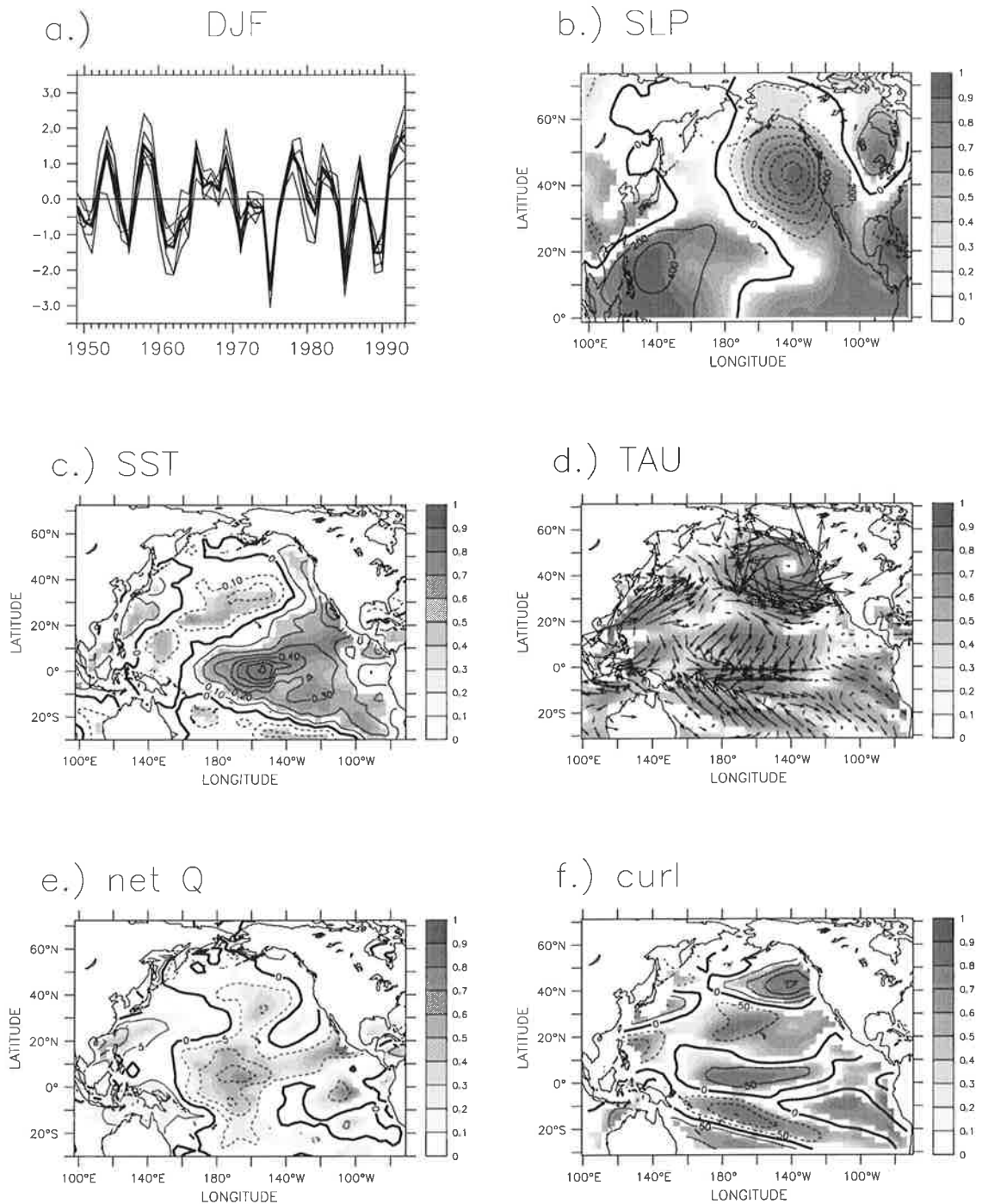


Figure 2.9: (a) Signal-to-noise maximising time series (heavy line) and projection of MSLP ensemble members onto signal-to-noise maximising pattern. Regression coefficients (contour lines) and fraction of total ensemble mean variance explained (shaded contours, - plotted only where detectable on the 95% confidence level) of (b) mean sea level pressure [Pa], (c) SST [K], (d) wind stress [Pa], (e) net surface heat flux [ $W/m^2$ ] and (f) wind stress curl [ $10^{-8} Pa/m$ ] onto time series shown (a) (heavy line).

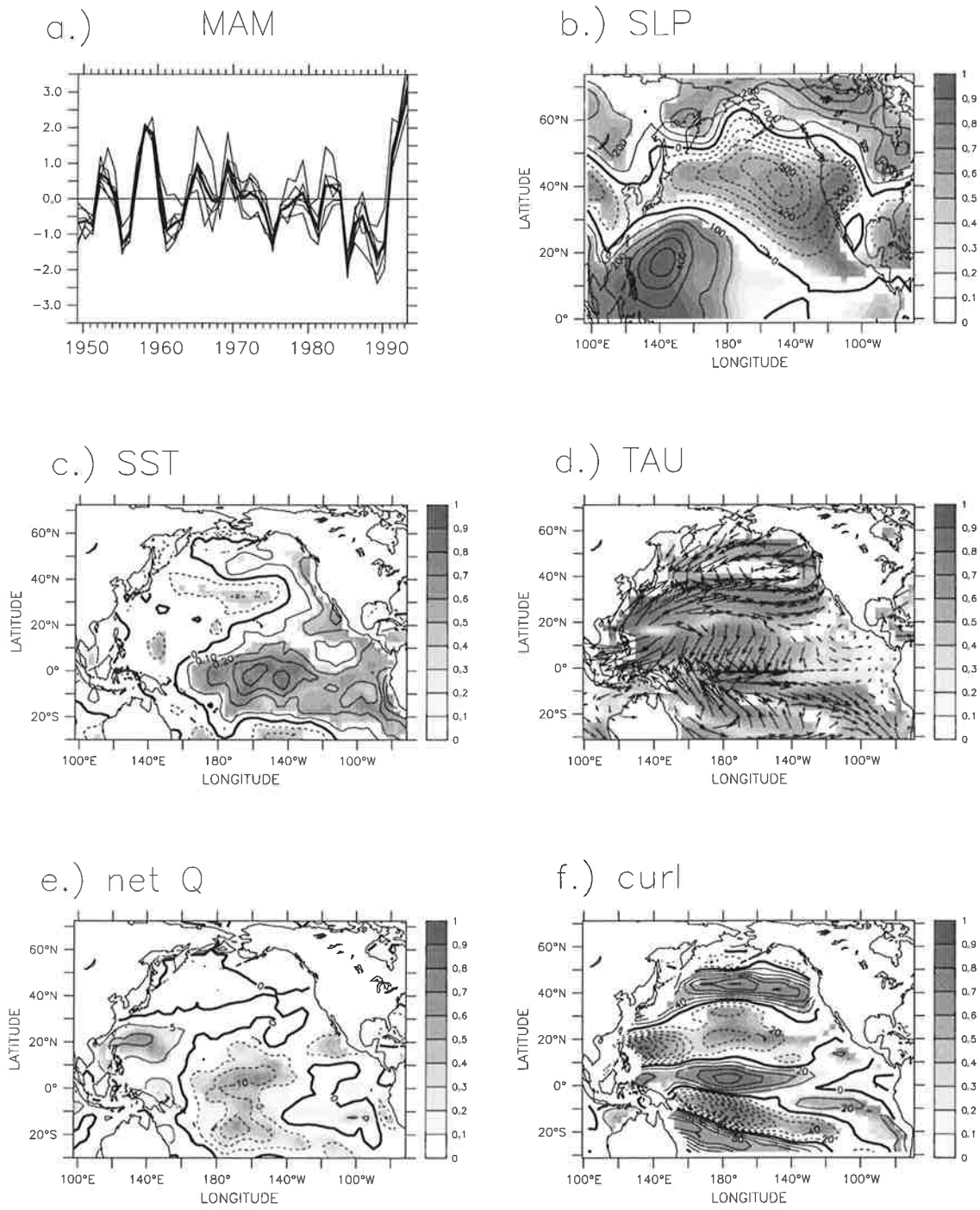


Figure 2.10: Same as Fig. 2.9 but for spring (MAM) data.

net surface heat flux into its individual components (not shown) supports this view. At this point, it shall be noted again that one has to be careful in estimating surface fluxes from atmospheric GCM integrations with prescribed SSTs as pointed out by Barsugli and Battisti (1998) as well as Saravanan and McWilliams (1998).

ENSO-related wind stress curl anomalies exhibit a pronounced meridional dipole structure over the North Pacific (Fig. 2.9f and 2.10f). They bear the potential to excite Rossby waves of opposite polarity in the midlatitudinal and subtropical North Pacific Ocean and could therefore be important for the generation of low-frequency changes in the the North Pacific Ocean. This issue will be addressed in more detail in chapter 3.

### 2.4.2 ENSO-independent atmospheric response

Above, a major fraction (34% in winter and 32% in spring) of the total North Pacific MSLP variability has been found to result in response to tropical SST changes related to ENSO. The next question to be answered is whether in addition to the ENSO-related component further consistent SST-forced atmospheric variability can be detected. In order to address this question, the ENSO-related variability has been reduced in all atmospheric data fields by computing the regression of the seasonal mean MSLP, wind stress and heat flux anomalies from every ensemble member with the Niño-3 SST index (5°N-5°S, 150°W-90°W) time series and retaining only the residual part of the data for the detection analysis in the same way as it was done over the North Atlantic in the previous section. Repeating the signal-to-noise maximising analysis with the ENSO-removed MSLP data, the characteristic time series change considerably (Fig. 2.11a and 2.12a). They contain much less interannual and more pronounced decadal fluctuations than before. The atmospheric GCM shows a consistent ( $\hat{\sigma}_M^2/\hat{\sigma}_N^2 = 3.14$  in winter and  $\hat{\sigma}_M^2/\hat{\sigma}_N^2 = 3.45$  in spring) response beyond the ENSO-related atmospheric circulation changes. The detected atmospheric signal does not show any linear in phase relation with SST changes in the eastern equatorial Pacific but is mainly connected with SST anomalies in the central subtropical and midlatitudinal North Pacific (Fig. 2.11c and 2.12c). It explains 11% (winter) and 20% (spring) of the total North Pacific MSLP variance. Analysing only observed SSTs by means of *Principle Oscillation Patterns* (POPs - Hasselmann, 1988; von Storch et al., 1995), Latif et al. (1997) were also able to separate a decadal mode from ENSO-related variability. POPs are, in general, complex with a real part and an imaginary part (Fig. 2.13). The evolution of the

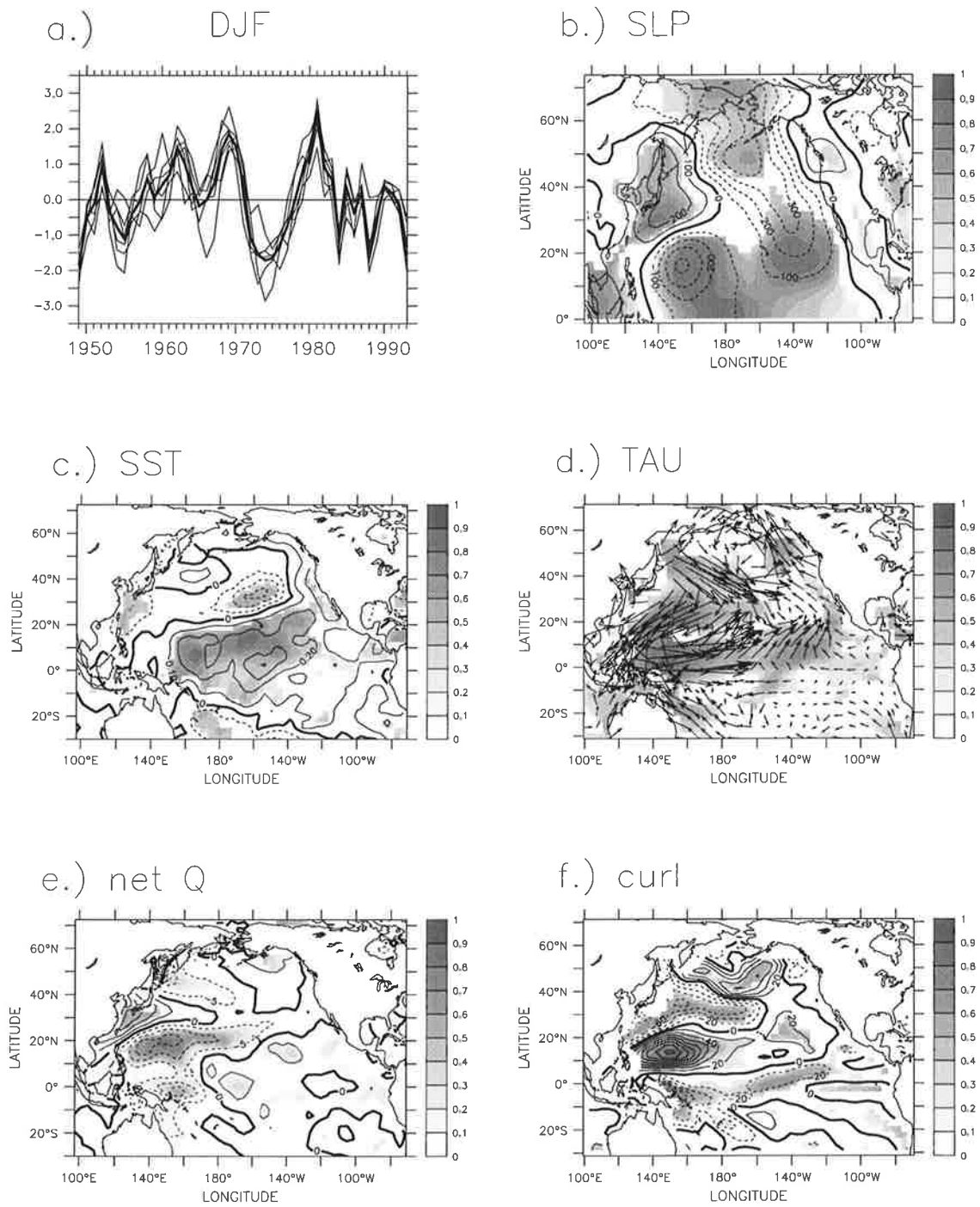


Figure 2.11: Same as Fig. 2.9 but for ENSO-removed data.

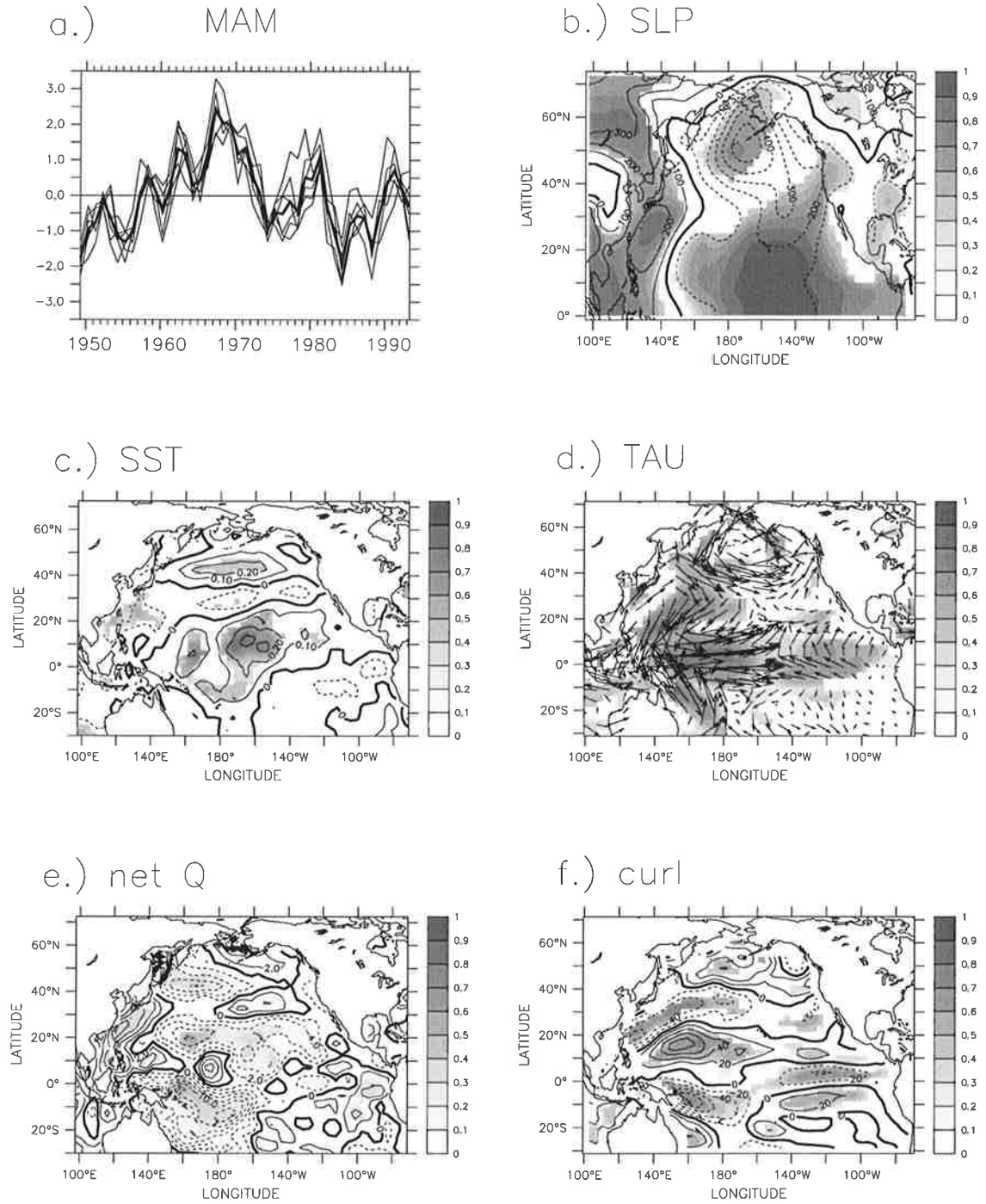


Figure 2.12: Same as Fig. 2.10 but for ENSO-removed data.

two-dimensional POP space can be interpreted as a cyclic sequence of spatial patterns. For the decadal POP mode, Latif et al. (1997) found the characteristic period to complete a full cycle to be 13 years. They point out, however, that timescale estimates from a relatively short record (they used the same GISST dataset that was used here) are subject to large uncertainties and focus their discussion on the spatial structures. The SST variance explained by the decadal POP shows relatively high values in the central subtropical and midlatitudinal Pacific as well as along the west coast of North America. In the interpretation of Latif et al. (1997) the relevant subtropical SST anomalies originate at the west coast of North America and propagate south westward, as indicated by the rotation from the negative real part of the POP to the imaginary part. Possible mechanisms for this remain unclear. The temporal evolution as well as the anomalous SST, MSLP and wind stress patterns that they obtained in association with the imaginary part of the decadal POP resemble very much those found here. It demonstrates that the optimal detection algorithm successfully revealed some sensitivity of the atmospheric GCM to one phase of the most dominant decadal mode of observed SST variability.

The spatial structure of the dominant ENSO-independent MSLP response shows marked differences from the PNA pattern (Fig. 2.11b and 2.12b). Low pressure extends from the Aleutian Islands equatorward over the entire central and eastern North Pacific. In parallel to the findings for the atmospheric response over the North Atlantic, the detected signal explains most MSLP variance over the tropical and subtropical region. Over the western Pacific MSLP anomalies of opposite sign are found. Especially in winter, this zonal pressure contrast leads to enhanced southward advection of cold air over the western part of the basin. Apart from the Yellow Sea and the East China Sea, where SSTs are already anomalously cold, this leads to heat loss of the western North Pacific ocean (Fig. 2.11e and 2.12e). In the central North Pacific, where the SST anomalies that are related to this mode of atmospheric variability are strongest, surface heat flux damping is reduced by anomalous meridional advection. Like in the previous section, the impact of anomalous advection may be interpreted as a positive feedback to the SST anomalies in that region. Apart from this positive feedback a coupled extra-tropical air-sea mode would require a delayed negative feedback from the atmosphere to the ocean. Latif and Barnett (1994, 1996) suggested that such a feedback might involve the adjustment of the strength of the subtropical ocean gyre by Rossby waves. These can be excited by wind stress curl anomalies as mentioned already in connection with ENSO-related atmospheric circulation changes (Fig. 2.9f and 2.10f). Wind stress

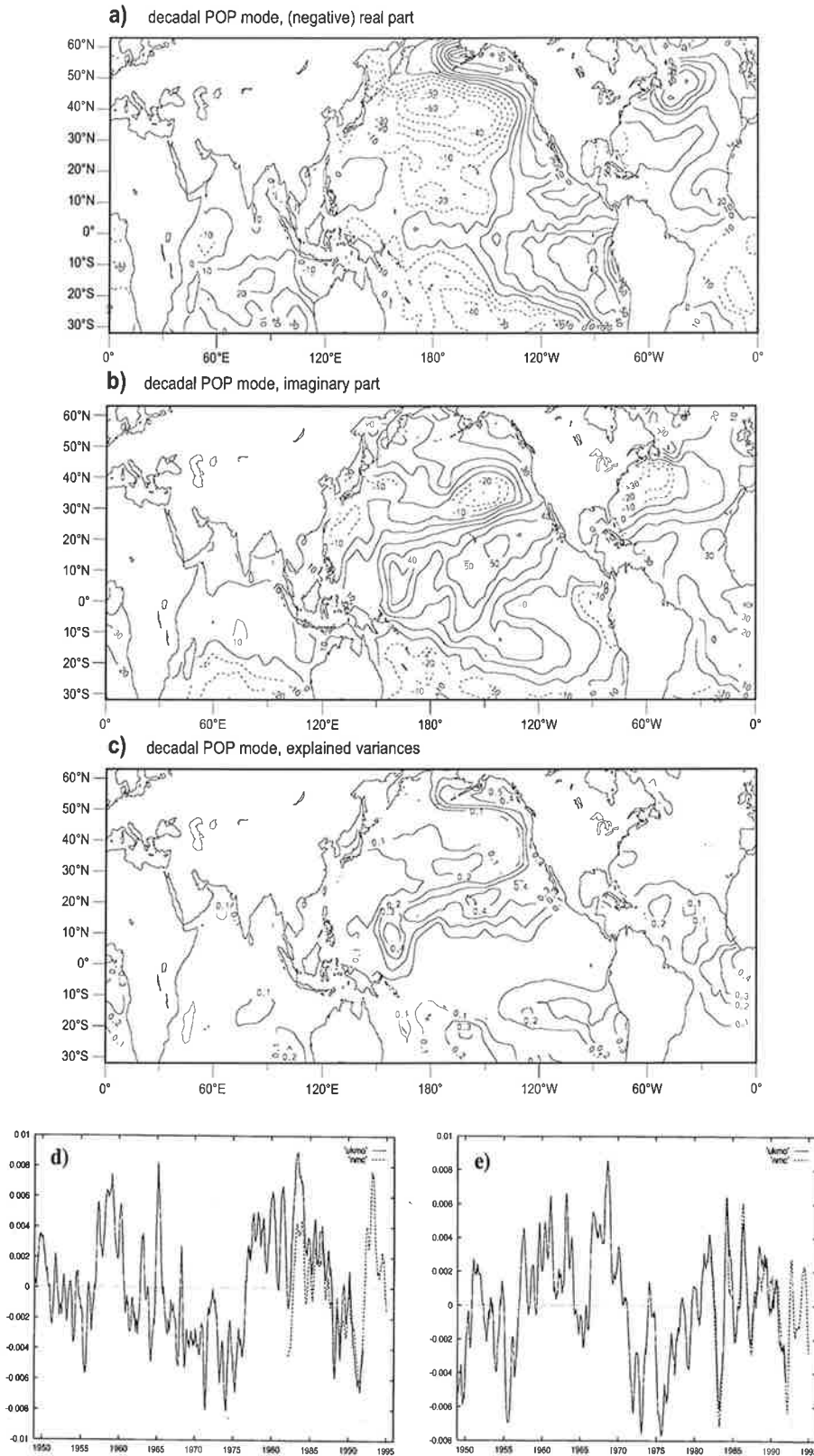


Figure 2.13: Decadal SST POP mode: (a) pattern of (negative) real part, (b) pattern of imaginary part, (c) variances explained, (d) projections of UKMO and NMC SSTs onto (a), and (e) projections of UKMO and NMC SSTs onto (b) (from Latif et al., 1997).

curl anomalies that are associated with extra-tropical SST anomalies also exhibit a meridional dipole structure (Fig. 2.11f and 2.12f) in midlatitudes and the subtropics. It is, however, less pronounced than that associated with ENSO and the centers of the anomalies are located further to the west. Additionally, strong wind stress curl anomalies are found south of  $20^{\circ}\text{N}$ . As they are located at the very western side of the basin, their impact on the subtropical ocean circulation will be mostly local through Ekman pumping. In chapter 3 it will be discussed how this could still add constructively to the effect that Rossby waves, generated by the wind stress anomalies at higher latitudes, have on the ocean circulation. Overall, the wind stress curl anomalies could provide a negative feedback in a coupled decadal North Pacific air-sea mode as suggested by Latif and Barnett (1994, 1996). One should note, however, that the variance of the wind stress curl response found in association with the decadal signal is only one fifth of the variance of the ENSO-related wind stress curl response which has a similar spatial structure. A coupled decadal North Pacific air-sea mode would therefore be subject to disruptions by internal atmospheric variability as well as ENSO-related interannual variability.

Whether the strong atmospheric response to equatorial Pacific SST changes or the somewhat weaker response to subtropical and midlatitudinal North Pacific SST changes are more important for the generation of decadal climate variability depends also on the oceanic processes that might be involved in possibly coupled mechanisms. The investigation of such oceanic processes is the subject of the next chapter.

## Chapter 3

# Ocean model experiments

In the previous chapter decadal fluctuations of the extra-tropical atmospheric circulation have been attributed to decadal variations of the underlying SSTs. In this chapter ocean processes that may be relevant for the generation of such SST changes will be examined. The investigation of the ocean dynamics will be restricted to the Pacific basin. As seen in the previous chapter, climate variability in the Pacific Ocean region is primarily characterised by interannual changes associated with the ENSO phenomenon, and only to a smaller extent is this region subject to decadal variations. There is an ongoing debate about the manner in which decadal fluctuations in the North Pacific might interact with changes in the equatorial Pacific.

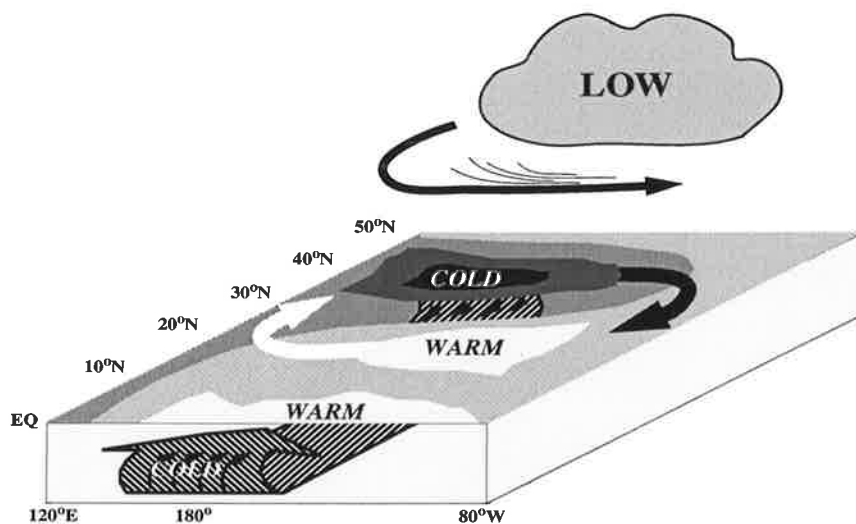


Figure 3.1: *Schematic diagram of ocean dynamics that could account for the decadal memory of the coupled ocean-atmosphere system in the Pacific region.*

It centers around three ideas: First, low-frequency modulations of ENSO, what-

ever their cause, could via atmospheric teleconnections be directly responsible for the decadal midlatitude fluctuations (Trenberth and Hurrell, 1994; Trenberth and Hoar, 1996). Alternatively, midlatitudinal decadal fluctuations could be an independent phenomenon and can exist independently of tropical variability (Latif and Barnett, 1994, 1996). The timescale of this *gyre-mode* would be set by the subtropical gyre circulation as indicated by the rotating anomalous heat content patches in the schematic diagram of Fig. 3.1. Finally, it has been proposed that tropical SST anomalies force via atmospheric teleconnections midlatitudinal SST anomalies which in turn may induce decadal changes in the equatorial ocean via an ocean teleconnection (Gu and Philander, 1997; Zhang et al., 1998). In this *subduction-mode* the timescale would be set by the equatorward propagation of North Pacific temperature anomalies through the interior of the ocean as schematically represent in Fig. 3.1 by the large dashed arrow. In the gyre-mode the inertia of the subtropical ocean gyre circulation provides memory on the timescale of decades and in the subduction-mode this is given by the adiabatic equatorward transport of North Pacific water underneath the ocean's mixed-layer.

From the results of the previous chapter none of the above hypotheses can be ruled out. To get further insight into the role of the ocean in the generation of decadal climate variability the relevant ocean dynamics will be studied using the Hamburg Ocean Primitive Equation model (HOPE). Prior to that, some aspects of ocean circulation theory which are important in this investigation will be briefly reviewed.

## 3.1 Dynamics of the subtropical gyre circulation

The dominant features of the large-scale extra-tropical Pacific ocean circulation are the subtropical gyres. In the North Pacific the subtropical gyre extends from about  $10^{\circ}\text{N}$  to about  $40^{\circ}\text{N}$ , and the water circulating in this massive pool reaches to about 1000 meter beneath the oceanic surface. The vigor of the gyre is intensified greatly in its western reach and a broad region of relatively weak flow occupies most of the gyre in the interior part of the basin in the so called Sverdrup regime described below.

### 3.1.1 The steady circulation

In the upper ocean there is a rich structure for the velocity field and the fields of temperature and salinity with depth. Beneath a surface layer of about 100m

that is mixed to homogeneity by the action of the winds and local heat loss to the atmosphere, the oceanic temperature decreases rapidly with depth in the main thermocline over the next 1000 m until cold water of clearly polar origins with uniform temperatures is reached. The radical departure of the vertical temperature profile for the mean state from a linear conductive gradient implies that dynamic processes are at work in forming the nonuniform structure of the thermocline.

### The Sverdrup balance

Current flow in the subtropical gyres is related to the overlying anticyclonic wind systems which blow around the subtropical high pressure regions. To a first approximation the wind-driven circulation can be described by the Sverdrup-balance (Sverdrup, 1947) according to which the meridional transport of water integrated over the entire depth of moving water is determined by the curl of the overlying wind stress:

$$\beta \int v dz = \mathbf{k} \cdot \frac{\nabla \times \boldsymbol{\tau}}{\rho} \quad (3.1)$$

where  $\beta = \frac{\partial f}{\partial y}$  represents the variation of the Coriolis parameter  $f$  with latitude,  $v$  is the meridional velocity,  $\mathbf{k}$  a vertical unit vector,  $\boldsymbol{\tau}$  represents the surface wind stress and  $\rho$  density. Sverdrup had abandoned any attempt to determine the details of the velocities as a function of depth. In the subtropical gyres  $\mathbf{k} \cdot \nabla \times \boldsymbol{\tau}$  is negative, and the total transport must move equatorward. Stommel (1948) demonstrated that for the reason of vorticity conservation this equatorward flow is compensated by intensified poleward transport along the western boundary.

### Ventilated layers in the thermocline

From the balance of Coriolis and pressure force, Ekman (1905) derived that in the wind-driven surface layer the tips of the horizontal velocity arrows at equal depth intervals form a vertically decreasing spiral ("Ekman spiral"). Vertical integration of these horizontal velocities over the directly wind-driven layer yields for the direct wind-driven horizontal transport:

$$\mathbf{V}_E = \int \mathbf{v} dz = -\frac{\mathbf{k} \times \boldsymbol{\tau}}{f\rho} \quad (3.2)$$

where  $\mathbf{v} = (u, v)$  is the horizontal velocity vector. In the subtropical gyres the Ekman transport is laterally convergent. This convergence produces a downwelling velocity

$$w_E = \mathbf{k} \cdot \nabla \times \frac{\boldsymbol{\tau}}{f\rho} \quad (3.3)$$

that is responsible for setting the deeper layers of the ocean in motion. This process is called Ekman pumping. The question is how deep motion can take place. Montgomery (1938) and Iselin (1939) observed that the vertical distribution of properties at depth were systematically related to their lateral distributions on the sea surface. Some advective process is therefore required to carry the surface signal into the thermocline. The surface of the ocean is not uniform in temperature and salinity. Roughly, the temperature decreases poleward so that surface isotherms run nearly east-west along the ocean's surface.

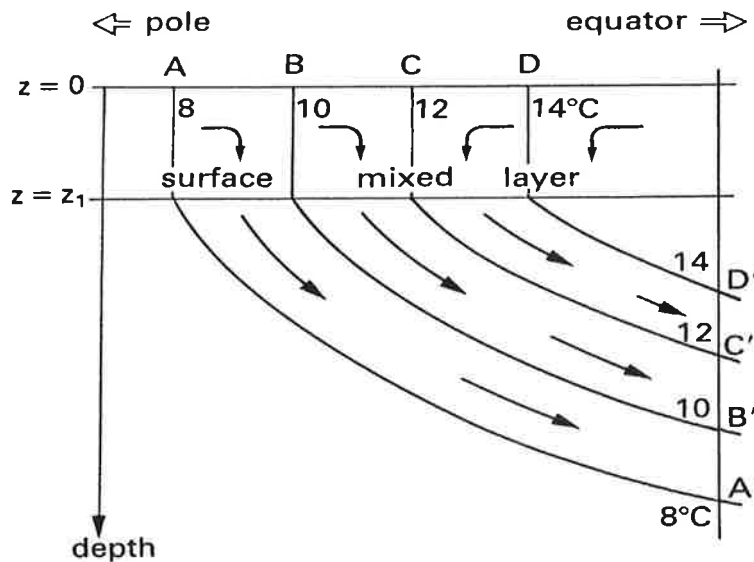


Figure 3.2: Sketch of water mass formation by subduction in the subtropical convergence.

The continuation of those isolines beneath the surface forms the topography of the density surfaces in the thermocline (e.g. Fig. 3.5). In the regions in which a certain density layer is in contact with the mixed surface layer (“outcrop regions”), it ingests fluid pumped down by the wind in accordance with equation 3.3 and sets the layer in motion. This process, which is known as *subduction*, is illustrated in Fig. 3.2.

Its imprint on the thermocline varies with the seasons, partly in response to variations in the strength of the Ekman pumping but mainly because of the seasonal

development of a seasonal thermocline: The summer mixed layer depth is shallower than the depth of the winter mixed layer. The water trapped between is available for subduction (Stommel, 1979). In order to derive the further path of the fluid which determines the structure of the thermocline, vorticity provides a useful tool. It will be considered later (section 3.4).

### 3.1.2 The spin-up

The previous section dealt with steady-state theories that intend to describe a conceptual time average of the circulation. The ocean circulation, however, is subject to variations on various timescales. In the subtropical gyre, for example, the adjustment time to changes in the wind stress forcing is of the order of weeks for the barotropic mode, while the baroclinic adjustment timescale is several years. As this thesis focuses on physical processes which have the potential to influence climate on decadal timescales, only the baroclinic response is examined. It gives useful insight into the nature of the ocean circulation and its transient behaviour which is expected to be of relevance for the decadal memory of the climate system. As derived by Gill (1982), the governing equation of the response is the linear potential vorticity equation including a forcing term  $F$  equal to the Ekman divergence. It reads on the beta plane at latitude  $\theta_0$ :

$$\frac{\partial}{\partial t} \left( \frac{\partial^2 \eta}{\partial x^2} + \frac{\partial^2 \eta}{\partial y^2} - \frac{f_0^2}{c^2} \eta \right) + \beta \frac{\partial \eta}{\partial x} = F, \quad (3.4)$$

$$F = \frac{f}{\rho g H} \mathbf{k} \cdot \nabla \times \boldsymbol{\tau}$$

where  $\eta$  is the sea surface elevation (or sea level),  $c$  is the gravity wave speed of the baroclinic mode considered,  $f$  denotes the Coriolis parameter and  $\beta = \frac{\partial f}{\partial y}$  its meridional derivative.  $H$  is a measure of how well the wind stress projects onto the mode, the so-called forcing depth. The zonal and meridional wind stress are denoted by  $\tau_x$  and  $\tau_y$ . The free wave solutions of this equation ( $F \equiv 0$ ) are the planetary Rossby waves. With the plane wave ansatz  $\eta = \eta_0 \exp[i(kx + ly - \omega t)]$  the dispersion relation and group velocity  $c_g$  can be derived from (3.4). For the latter one obtains

$$c_g = \beta \frac{k^2 - l^2 - R^{-2}}{(k^2 + l^2 + R^{-2})^2} \quad (3.5)$$

with  $R = c/f$  being the Rossby radius. The group velocity reaches its maximum speed  $\beta R^2$  for the largest scale modes, i. e. if both  $k$  and  $l$  vanish. For these basin

size waves the group velocities are negative, and the waves are moving to the west. Equation (3.4) allows eastward traveling waves as well. These are, however, too short to be relevant to the large-scale decadal variations considered here. For constant forcing  $F$  Anderson and Gill (1975) note two solutions of the forced problem (3.4). The space independent solution

$$\eta(t) = -R^2 F t \quad (3.6)$$

and the time independent Sverdrup solution

$$\eta(x) = F \beta^{-1} x. \quad (3.7)$$

They show how these solutions transform from (3.6) to (3.7) in response to a suddenly applied wind stress. Fig. 3.3 illustrates the numerically determined solution of (3.4) as a function of longitude for the case of an eastward wind stress varying sinusoidally with latitude.

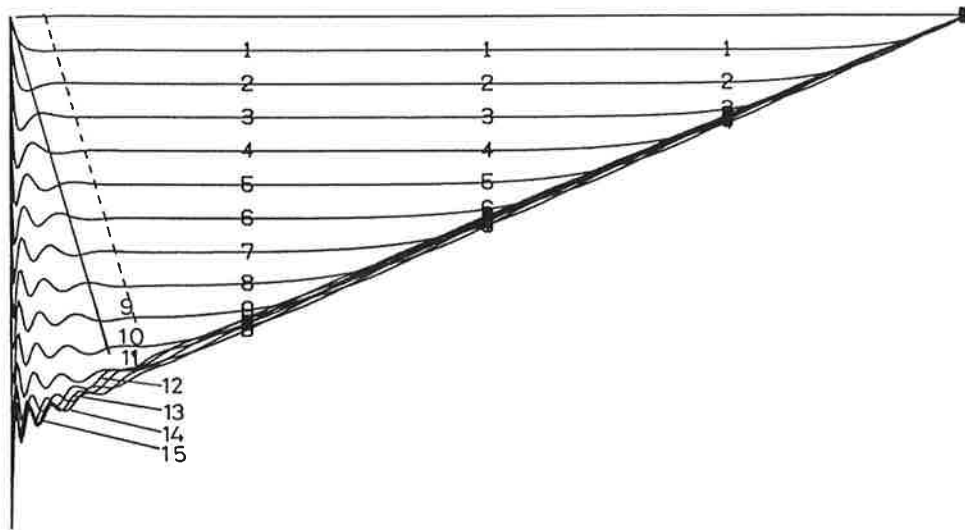


Figure 3.3: *The numerically determined solution of (3.4) as a function of longitude (east to the right) for the case of an eastward wind stress varying sinusoidally with latitude (from Anderson and Gill, 1975).*

The diagram shows the displacement of the thermocline (which is equivalent to sea level changes of opposite sign) for a baroclinic mode at different times (marked 1-15) after the wind is switched on at time zero. The thermocline is moving uniformly downward through Ekman pumping until boundary effects are felt. Long planetary

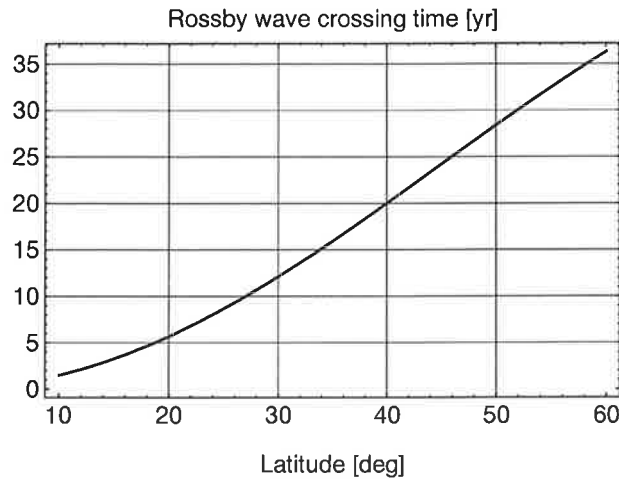


Figure 3.4: *Dependence of the traveling time of the longest Rossby wave across the Pacific on latitude. The Pacific basin is approximated by a sector of  $100^\circ$  longitude. The baroclinic gravity wave speed is set to  $2.6\text{m/s}$ .*

waves, moving out westward from the eastern boundary, establish a Sverdrup balance with a uniformly sloping thermocline almost as soon as they arrive. Near the western boundary slowly eastward propagating waves can be seen. As mentioned above, these are not relevant to the large-scale decadal variations considered here. The dependence of the Rossby wave speed on  $\beta$  makes the basin crossing time strongly dependent on the latitude  $\theta_0$ . The typical Rossby wave crossing times in the North Pacific are illustrated in Fig. 3.4. The transit time quadruples from about five years in the subtropics near  $20^\circ\text{N}$  to about 20 years in midlatitudes near  $40^\circ\text{N}$ . Whether decadal climate fluctuations in the North Pacific region are related to Rossby waves is the central question addressed in section 3.3. It will be investigated by using the HOPE model which is described in the next section.

## 3.2 Ocean model and experimental design

### 3.2.1 The ocean model

The ocean model used is the Hamburg Ocean Primitive Equation model (HOPE – Wolff et al., 1997). It is based on the nonlinear balance equations for momentum (the equations of motion), the continuity equation for an incompressible fluid and the conservation equations for temperature and salinity. It employs the hydrostatic and Boussinesq approximations. The prognostic variables are temperature, salinity,

horizontal velocities and sea surface elevation.

The horizontal momentum balance equations are:

$$\frac{d\mathbf{v}}{dt} - f(\mathbf{k} \times \mathbf{v}) = -\frac{1}{\rho_0}[\nabla_H(p + \rho_0 g \eta)] + \nabla_H A_H \nabla_H \cdot \mathbf{v} + \frac{\partial}{\partial z}(A_V \frac{\partial \mathbf{v}}{\partial z}) \quad (3.8)$$

where  $\mathbf{v} = (u, v)$  is the horizontal velocity vector,  $f$  the Coriolis parameter,  $\mathbf{k}$  a vertical unit vector,  $\rho_0$  a reference density,  $\nabla_H$  the horizontal gradient operator,  $p = g \int_0^h \rho dz$  the internal pressure,  $\eta$  the sea level,  $A_H$  the horizontal and  $A_V$  the vertical turbulent viscosity coefficients. Using the hydrostatic approximation the internal pressure is computed from

$$\frac{\partial p}{\partial z} = -g\rho. \quad (3.9)$$

The vertical velocity is computed diagnostically from the incompressibility condition:

$$\frac{\partial w}{\partial z} = -\nabla \cdot \mathbf{v} \quad (3.10)$$

The sea level is computed from the linearised kinematic boundary condition:

$$\frac{\partial \eta}{\partial t} = w(z=0) = \nabla \cdot \int_{-H}^0 \mathbf{v} dz \quad (3.11)$$

where  $H(\phi, \lambda)$  is the water depth.

The density is computed with a nonlinear polynomial depending on salinity, temperature and pressure (UNESCO, 1983). In the case of static instabilities convective adjustment is applied, i.e. each pair of vertically adjacent unstably stratified layers is vertically mixed with heat and salt being conserved. Salinity and temperature are determined from the prognostic equations

$$\frac{dT}{dt} = \frac{\partial}{\partial z}(D_V \frac{\partial T}{\partial z}) + D_H \nabla_H^2 T \quad (3.12)$$

$$\frac{dS}{dt} = \frac{\partial}{\partial z}(D_V \frac{\partial S}{\partial z}) + D_H \nabla_H^2 S \quad (3.13)$$

where  $D_H$  and  $D_V$  are the horizontal and vertical eddy diffusivity coefficients.

Bottom friction is computed applying a Newtonian friction law. No-slip boundary conditions are used at lateral boundaries. The model domain used here is limited to the Pacific Ocean (120°E–70°W, 55°S–67°N) and has a realistic bottom topography.

The model has a  $2.8^\circ$  resolution, with the meridional resolution gradually increased to  $0.5^\circ$  within the region  $10^\circ\text{N}$  to  $10^\circ\text{S}$ . Vertically, there are 20 irregularly spaced levels, with ten levels within the upper 300 m. The numerical scheme uses the Arakawa E-grid (Arakawa and Lamb, 1977) with a two-hour time step. A 360-day year subdivided in 12 equal-length months of 30 days is used. There is no diurnal cycle in the forcing fields.

The momentum flux through the sea surface at  $z = 0$

$$\tau = \rho_0 A_V \frac{\partial \mathbf{v}}{\partial z} \quad (3.14)$$

is given by the wind stress forcing specified below. Furthermore, surface heat flux forcing is imposed. No explicit fresh water flux forcing is provided, as previous studies (Xu et al., 1998) showed that the fresh water flux plays only a minor role for decadal North Pacific climate variations. Instead, a Newtonian relaxation is employed to restore the surface salinity within the whole domain to the climatology of Levitus (1982) using a time constant of 40 days. Further details can be found in the model documentation (Wolff et al., 1997).

### 3.2.2 Atmospheric forcing

#### Climatological forcing

Monthly climatologies of surface heat flux and wind stress were generated from an integration of the atmospheric GCM ECHAM-3 (Roeckner et al., 1992) forced by the same GISST data set (Parker et al., 1995) that was introduced in the previous chapter. Daily values of surface heat flux and wind stress were obtained by linear interpolation. After initialising the ocean model with three dimensional temperature and salinity fields derived from the climatology of Levitus (1982), it was spun up for 30 years with this climatological forcing, at which point a realistic climatological ocean state was reached for the upper Pacific Ocean. The simulated mean subsurface temperature structure is in good agreement with the observed thermal structure. This is illustrated by means of an isopycnal surface in the thermocline (Fig. 3.5 and Fig. 3.6), which will be the focus in the final section of this chapter. In both the observations and the model, the depth of the  $1025 \text{kgm}^{-3}$  surface exceeds the mixed layer depth over much of the subtropical gyre. There is a clear trough-ridge structure oriented in the west-east direction. The sharp temperature gradient on the  $1025 \text{kgm}^{-3}$  surface at the equator is due to the inflow of warm and salty water

from the South Pacific into the equatorial thermocline. Overall, the climatological state of the upper Pacific Ocean is reproduced very well by the HOPE model.

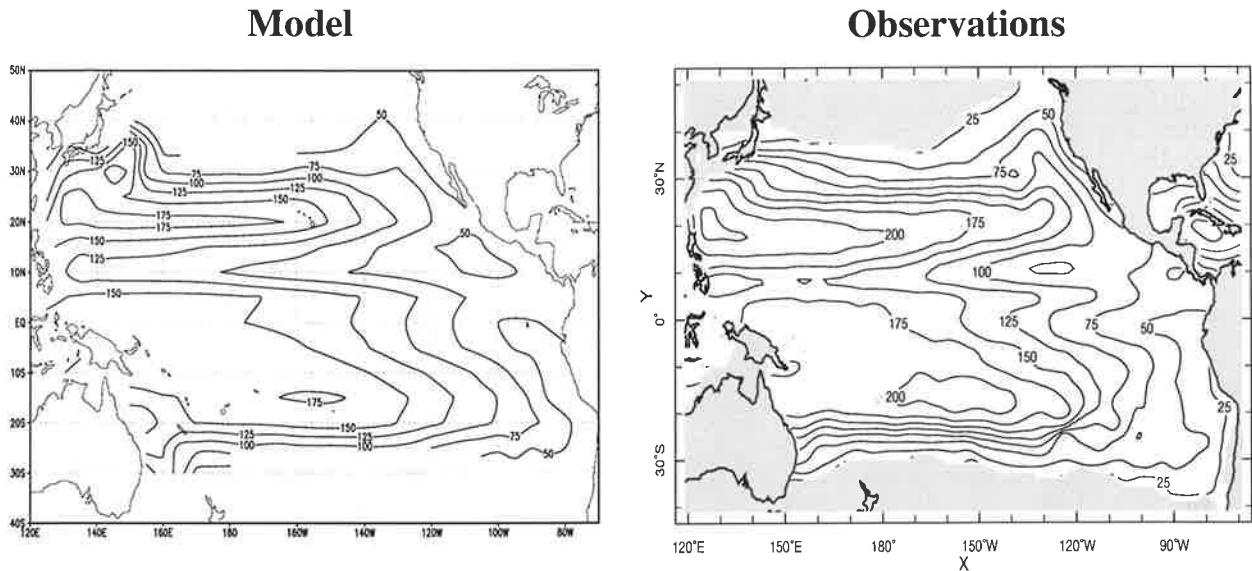


Figure 3.5: Mean depth [m] of the  $1025\text{kgm}^{-3}$  isopycnal surface as simulated by the HOPE model and as deduced from observations (Levitus, 1982)

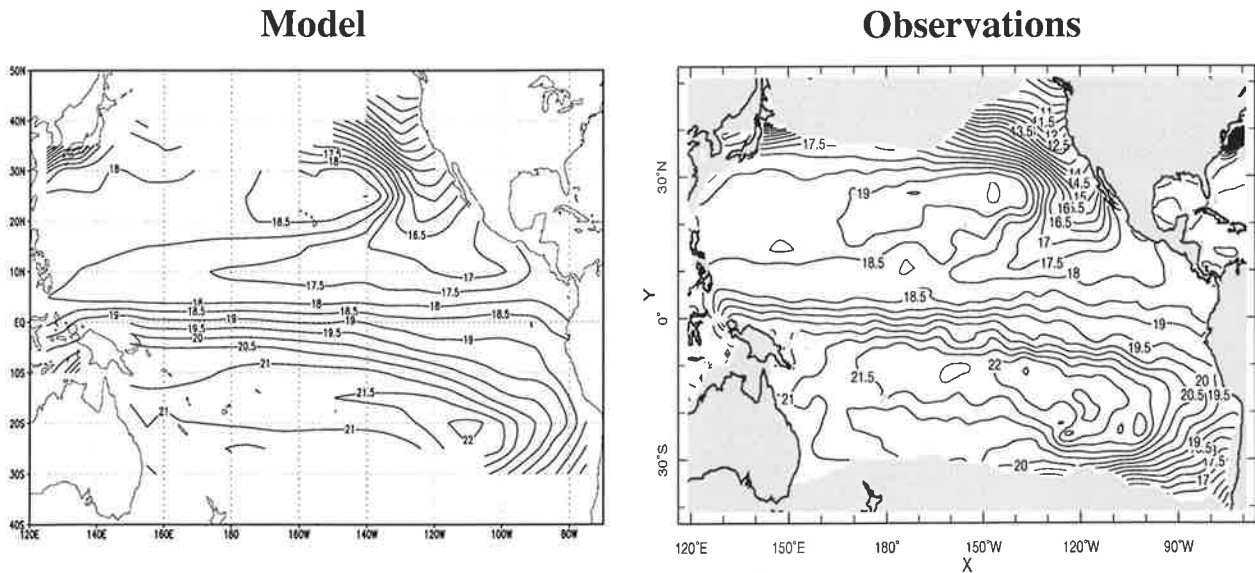


Figure 3.6: Mean temperature [ $^{\circ}\text{C}$ ] on the  $1025\text{kgm}^{-3}$  isopycnal surface as simulated by the HOPE model and as deduced from observations (Levitus, 1982)

### Idealised decadal wind stress forcing

In the previous chapter a consistent response of the atmospheric circulation over the North Pacific to underlying decadal SST changes was detected (Figs. 2.11 and 2.12). To investigate the origin of such atmospheric response to the extra-tropical anomalous SST pattern more closely, Latif and Barnett (1994) forced the ECHAM-3 model by an SST pattern similar to that shown in Fig. 2.11c, but they entirely neglected tropical SST anomalies. The integration was done in perpetual January mode, and an ensemble of 12 January integrations was performed. The resulting wind stress anomaly pattern over the North Pacific and its curl (Fig. 3.7) resemble quite closely those detected in section 2.4. Two experiments were performed in which the wind stress pattern of Fig. 3.7 was superimposed onto the climatological forcing. In the experiment *SPINUP* the anomalous wind stress is suddenly switched from zero to full magnitude, and in the experiment *PERIO* the amplitude varies sinusoidally with a period of 20 years.

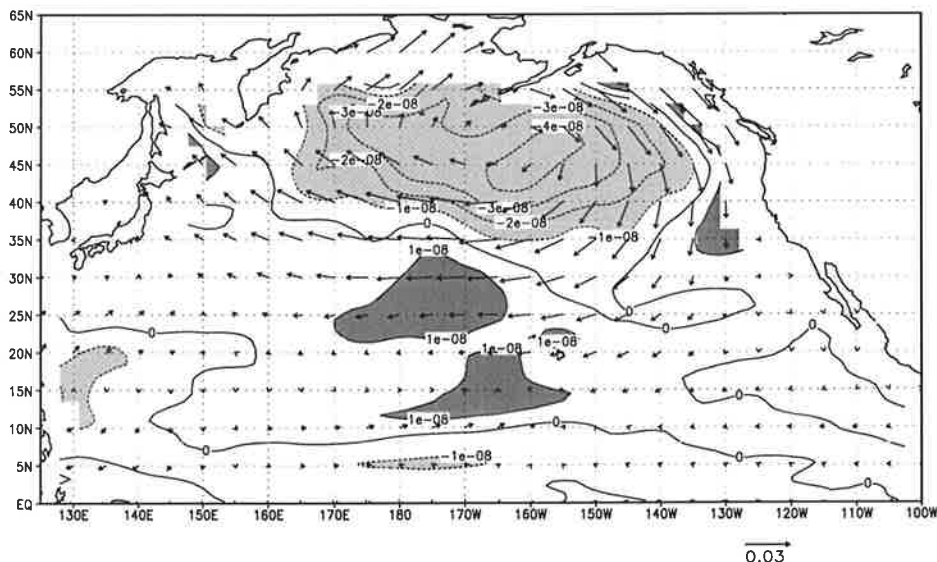


Figure 3.7: Response of the atmospheric GCM ECHAM-3 to a large-scale positive SST anomaly in the central North Pacific (see Latif and Barnett (1994) for details). Shown is the resulting wind stress anomaly [Pa] and its curl [Pa/m] over the North Pacific.

### Observed anomalous atmospheric forcing

Observed surface heat flux and wind stress anomalies have been derived from the COADS data set for the years 1949 to 1994 (da Silva et al., 1994). In the experiment

Experiment	anomalous atmospheric forcing	integration time
SPINUP	$\tau' = \tau'_{decadal}$ ( $\rightarrow$ pattern shown in Fig. 3.7)	15 years
PERIO	$\tau' = \tau'_{decadal} \sin(\frac{2\pi}{20years}t)$	40 years
COADS	$\tau' = \tau'_{COADS}$ $Q' = Q'_{COADS} + 40 \frac{W}{m^2K} (T_{GISST} - T_{HOPE})$	45 years

Table 3.1: Overview of the experiments discussed in section 3.3.

*COADS*, these are superimposed onto the climatological forcing of the ocean model. Furthermore, the model SSTs are restored to the observations using a time constant of 23 days.

### 3.3 Decadal changes in the North Pacific gyre circulation

#### 3.3.1 Spin-up by suddenly applied anomalous wind stress

In the experiment *SPINUP*, the wind stress pattern shown in Fig. 3.7 was suddenly superimposed onto the climatological atmospheric forcing for 15 years. The anomalous wind stress drives an Ekman transport in the surface layers towards the latitude at which the anomalous surface air pressure has a maximum and away from the latitude at which the anomalous pressure has a minimum, i.e. towards the latitude at which the wind stress changes sign in midlatitudes and away from the latitude at which the wind stress changes sign in the subtropics. The baroclinic response of the ocean to the superimposed anomalous wind stress pattern is therefore a raising of the thermocline in the subtropics (which is equivalent to a decrease in sea level) and a deepening of the thermocline in midlatitudes (which is equivalent to an increase in sea level).

The associated temporal anomalous sea level evolution as simulated by the HOPE model in response to the characteristic decadal wind stress pattern (Fig. 3.7) is shown in Fig. 3.8. It resembles very well the solution of Anderson and Gill (1975) shown in Fig. 3.3. While in the subtropics the new Sverdrup balance is already established after about four years, it takes about a decade before a steady state is reached in midlatitudes. This is due to the decrease of the Rossby wave speed with

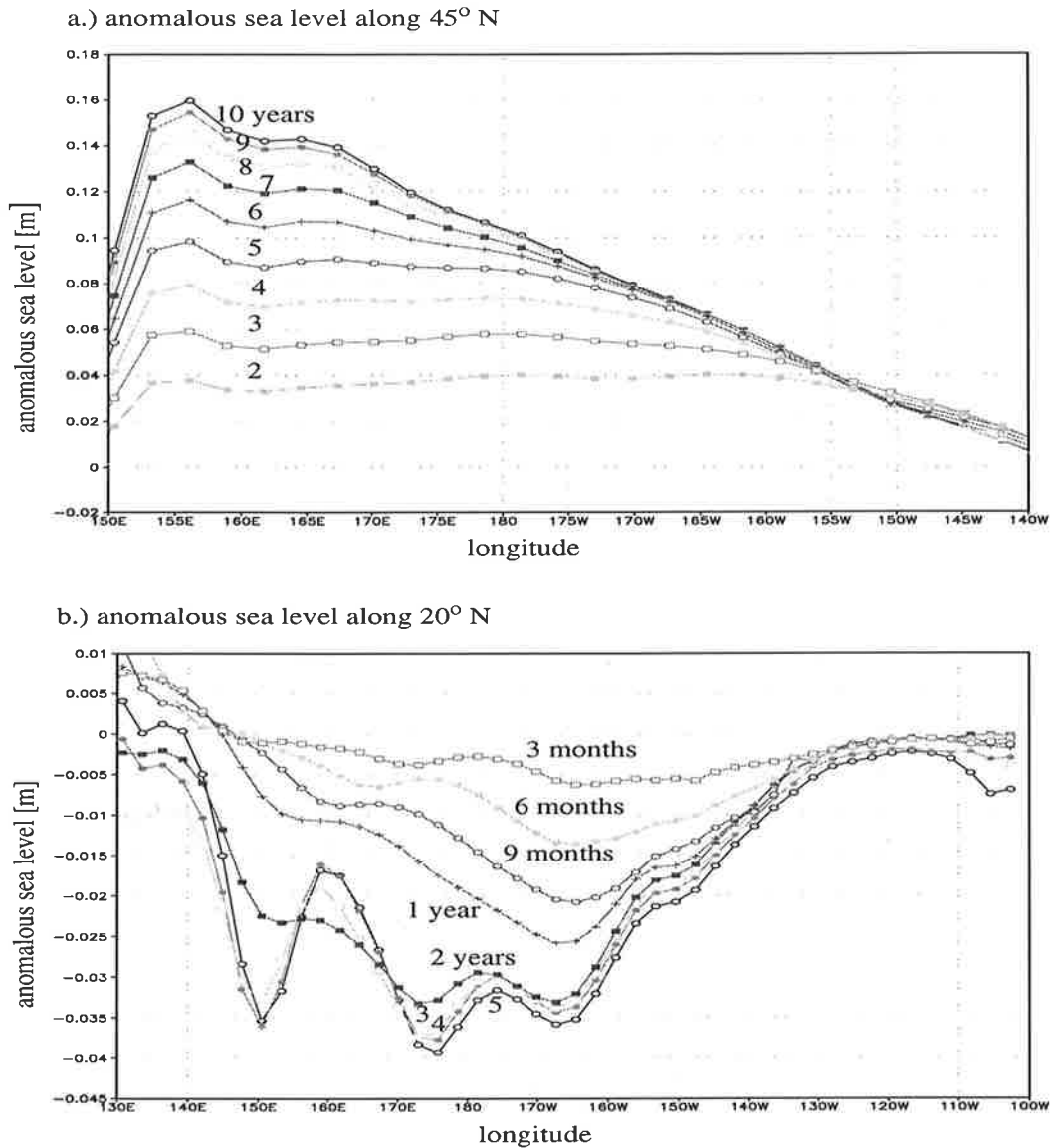


Figure 3.8: Anomalous sea level [m] (a) in midlatitudes (along  $45^\circ\text{N}$ ) and (b) the subtropics (along  $20^\circ\text{N}$ ) as simulated by the HOPE model at different times after the wind stress anomaly shown in Fig. 3.7 was switched on.

latitude as shown in Fig. 3.4.

In summary, the experiment *SPINUP* demonstrates that the adjustment of the North Pacific Ocean to a wind stress anomaly that is characteristic for long-term North Pacific climate fluctuation takes about a decade. Thus, wind stress induced gyre circulation changes are indeed capable of providing a decadal memory for the coupled ocean-atmosphere North Pacific climate system.

### 3.3.2 North Pacific response to decadal wind stress changes

According to the hypothesis of Latif and Barnett (1994, 1996) anomalous North Pacific SSTs cause wind stress curl anomalies which lead to changes in the gyre circulation and hence a changed meridional oceanic heat transport which in turn weakens the initial SST anomaly in the central North Pacific. This will eventually reverse the phase of the coupled ocean-atmosphere mode which they proposed. To simulate the oceanic part of this scenario, the characteristic decadal wind stress anomaly pattern (Fig. 3.7) was superimposed in the experiment *PERIO* onto the climatological forcing of the HOPE model with a sinusoidally varying amplitude. The period was chosen to be 20 years.

Snapshots of the resulting sea level anomalies through half a cycle are shown in Fig. 3.9. They exhibit the same characteristics as revealed by Complex Empirical Orthogonal Function (CEOF) analysis of upper ocean heat content observations (Tourre et al., 1998) and coupled ocean-atmosphere models (Latif and Barnett, 1994, 1996). While Latif and Barnett (1994, 1996) describe the westward propagation in the subtropics and the eastward spreading along the Kuroshio extension, Tourre et al. (1998) focus on the westward propagation in the subtropics and midlatitudes. Three different bands of sea level variability are emphasised in the Hovmöller diagrams of Fig. 3.10.

Westward propagating Rossby waves can be seen in the subtropical North Pacific (left panel). Maxima of the sea level anomalies are found slightly to the west of the maxima of the wind stress curl anomaly in phase with the amplitude of the forcing. Westward propagating sea level anomalies are also found in midlatitudes (right panel). As the Rossby wave speed decreases at higher latitudes, the sea level anomalies west of the region of strong wind stress curl anomalies are lagging the forcing amplitude in this region. As expected from the findings of Anderson and Gill (1975), the lag increases towards the west. Between the two bands of westward propagating sea level anomalies there is a band of almost zero wind stress curl anomalies (Fig. 3.7) at the latitude of the Kuroshio extension (around 35°N). Here, eastward propagating sea level anomalies are simulated (Fig. 3.10, middle panel). In the western part of the basin these are not directly forced by the anomalous wind stress but result from the gyre-adjustment (established by the Rossby waves in higher and lower latitudes). The maximum sea level anomalies in the eastern central North Pacific are again directly forced by the local wind stress curl anomalies.

The delayed response to the anomalous wind stress forcing can be separated from

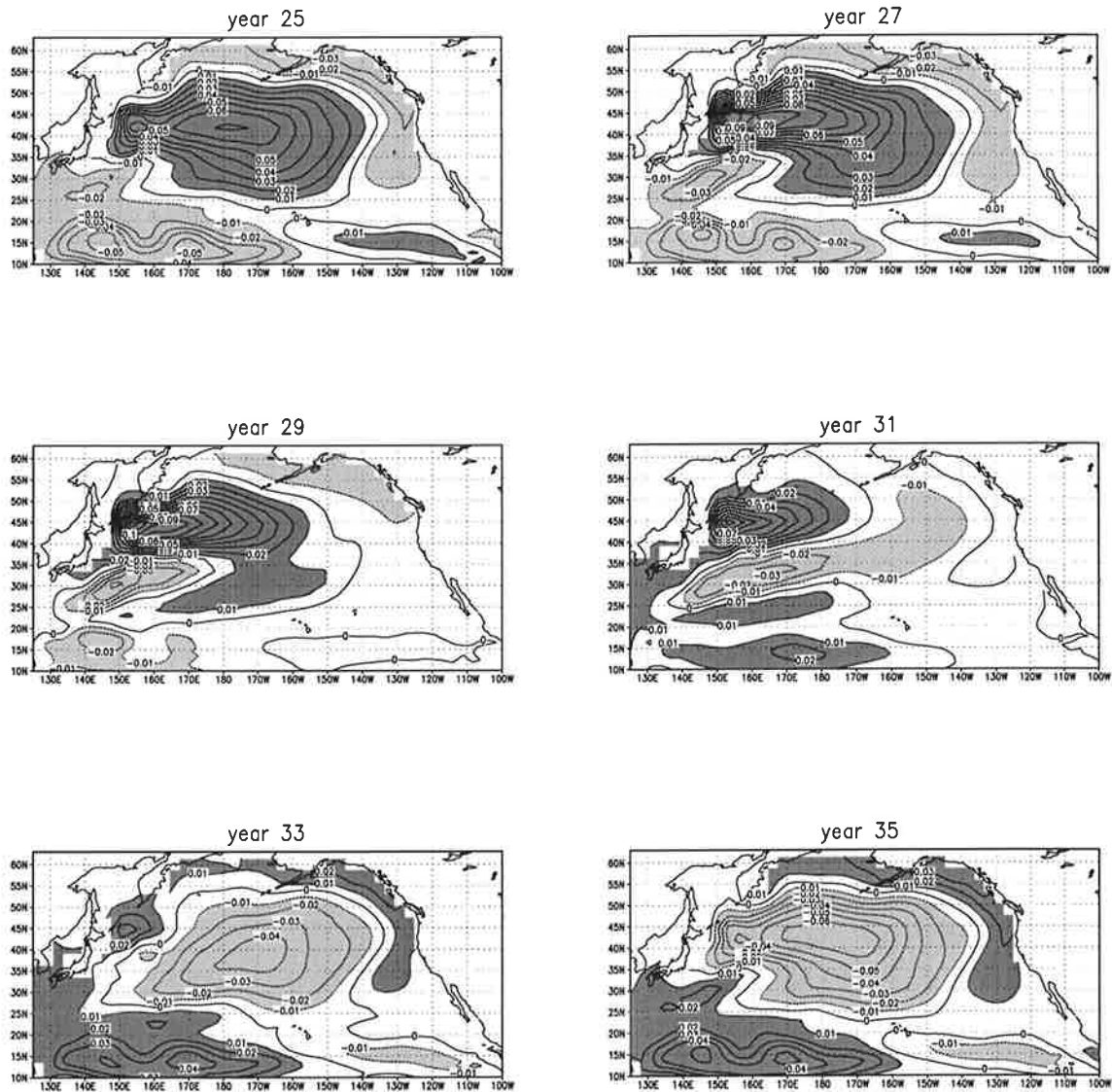


Figure 3.9: Snapshots of North Pacific sea level anomalies [m] in the course of half a forcing period as obtained from the HOPE model forced by spatially fixed decadal wind stress anomalies from Fig. 3.7 following sinusoidal amplitude variations with a period of 20 years.

the direct Ekman response by an EOF analysis.

The first EOF of the anomalous sea level (Fig. 3.11b) represents the direct response to the wind stress anomalies. It explains 80% of the total variance and is dominated

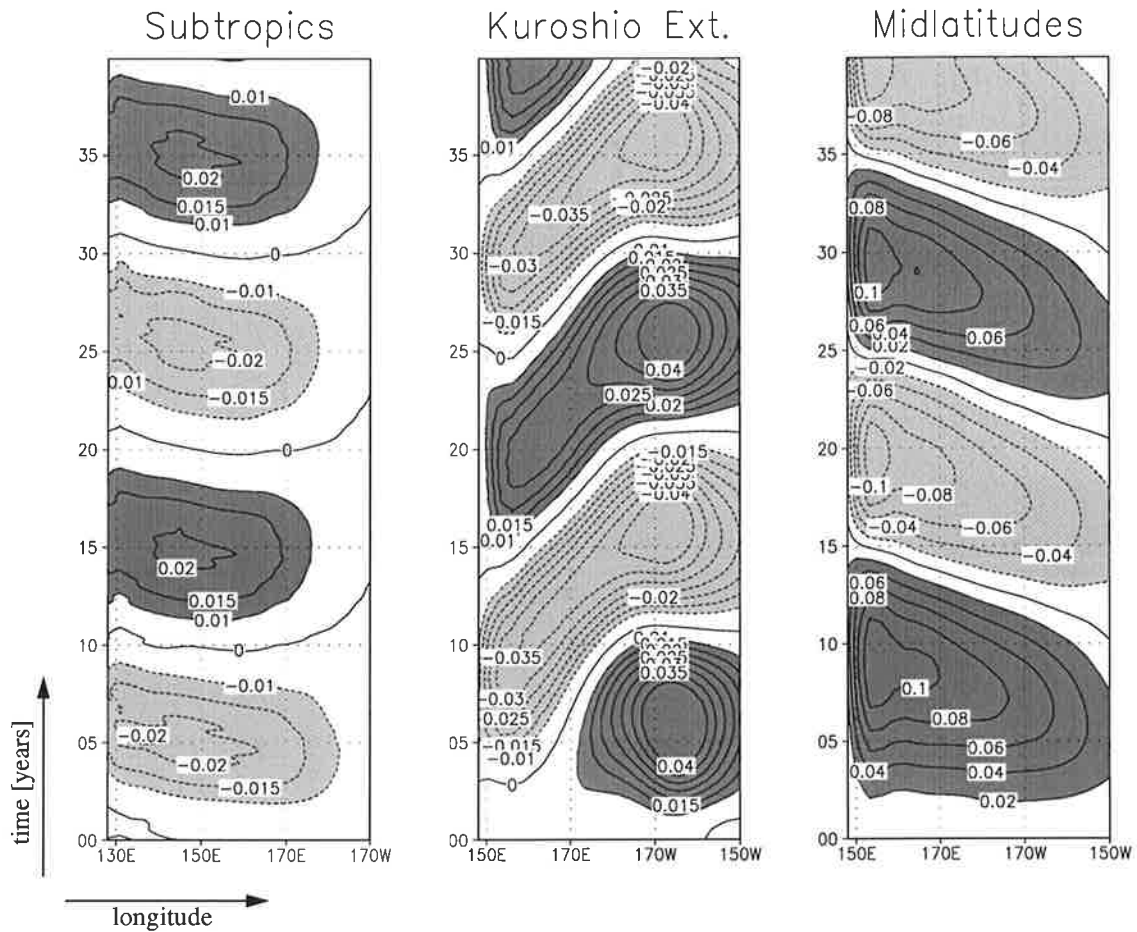


Figure 3.10: Hovmöller diagrams of sea level anomalies [m] from the same experiment as figure 3.9 averaged over the subtropical ( $18\text{--}23^\circ\text{N}$ ) and midlatitudinal ( $40\text{--}45^\circ\text{N}$ ) North Pacific as well as the Kuroshio extension ( $33\text{--}38^\circ\text{N}$ ).

by large-scale anomalies in the central and northwestern North Pacific which are surrounded by anomalies of opposite sign with highest amplitudes in the subtropics. This situation is described by Tourre et al. (1998) as the end of the “growth phase” of the observed decadal cycle. The associated principle component (PC) lags the forcing by about one year. The second EOF of the anomalous sea level (Fig. 3.11c) represents the delayed response. While the sea level anomalies in the northwestern part of the basin have decayed and those in the eastern subtropics moved westward, sea level anomalies of opposite sign have spread from the western subtropical region into the central North Pacific. PC-1 and PC-2 are  $90^\circ$  out of phase. The North Pacific SST anomalies vary in phase with the sea level changes (Fig. 3.11a, b, e).

In the gyre-mode hypothesis of Latif and Barnett (1994, 1996) EOF-2 follows EOF-1

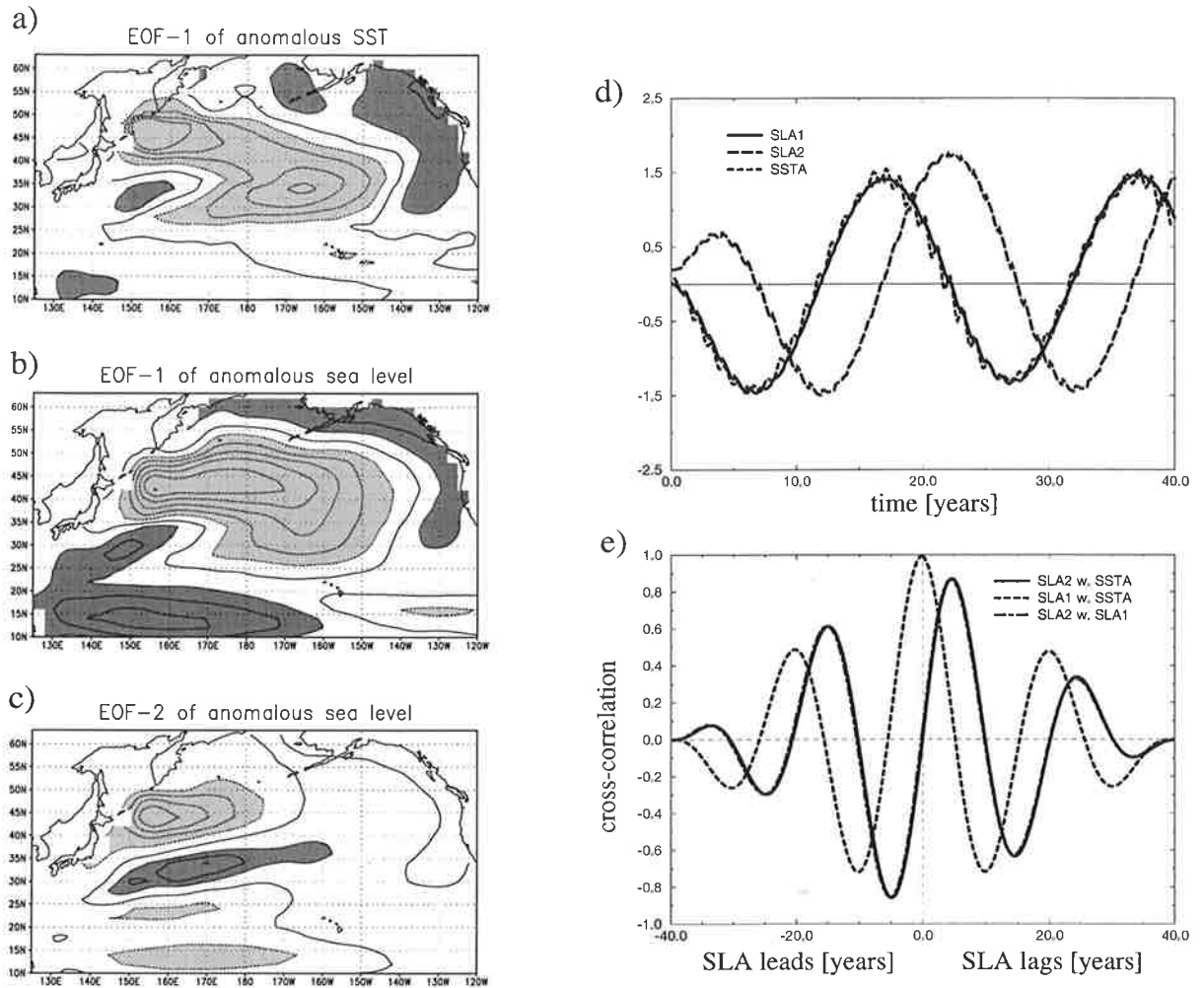


Figure 3.11: (a) First EOF of anomalous SST (explaining 61% of the total variance), (b) first EOF of anomalous sea level (80%) and (c) second EOF of anomalous sea level (17%) together with (d) the associated principle components and (e) their lag-correlation functions. The data was obtained from the same experiment as in Fig. 3.9 and 3.10.

due to oceanic circulation changes caused by SST-induced wind stress curl changes. EOF-2 then develops into EOF-1 with opposite polarity due to SST-induced heat flux anomalies. Atmospheric circulation changes that are forced by extra-tropical SST anomalies were the subject of chapter 2. In the simple coupled model of Münnich et al. (1998) the feedbacks between the ocean and the atmosphere were simply parameterised by linking the amplitude of the wind stress anomaly shown in Fig. 3.7 directly to the thermocline depth that is simulated by their ocean model near the western boundary. The ocean model solves the linear potential vorticity equation on the beta plane at latitude  $\theta_0$  (equation 3.4) and does not include

any advective processes. Oceanic variability in midlatitudes and in the subtropics is therefore governed by Rossby wave propagation similar to that described above (Fig. 3.10) but does not show (by definition) any eastward advection of thermal anomalies at the latitude of the Kuroshio extension. The latter is parameterised by a delay of the atmospheric coupling to the thermocline depth near the western boundary. For suitable parameter choices, this simple model has produced decadal oscillations. They are weakly damped with a period of 16 years (Fig. 3.12a). Such

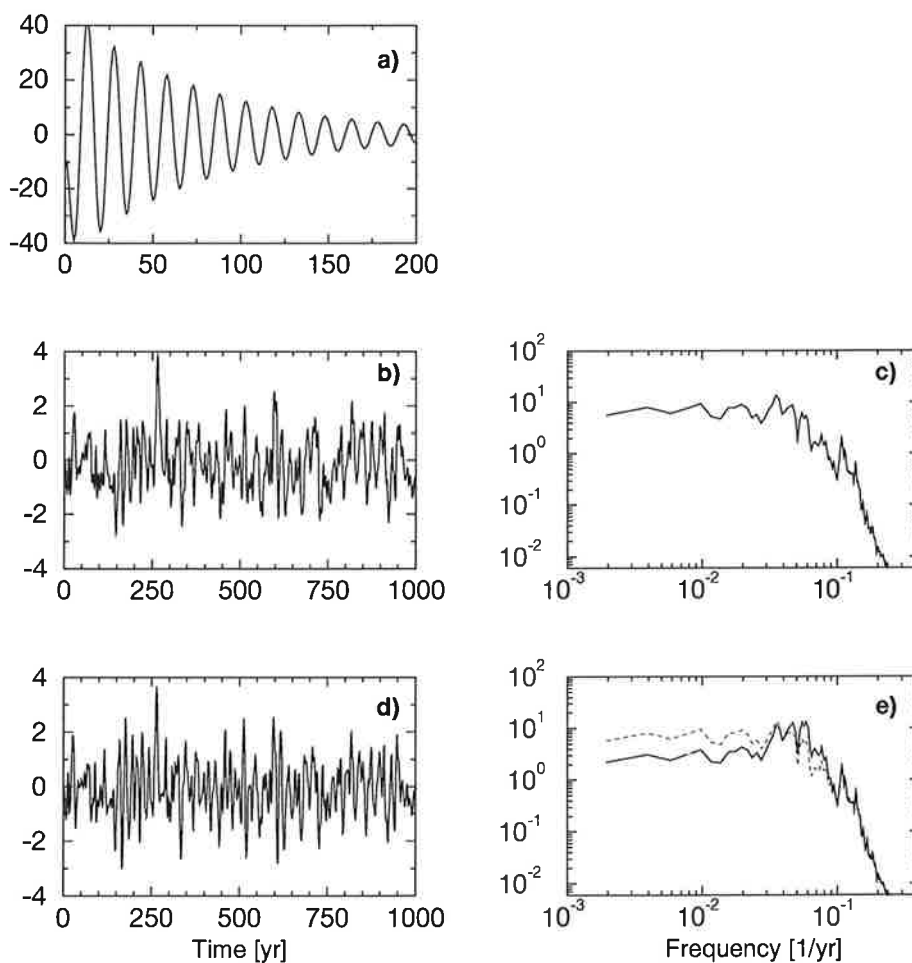


Figure 3.12: Scaled time series and spectra of thermocline depth anomalies in the index region  $14^{\circ}\text{E}$ – $15^{\circ}\text{E}$ ,  $37^{\circ}\text{N}$ – $39^{\circ}\text{N}$ . The forcing used for a) includes coupling of the wind stress amplitude to this index region. In b) the forcing is white in time. c) Shows the spectrum of b). In d) the forcings of a) and b) are superimposed. The spectrum of d) is shown in e) (solid). Spectrum c) is redrawn in e) (dashed) to ease comparison of the spectra. Further details can be found in Münnich et al. (1998).

a regular coupled ocean-atmosphere oscillation would represent an optimally predictable mode of decadal climate variability but is not apparent in the real world due to weather noise over the North Pacific. Frankignoul et al. (1997) extended Hasselmann's stochastic climate model by introducing Rossby wave dynamics. They showed that stochastic atmospheric forcing and Rossby wave dynamics can lead to a red spectrum of oceanic fields up to decadal timescales. Distinct spectral peaks, however, cannot be explained with their simple model in which the ocean only responds to atmospheric noise but has no impact of the atmospheric forcing itself. Münnich et al. (1998) incorporated spatially coherent (Fig. 3.7) but temporarily uncorrelated stochastic wind stress forcing in their model. In the absence of any feedback from the ocean to the atmosphere, the resulting spectrum of thermocline depth variability at the western boundary is red as predicted by Frankignoul et al. (1997), and no decadal peak is visible (Fig. 3.12c). When the feedback is reintroduced, a broad spectral peak at a period of about 17 years is superimposed on the red spectrum (Fig. 3.12e).

These results demonstrate that the above discussed decadal gyre-scale circulation changes, which involve planetary wave propagation as well as advective processes (the latter had to be parameterised in Münnich et al., 1998), in conjunction with weak ocean-atmosphere coupling and additional internal atmospheric variability can give rise to decadal climate variability that resembles the observed characteristics. One therefore may conclude that the most likely scenario for decadal North Pacific climate variability is the stochastically forced weakly coupled wind-driven ocean-atmosphere oscillator. This is an important conclusion that will be highlighted again in the final chapter of this thesis.

### 3.3.3 Predictability of observed decadal North Pacific temperature changes

The concept of the *delayed-action oscillator* (e.g. Suarez and Schopf, 1988) describes the basic dynamics of ENSO. Similarly, the above results suggest for the North Pacific Ocean that perturbations due to long-term anomalous wind stress forcing do not simply dissipate, once the anomalous atmospheric forcing vanishes. Rather, they determine a characteristic further evolution of the upper ocean temperatures. This means, for instance, that whenever anomalous wind stress conditions similar to those shown in Fig. 3.7 are observed over a longer period, heat content anomalies of the structure shown in Fig. 3.11b will be established and evolve into the structure

shown in Fig. 3.11c in the absence of any further atmospheric forcing. To demonstrate that this evolution is mainly determined by the oceanic initial conditions and does not require any further atmospheric forcing, some additional experiments were performed. In one experiment, the ocean model was initialised after year 28 of the experiment *PERIO*. At this time EOF-1 had maximum amplitude. Thereafter, the HOPE model was forced by climatological surface heat fluxes and wind stresses only. While the subtropical sea level anomalies damp out quite quickly, Rossby wave propagation can be followed for several years in midlatitudes (Fig. 3.13).

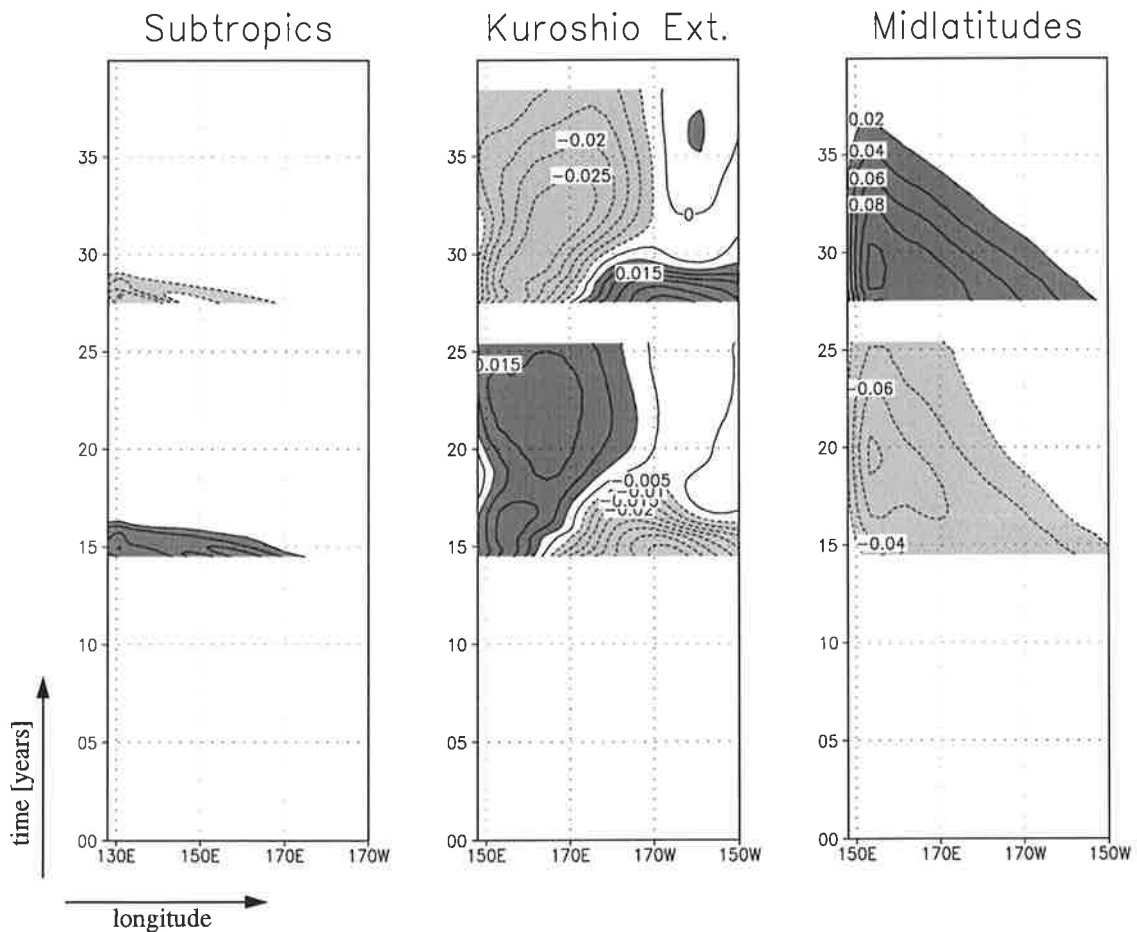


Figure 3.13: Hovmöller diagrams of sea level anomalies [m] from ocean-only experiments initialised after year 15 and year 28 of the *PERIO* experiment averaged over the same regions as in Fig. 3.10.

At the latitude of the Kuroshio extension negative anomalies spread eastward and replace the initial warm conditions in the central North Pacific similar to the control integration with periodic forcing (*PERIO*). Due to the lack of atmospheric feedbacks,

however, they are not amplified and restricted to the western central North Pacific. Projections of sea level anomalies from this ocean-only “forecast” onto the EOFs of Fig. 3.11 reveal that while the principal component of EOF-1 is monotonically decaying, the principal component of EOF-2 grows (starting from zero) for three years before it starts to decay. This confirms that gyre-scale oceanic circulation changes can provide the negative feedback required in a coupled ocean-atmosphere mode like the one proposed by Latif and Barnett (1994, 1996). If the model is initialised with opposite polarity (e.g. after year 15) the sea level anomalies evolve in the same way but with opposite sign. This proves that the cooling of the central North Pacific found in the “forecast” that was initialised after year 28 does not simply reflect a general tendency of the model to cool when the anomalous forcing is switched off.

In summary, the results from these idealised experiments indicate that long-term changes in the thermal structure of the upper central North Pacific Ocean may be predicted from initial oceanic conditions at a few years lead-time. One should note at this point, however, that such predictability is limited by atmospheric variability on a range of timescales, generating additional oceanic perturbations. It needs to be investigated if the characteristics of the discussed oceanic variations can also be found in a more realistic simulation of the North Pacific upper ocean temperatures, and hence if certain decadal changes could have been predicted.

While idealised atmospheric forcing was used in the experiment *PERIO*, observed atmospheric forcing was used in the experiment *COADS*. In Fig. 3.14 Hovmöller diagrams of sea level anomalies simulated in the *COADS* experiment are shown in analogy to Fig. 3.10. The *COADS* simulation reproduces the observed North Pacific upper ocean temperature evolution remarkably well as will be seen in more detail later (section 3.4). In agreement with the findings from the experiment *PERIO*, westward propagating sea level anomalies are found in the subtropics and midlatitudes while, especially during the late 1970s and late 1980s, sea level anomalies tend to propagate eastward in the region of the Kuroshio extension. An EOF-analysis further confirms the findings from *PERIO*. Fig. 3.15 shows in analogy to Fig. 3.11 that the long-term sea level variability can be separated into a direct and a delayed response which are described by the first two leading EOFs. The first EOF varies in phase with the first EOF of the anomalous SST. The first and the second PCs of the anomalous sea level have their maximum correlation when PC-1 leads PC-2 by about eight years and their maximum anticorrelation when PC-1 lags PC-2 by about eight years. Consistent with the results from the idealised forcing experi-

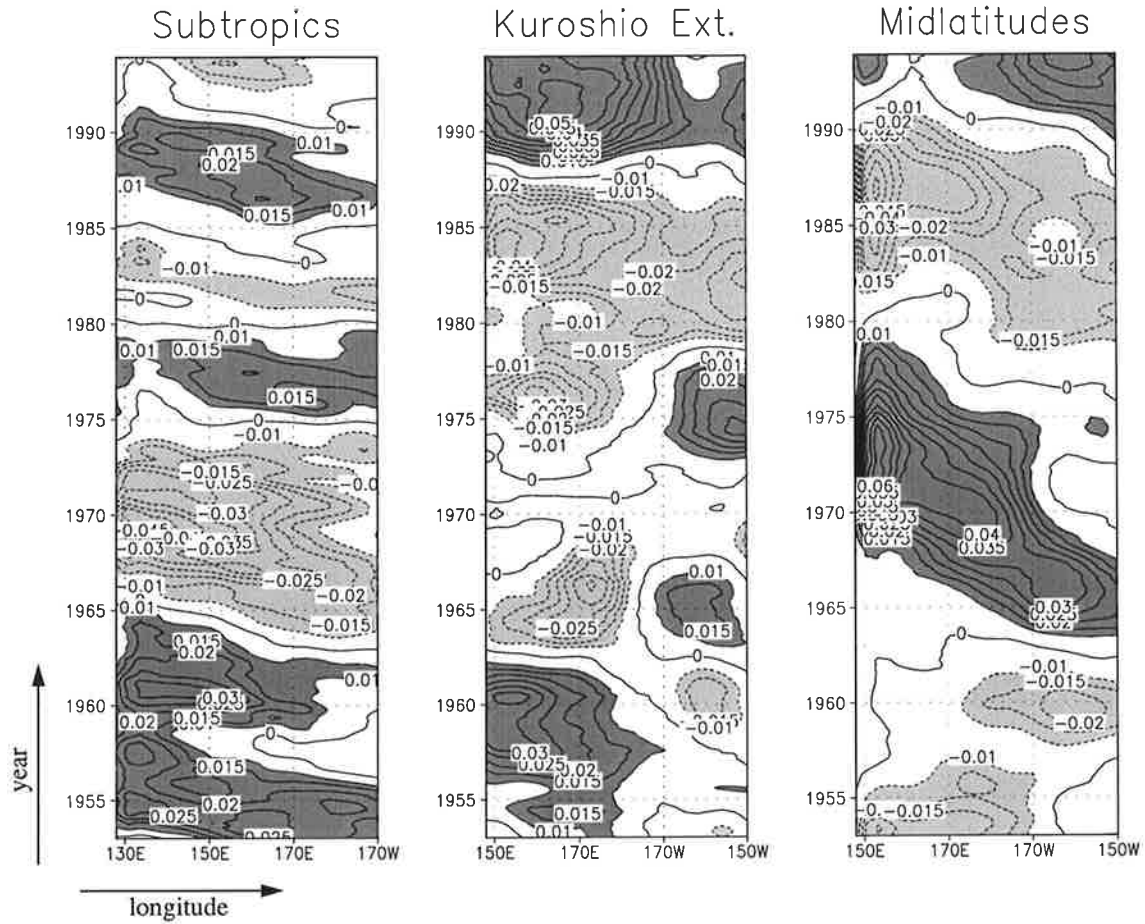


Figure 3.14: Same as Fig. 3.10 but for the COADS simulation in which the HOPE model was forced by observed atmospheric wind stress and surface heat flux anomalies. The sea level data has been smoothed with a 5 year running mean filter.

ment, EOF-1 represents the direct response and sets the conditions for the delayed response (EOF-2), which in turn is a precursor of EOF-1 with opposite sign. The lag is slightly longer than that in the simplified experiment (which by construction was five years) but is consistent with findings from Zhang and Levitus (1997) who investigated observed upper ocean temperature measurements.

Next, the predictability of the decadal upper ocean temperature changes that occurred during the late 1970s and 1980s in the central North Pacific is investigated. The most prominent long-term temperature change occurred in the North Pacific in the late 1970s (Fig. 3.14, middle panel) which is often referred to as the *1976/77 cold shift*. Subsurface cooling in the Kuroshio extension area during that time was identified in various studies (e.g. Deser et al., 1996; Miller et al., 1998a; Zhang

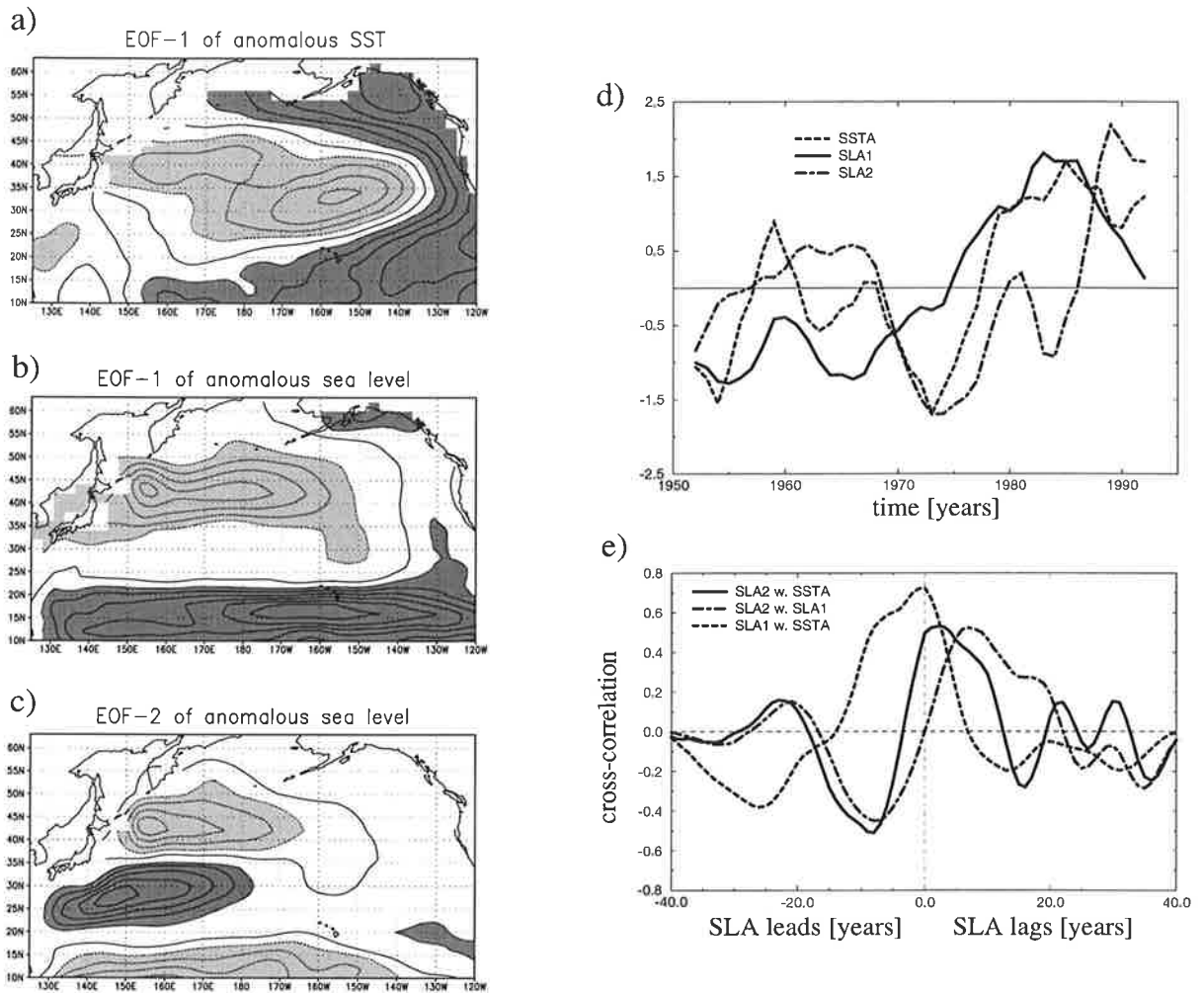


Figure 3.15: (a) First EOF of anomalous SST (explaining 45% of the total variance), (b) first EOF of anomalous sea level (43%) and (c) second EOF of anomalous sea level (19%) together with (d) the associated principle components and (e) their lag-correlation functions. The data was obtained from the COADS experiment and has been smoothed with a 5 year running mean filter.

and Levitus, 1997) and is simulated well by the HOPE model (Figs. 3.14 and 3.28). Negative sea level anomalies develop around 1965 in the eastern subtropical North Pacific and spread westward (Fig. 3.14). At the same time, anomalies of opposite sign develop in midlatitudes which also propagate westward (at lower speed as explained above).

Both anomalies can be clearly attributed to large-scale wind stress curl anomalies

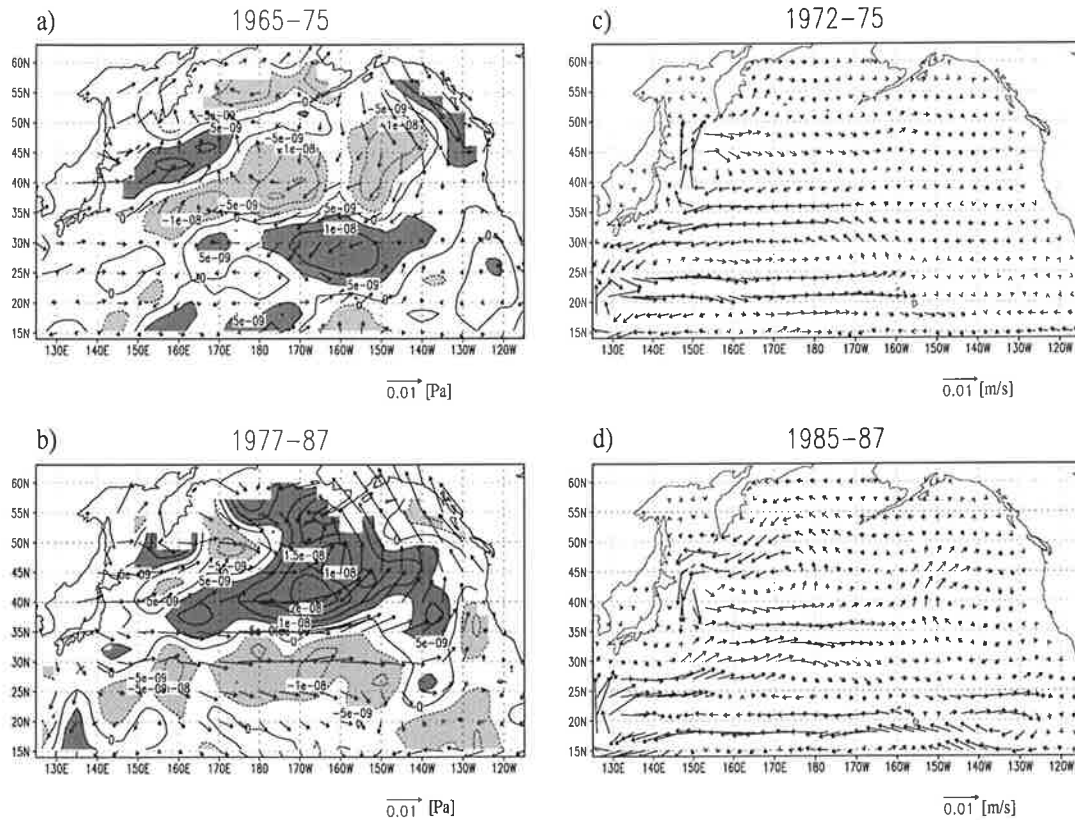


Figure 3.16: Observed wind stress [Pa] and wind stress curl [Pa/m] anomalies (deduced from the COADS data set) averaged over the periods (a) 1965-1975 and (b) 1977-1987 as well as anomalous upper ocean (0-300m) velocities [m/s] averaged over the periods (c) 1972-1975 and (d) 1985-1987 as simulated by the HOPE model in the COADS experiment.

(Fig. 3.16a) similar to those used in the previous section (Fig. 3.7). Here, it is hypothesised that they led to an adjustment of the subtropical gyre circulation (Fig. 3.15c), which caused the cooling in the Kuroshio extension region during the late 1970s. This hypothesis has recently been supported in a study by Deser et al. (1998). Based on wind stress fields from the NCAR/NCEP reanalysis project and observed upper ocean thermal fields, they have demonstrated that the Sverdrup transport along the Kuroshio extension was enhanced during the 1980s relative to the 1970s which is in very good agreement with the simulation in the COADS experiment (Fig. 3.16).

If the findings from the idealised experiments are applicable to the realistic simulation in COADS, then it should be possible to hindcast the observed cooling. The ocean model is initialised with the three dimensional temperature, salinity and

current structure simulated in December 1975 and integrated forward using the climatological surface heat fluxes and wind stresses only. Consistent with the results from the simplified experiment described in the previous section, negative sea level anomalies spread eastward along the area of the Kuroshio extension into the central North Pacific (Fig. 3.17 - middle panel).

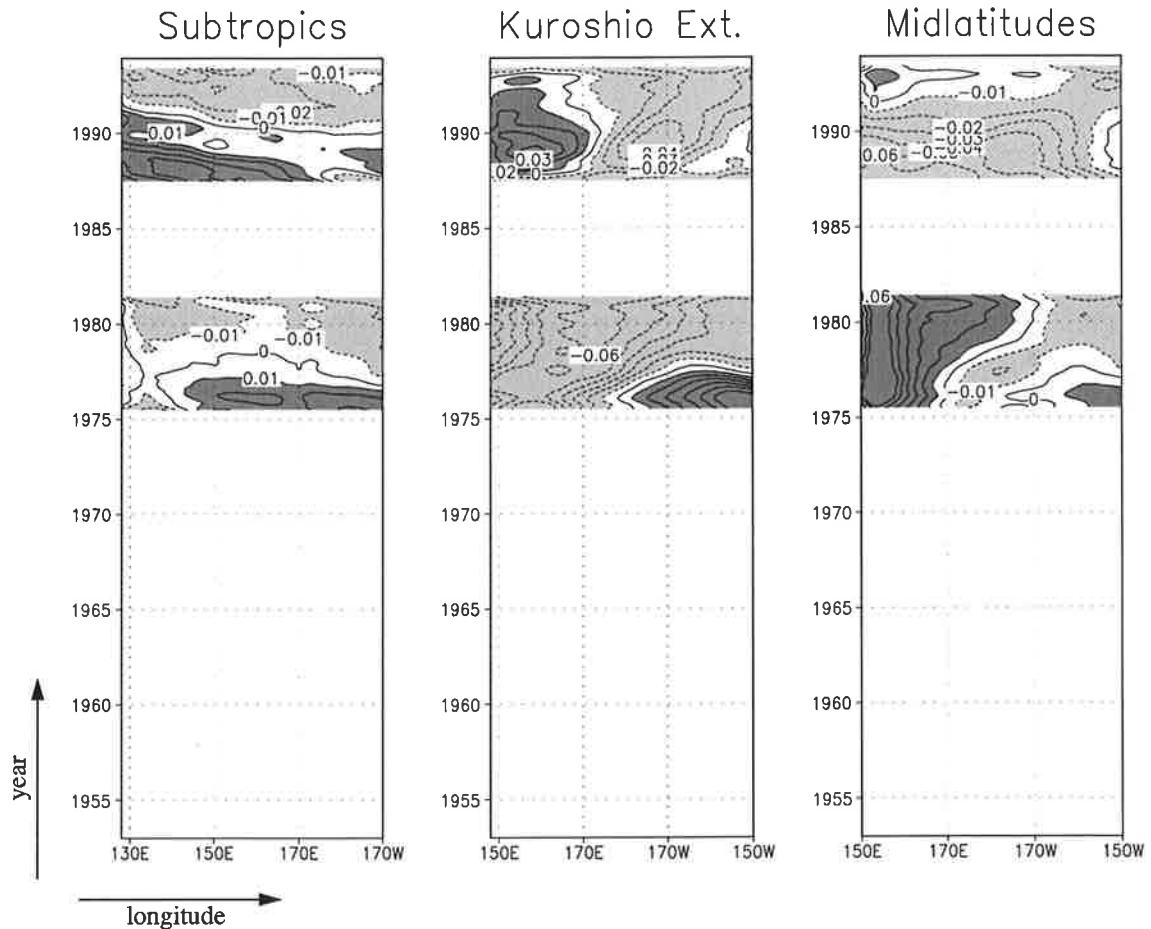


Figure 3.17: Hovmöller diagrams of sea level anomalies from ocean-only hindcasts initialised in December 1975 and December 1987 averaged over the same regions as in Fig. 3.14. The sea level data has been smoothed with a 13 months running mean filter.

These results confirm that the observed 1976/77 cooling in the central North Pacific can indeed largely be explained by the adjustment of the North Pacific Ocean circulation to decadal wind stress curl changes and to a lesser extent by local forcing. Furthermore, they demonstrate that this central North Pacific cooling was highly predictable a few years ahead.

In the late 1980s the cold conditions in the central North Pacific terminated. Again,

the conditions for the temperature change appeared to be set by wind stress anomalies (Fig. 3.16b). The resulting Rossby waves contributed in midlatitudes to the mature North Pacific cold phase during the 1980s and in the subtropics to the surrounding anomalously warm conditions (Fig. 3.14). The overall effect of the Rossby wave propagation is again a change in the gyre circulation (Fig. 3.16d). In order to investigate whether this allows to hindcast the observed warming in the central North Pacific, the HOPE model was initialised in December 1987 and integrated forward with climatological forcing only. The resulting sea level evolution is included in Fig. 3.17. The comparison with the integration using observed forcing (Fig. 3.14) reveals that in this hindcast the positive heat content anomalies in the region of the Kuroshio extension in the late 1980s are too much confined to the western part of the basin. There is, however, some indication of eastward propagation. Unlike the hindcast of the cooling in the late 1970s the sea level change in the central North Pacific is underestimated (Fig. 3.18.). This suggests that for this case the delayed wind stress response accounts for a smaller fraction of the observed change relative to the 1976/77 cooling. The second driving agent for upper ocean temperature changes are the local anomalous atmospheric variations. Decadal wind stress curl anomalies are generally small at the latitude of the Kuroshio extension (Fig. 3.7 and 3.16). They do, however, also affect the upper ocean temperature structure through anomalous Ekman currents. In fact, negative wind stress curl anomalies prevailed from 1987 until the early 1990s around 35°N (not shown). They deepened the thermocline and helped to enhance the upper ocean temperatures in the central North Pacific. This contribution is, by construction, not considered in the hindcast experiments in which changes resulting from preceding wind stress anomalies only contribute to upper ocean temperature changes. This may explain why the full extent of the warming is not captured in the simple hindcast experiment. In the case of the 1976/77 cooling the wind stress curl at the latitude of the Kuroshio extension did not show any strong anomalies that would locally affect the position of the thermocline.

In order to quantify the hindcast skill, seven additional hindcasts were initialised in December of the years 1966, 1968, 1973, 1978, 1980, 1984 and 1988. Fig. 3.18 shows central North Pacific index time series from the *COADS* simulation and the hindcasts. While the hindcasts show some skill in predicting the sea level evolution in this index region during the late 1970's and early 1980's, they largely fail during the late 1960's and early 1970's. To obtain a more complete picture of the hindcast skill, the actual skill score of the hindcast ensemble has been computed at every grid point

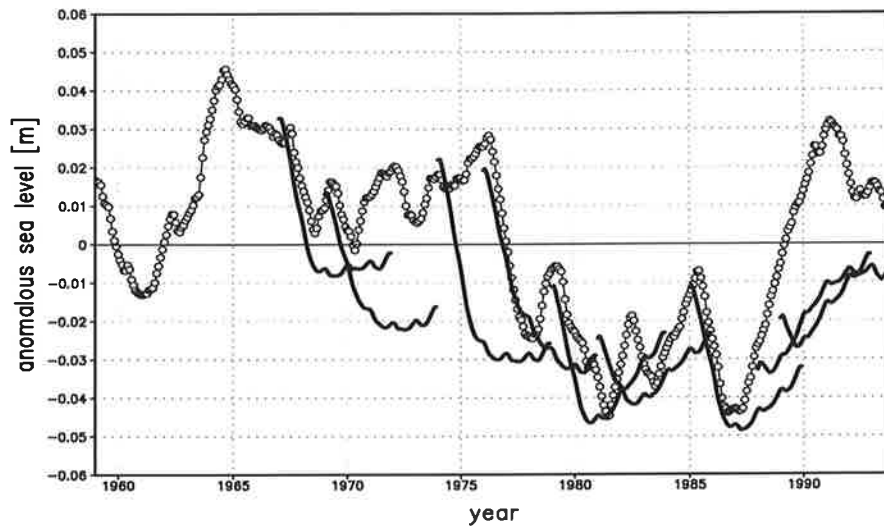


Figure 3.18: *Central North Pacific (32-42°N, 180-160°W) sea level anomalies [m] as simulated by the HOPE model in the COADS experiment (open circles) as well as in ocean-only hindcast experiments (black lines). The data was smoothed with a 13 months running mean filter.*

for different lead-times. As can be seen in Fig. 3.19, the skill of the hindcasts exceeds that of the persistence forecast over large parts of the North Pacific. In the western region the delayed response of the North Pacific gyre circulation to previous wind stress forcing provides significant skill for predicting the sea level evolution several years ahead. As discussed above, local atmospheric forcing plays an important role for sea level changes in the eastern North Pacific. Since no atmospheric feedback is included in the hindcast experiments, this limits the predictability of the system.

In summary, in this section it was shown that many of the observed features of decadal North Pacific variability can be interpreted as the North Pacific Ocean's response to decadal wind stress changes as hypothesised by Latif and Barnett (1994). In particular, the 1976/77 cooling can almost entirely be explained by the delayed response to basin-wide wind stress curl anomalies that prevailed over the previous decade. It represents a good example of how ocean dynamics enable a successful hindcast of decadal climate changes. In general, such predictability is limited by internal atmospheric variability. Such stochastic atmospheric forcing is on the other hand required to excite a weakly coupled air-sea mode and, hence, generate enhanced decadal climate variability that exceeds the variance of a red noise spectrum.

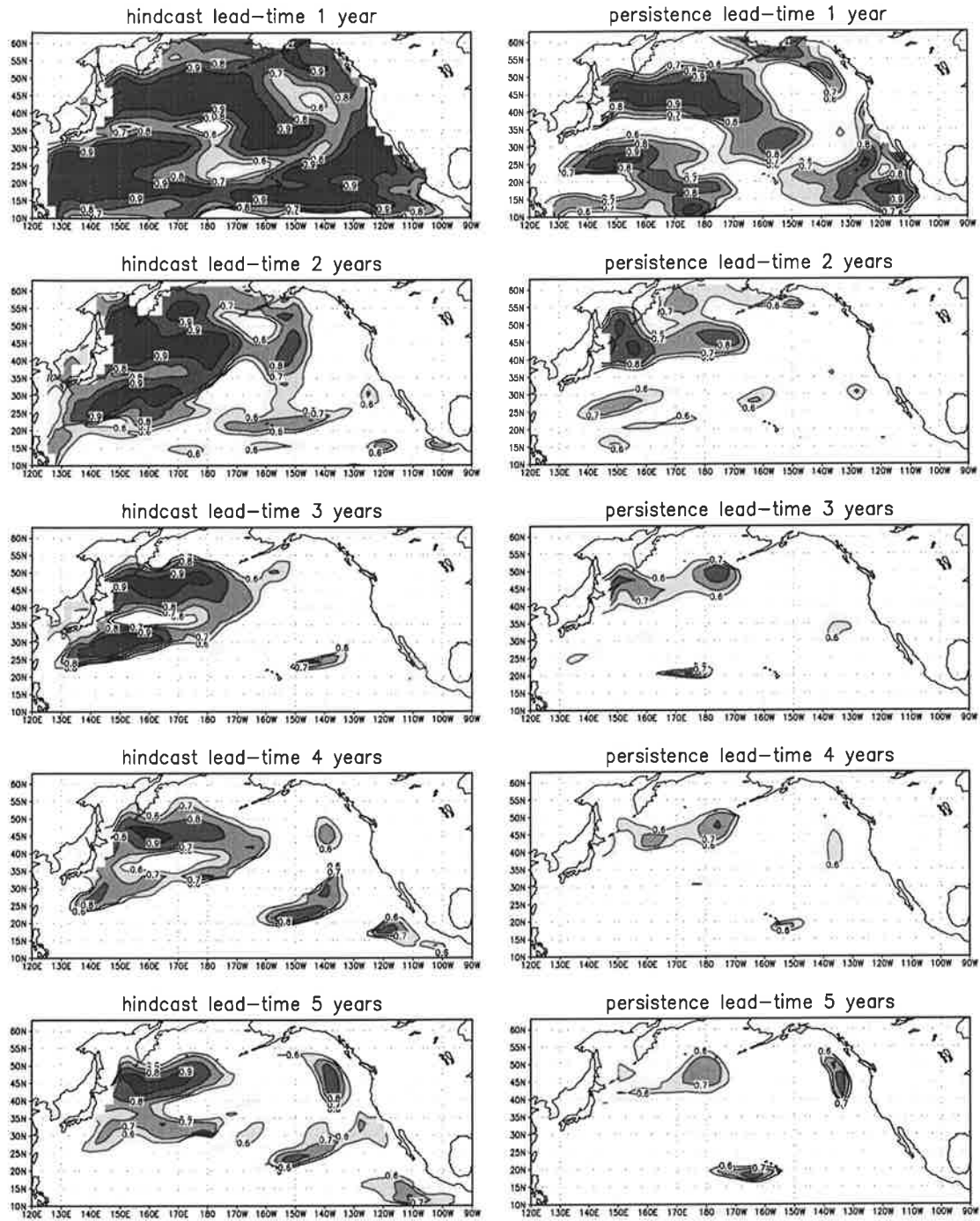


Figure 3.19: Left panels: Correlation coefficients (skill score) of annual sea level anomalies as simulated in the COADS experiment and as predicted in the hindcast experiments for different lead-times (plotted only, where significant at the 95% confidence level). Right panels: Equivalent correlation coefficients obtained by assuming persistence.

### 3.4 Decadal coupling of midlatitudinal and equatorial Pacific via the thermocline

In the previous section subtropical gyre dynamics were studied as a possible source of memory required for climate fluctuations with a decadal timescale. In this section a different hypothesis of how the ocean could contribute to the generation of enhanced North Pacific climate variability on decadal timescales will be addressed. Gu and Philander (1997) suggested that decadal SST fluctuations in midlatitudes may induce decadal changes in the equatorial ocean via an oceanic teleconnection. The resulting decadal equatorial SST anomalies could then feed back onto the atmosphere over the North Pacific. While the atmospheric feedback has been verified in the previous chapter, the effort of this section is to investigate whether the decadal coupling of northern midlatitude and equatorial Pacific via the oceanic thermocline is sufficiently strong.

Deser et al. (1996) presented the first observational evidence for subduction of decadal temperature anomalies in the North Pacific. With origins north of Hawaii, the peak anomaly appeared to move downward (approximately to 200m) and southward towards 25° N over a 10-15 year time period. So far, it has not been clearly established if these anomalies reach the equatorial thermocline. In order to study the further path of the fluid within the thermocline, vorticity provides a very useful tool.

#### 3.4.1 Maps of potential vorticity

Vorticity is of particular dynamical importance and consists of two parts. The first is the vorticity due to the rotation of the planet. The component perpendicular to the earth's surface is given by the Coriolis parameter  $f$  (*planetary vorticity*). In the broad regions of the Sverdrup regime it is many times greater than the vorticity due to the currents themselves, which make up the second part (*relative vorticity*,  $\zeta$ ). The sum of planetary and relative vorticity is called *absolute vorticity* ( $f + \zeta$ ). Cross-differentiation of the equations for the horizontal components of motion (see equation 3.8) in the absence of friction yields

$$\frac{d}{dt}(\zeta + f) = -(\zeta + f)\nabla \cdot \mathbf{v}. \quad (3.15)$$

To a first approximation, subducted fluid will tend to preserve its density as mixing across isopycnal surfaces (diapycnal mixing) is generally much weaker than mixing

on isopycnal surfaces. If one considers a layer of thickness  $h_n$  whose density is uniform (e.g. between two isopycnal surfaces in the thermocline), then the equation of continuity for the layer is

$$\frac{1}{h_n} \frac{dh_n}{dt} + \nabla \cdot \mathbf{v} = 0. \quad (3.16)$$

Combining 3.15 and 3.16 yields

$$\frac{d}{dt} \left( \frac{\zeta + f}{h_n} \right) = 0 \quad (3.17)$$

which states that the quantity  $q_n = \frac{\zeta + f}{h_n}$ , called *potential vorticity*, has to be conserved. Streamlines of subsurface flow must therefore coincide with lines of constant  $q_n$  in each layer. Luyten, Pedlosky and Stommel (1983) described in detail how the

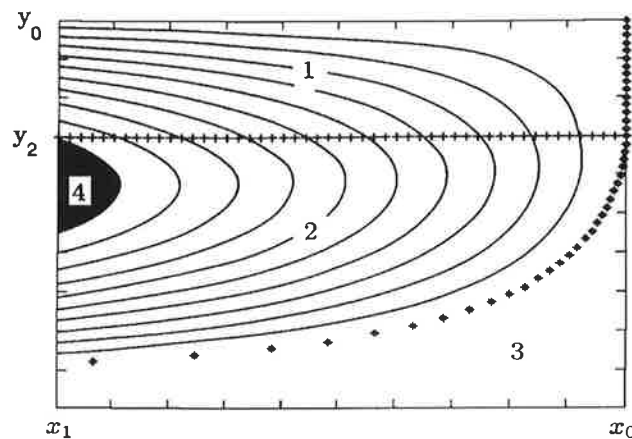


Figure 3.20: *Circulation pattern from the two-layer model of Luyten, Pedlosky and Stommel (1983).*

process of ventilation and subduction allows  $q_n$  to be determined, for each layer, in regions where the layer is shielded from Ekman pumping by warmer layers above it. They formulated a model for the ocean interior, excluding the western boundary region, the mixed layer and the Ekman layer. According to their model there are four different regions in the ocean interior (Fig. 3.20): In the pool (4) water comes from the western boundary region. North of the outcrop line ( $y_2$ ), the interior ocean is affected directly by Ekman pumping (1). The water in the ventilated region (2) has been subducted from the upper surface, and in the shadow zone (3) water is stagnant. The ventilated thermocline theory of Luyten, Pedlosky and Stommel (1983)

provides a conceptual model for the isopycnal ventilation process that was proposed much earlier by Iselin (1939). Because the potential vorticity in the Sverdrup regime can be evaluated from standard hydrographic data, it is straightforward to prepare maps of potential vorticity for particular density surfaces. The most detailed comparison between observation and the theory described above was made by Talley (1988) for the circulation of the North Pacific subtropical gyre.

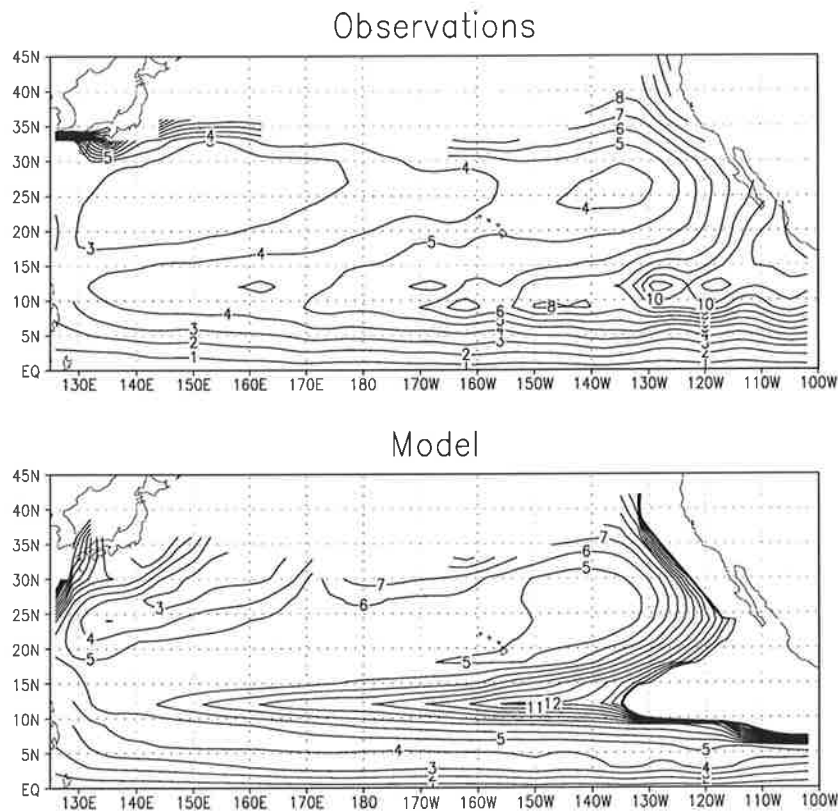


Figure 3.21: Maps of potential vorticity on the  $1025.25\text{kgm}^{-3}$  isopycnal surface as inferred from observations (Levitus, 1982) and as simulated by the HOPE model. Units are  $10^{-10}\text{m}^{-1}\text{s}^{-1}$ .

In Fig. 3.21 maps of potential vorticity on the  $1025.25\text{kgm}^{-3}$  isopycnal surface are shown. They reveal that the simple model of Luyten, Pedlosky and Stommel (1983) is remarkable successful in predicting the structure of the flow pattern. Furthermore, Fig. 3.21 demonstrates that the HOPE model reproduces the observed potential vorticity structure very well. Both, the potential vorticity maps deduced from observations and the model data, indicate that water subducting within the outcrop regions may be recirculated in the subtropical gyre or move equatorward

and contribute to the ventilation of the equatorial thermocline. Lu and McCreary (1995) note that Ekman pumping associated with the intertropical convergence zone (ITCZ) generates a potential vorticity barrier and that the subtropical water does therefore not flow to the equator through the interior ocean, but must first travel to the western boundary before reaching the equator through the Mindanao current. In a more recent study (Lu et al., 1998), they confirm this finding and furthermore identify a weak interior pathway. Lower potential vorticity in the western basin allows water masses that would not be able to directly cross the potential vorticity barrier at a particular longitude to travel southwest until reaching a region without any potential vorticity gradient to the south. Whether ventilated waters, following the potential vorticity contours along an isopycnal surface, are of relevance for the generation of decadal climate variability will be investigated next.

### 3.4.2 Propagation of diabatically forced temperature anomalies

The water exchange between the extra-tropics and the tropics has been studied in various experiments with passive tracers (Liu et al., 1994; Liu and Philander, 1995). Possible pathways along which North Pacific surface water properties could get into the tropical thermocline have been suggested. However, whether decadal North Pacific SST anomalies can have a significant impact on the thermal structure of the equatorial Pacific has not been convincingly shown yet. In order to isolate subsurface temperature anomalies that originate from diabatic surface processes from adiabatically driven anomalies that are due to anomalous Ekman pumping, a set of idealised experiments have been carried out with the HOPE model.

In selected regions, surface heat flux anomalies were superimposed onto the climatological forcing. The regions were chosen in certain windows found in the tracer study of Liu et al. (1994): Tracers subducting in the central North Pacific (just east the dateline) recirculated along the western boundary current (*recirculation window*). Tracers subducting slightly further east (around 145°W) tended to propagate westward and to flow equatorward through the Mindanao current (*western boundary exchange window*). Tracers subducting even further to the south-east (around 125°W) reached the equator through the interior of the ocean (*interior exchange window*). In each of the three idealised experiments that were performed, anomalous surface heat flux was applied in one of these windows over the course of 20 years. An overview of the experiments is given in Tab. 3.2.

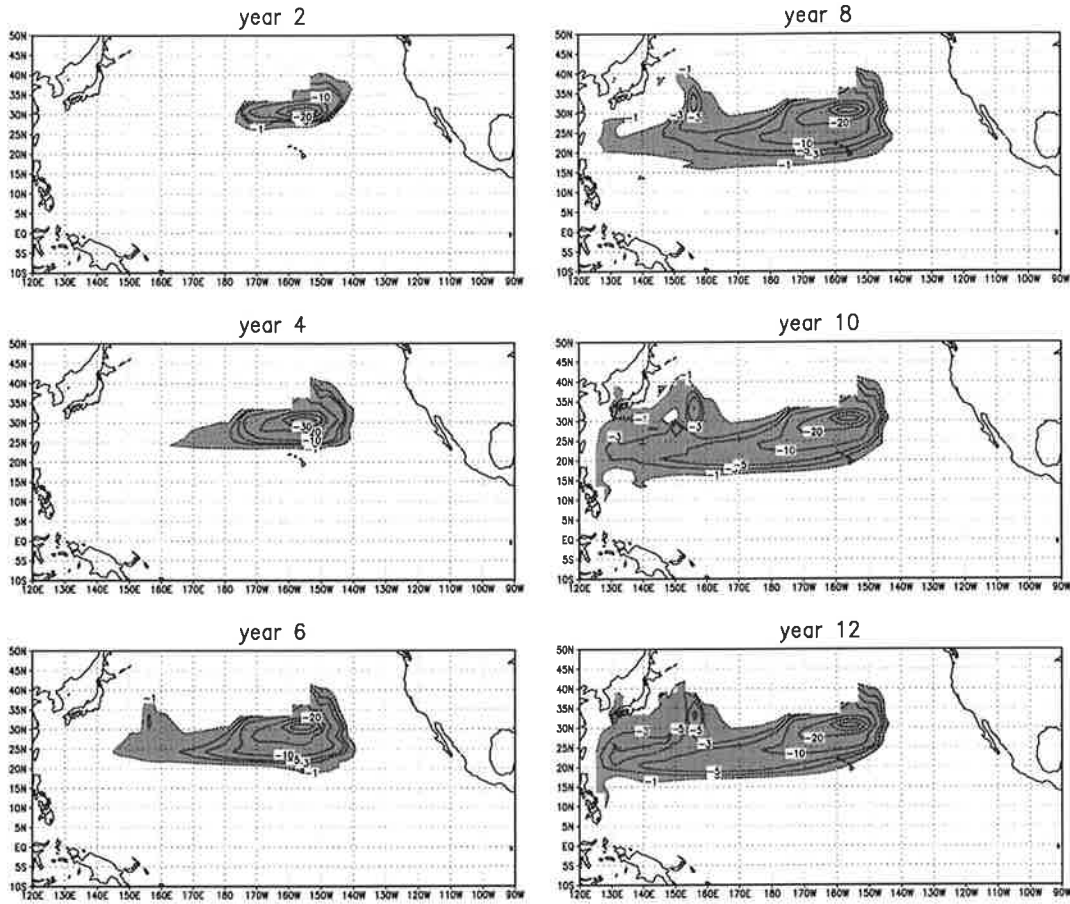


Figure 3.22: Anomalous depth [m] of the  $1025.25\text{kgm}^{-3}$  isopycnal surface in the RECIR experiment.

Experiment	region of SSTA	integration time
RECIR	$30^{\circ}\text{N} - 40^{\circ}\text{N}; 170^{\circ}\text{W} - 150^{\circ}\text{W}$	20 years
WEBOU	$22^{\circ}\text{N} - 33^{\circ}\text{N}; 150^{\circ}\text{W} - 128^{\circ}\text{W}$	20 years
INTER	$22^{\circ}\text{N} - 33^{\circ}\text{N}; 128^{\circ}\text{W} - 111^{\circ}\text{W}$	20 years

Table 3.2: Overview of the experiments discussed in this section.

The amplitude of these surface heat flux anomalies was chosen to cause SST anomalies of around  $2\text{K}$ . The goal of these experiments was to establish whether diabatically forced North Pacific temperature anomalies can propagate to the equator within the thermocline. This question is investigated by means of density. The propagation of density anomalies in the ocean can be best described by undulations

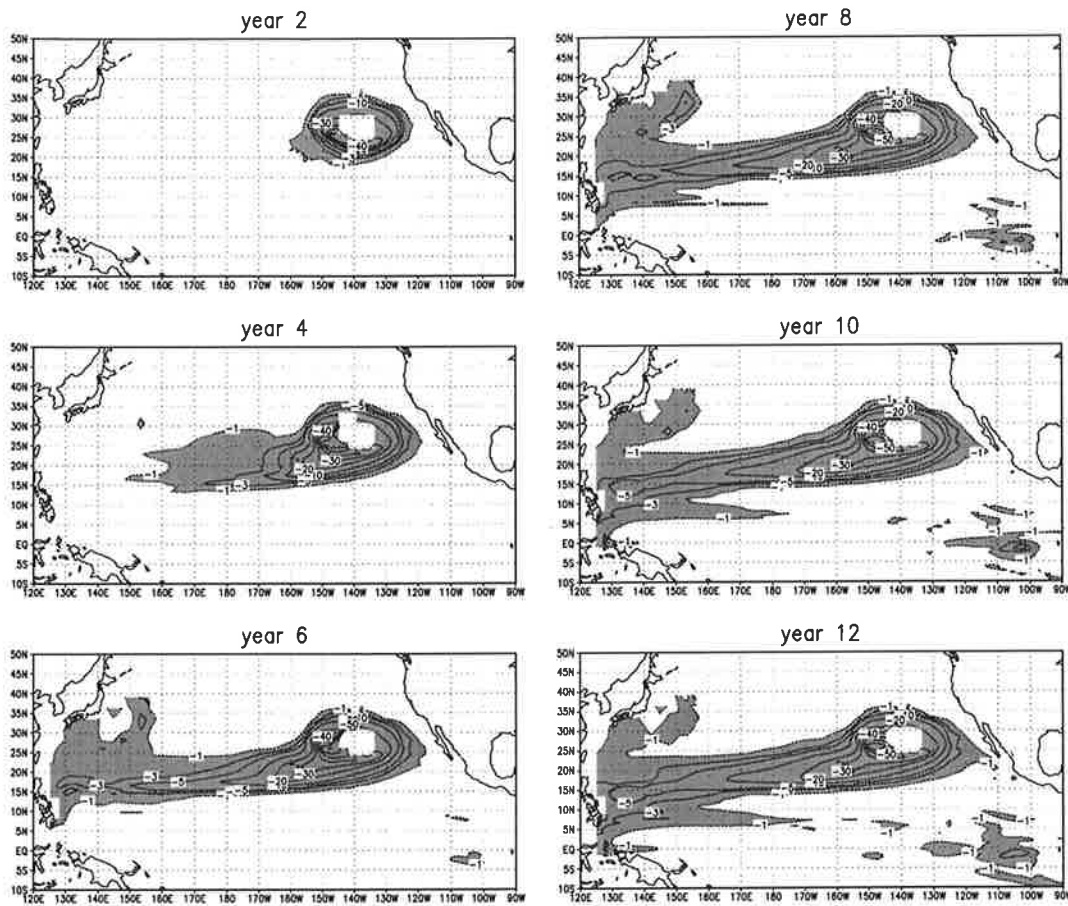


Figure 3.23: Anomalous depth [m] of the  $1025\text{kgm}^{-3}$  isopycnal surface in the WEBOU experiment.

of isopycnal surfaces, since these are aligned with the three dimensional oceanic circulation. In Fig. 3.22 depth anomalies of the  $1025.25\text{kgm}^{-3}$  isopycnal surface are shown for the first 12 years after the SST anomaly in the experiment *RECIR* was generated. A negative depth anomaly, corresponding to cold conditions appears in the central North Pacific. This spreads southwestward and reaches the western boundary after about eight years. As expected from tracer studies (Liu et al., 1994) and theoretical considerations, the anomaly does not propagate equatorward but recirculates northward.

Tracers originating from slightly further southeast, however, have been found to penetrate into the equatorial thermocline via the low-latitude western-boundary current (Liu et al., 1994). Hence, an SST anomaly was generated in that region in the *WEBOU* experiment. In Fig. 3.23 the resulting anomalies of the depth of the

$1025\text{kgm}^{-3}$  isopycnal surface are shown for the first 12 years after the SST anomaly in *WEBOU* was generated.

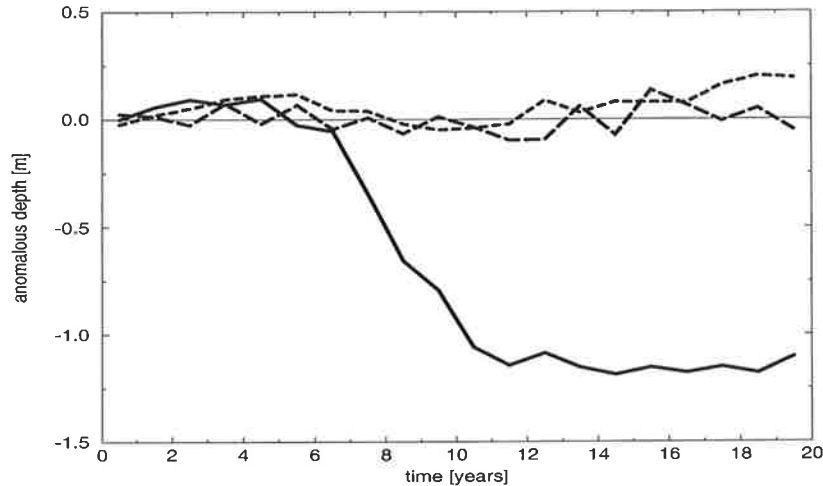


Figure 3.24: Anomalous depth [m] of the  $1025\text{kgm}^{-3}$  isopycnal surface at  $0^\circ\text{N}$ ,  $140^\circ\text{E}$  in the experiments *RECIR* (long-dashed), *WEBOU* (solid) and *INTER* (dashed).

Again, the  $1025\text{kgm}^{-3}$  isopycnal surface is shallowing first around the region of the perturbation and then also further to the southwest of it. After about six years the thermocline at the western boundary is affected. In contrast to the *RECIR* experiment, the anomaly now also spreads equatorward. It partly follows the contours of constant potential vorticity back eastward between  $5^\circ\text{N}$  and  $10^\circ\text{N}$  and partly reaches the equatorial thermocline (Fig. 3.24) via the Mindanao current at the western boundary. Following the water which joins the Mindanao current into the equatorial thermocline, it becomes evident that negative temperature anomalies can indeed be found throughout the entire equatorial thermocline at approximately the depth of the  $1025\text{kgm}^{-3}$  isopycnal surface (Fig. 3.25). Their amplitude, however, is reduced to less than 5% of the initial North Pacific SST anomaly. Furthermore, one should keep in mind that the amplitude of the idealised North Pacific SST anomaly was scaled by a factor of four compared to the typically observed amplitude of decadal North Pacific SST anomalies and that it was much more persistent than any observed SST anomaly. The evolution of temperature anomalies generated even further to the east in the North Pacific was also investigated in a further experiment (*INTER*). They were found to have no impact on the equatorial thermocline (Fig. 3.24). Overall, these idealised studies suggest that the remote impact of extratropical SST anomalies on the equatorial Pacific via the thermocline is only marginal and limited to the western boundary exchange window. Whether this is sufficient

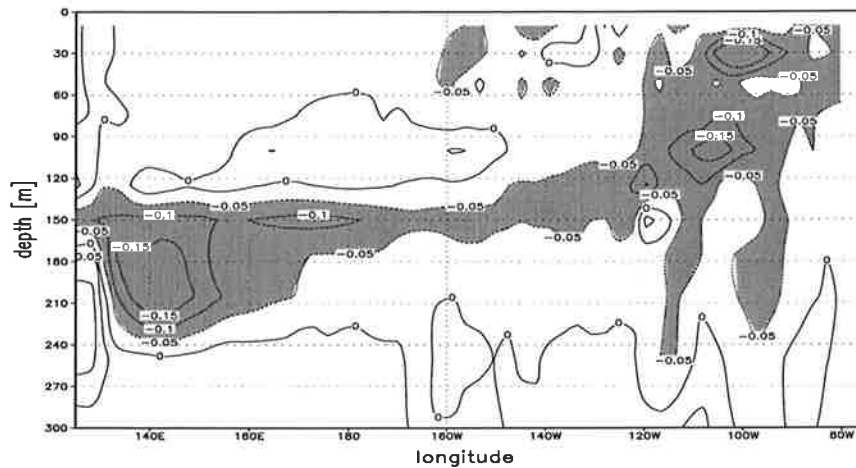


Figure 3.25: Anomalous temperature [K] in experiment WEBOU along the equator averaged over year 12 to 20 of the integration.

to explain observed decadal changes in the tropical Pacific will be investigated next.

### 3.4.3 Observational findings and sensitivity study

It has been observed that the equatorial thermocline did undergo persistent anomalous warm and cold conditions (Gu and Philander, 1997). The forecast skill of ENSO predictions also shows decadal variations (Balmaseda et al., 1995). Kirtmann and Schopf (1998) have suggested that the above findings may be related through the effectiveness of the delayed action oscillator which they found to be strong (weak) when the mean east-west thermocline slope along the equator is strong (weak). However, competing explanations have been given for the origin of observed decadal changes in the equatorial thermocline. An interpretation of historical upper ocean temperature anomalies by Zhang et al. (1998a) indicates that indeed thermal anomalies propagate from midlatitudes to the equatorial region. Using observed wind stress anomalies and simple models of the oceanic circulation, Schneider et al. (1998a) found, however, that tropical variability is mainly driven by low-latitude winds. Here, it shall be investigated by the *COADS* experiment and an additional sensitivity experiment whether propagation of midlatitudinal temperature anomalies through the thermocline or local wind stress forcing is more relevant to the observed decadal variability in the tropical Pacific.

As seen in the previous section, the propagation of thermal anomalies in the thermocline can be described by undulations of the isopycnal surfaces. The  $1025.5 \text{ kg m}^{-3}$

isopycnal surface connects the northern midlatitude and equatorial Pacific and displays enhanced low-frequency variance in the Kuroshio region around  $30^{\circ}\text{N}$  and in a broad swath that extends southwestward from the subduction region in the central North Pacific to the western subtropical and equatorial Pacific (Miller and Schneider, 1998). In this region coherent anomalies propagate from the central North

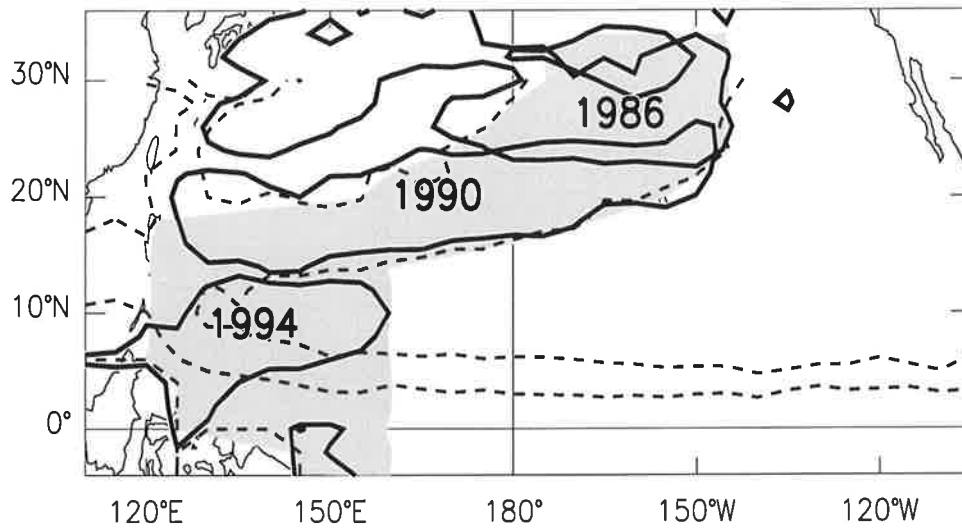


Figure 3.26: Contours of the depth anomaly of the  $1025.5\text{kgm}^{-3}$  isopycnal surface that corresponds to a shallowing of the surface by 10m. Heavy lines denote data from 1986, 1990 and 1994. Dashed lines are  $2.4$  and  $4.5 \times 10^{-10}\text{m}^{-2}\text{s}^{-1}$  isopleths of potential vorticity, and shading denotes the area of zonal averaging used in Fig. 3.28.

Pacific to the subtropics along a path of constant potential vorticity. This is shown in Fig. 3.26 for a cold anomaly in the late 1980s and early 1990s. In the *COADS* experiment, this evolution is simulated quite well as can be seen in Fig. 3.27. This figure displays also the simulation of a warm anomaly that originated in the central North Pacific in the early 1970s. Zhang et al. (1998a) have interpreted the observed evolution of the latter anomaly as propagation of subducted surface-waters through the subtropics into the tropics. They claim that it is evidence for a subsurface ocean bridge driving the formation of an equatorial SST anomaly. Fig. 3.27 indicates that this may be a misinterpretation. In the case of the warm anomaly that subducted in the early 1970s as well as in the case of the cold anomaly, thermal anomalies south of  $18^{\circ}\text{N}$  seem to be independent of the anomalies north of that latitude. This was also noted by Schneider et al. (1998a) in an analysis of observed isothermal depth. The agreement between observations and the *COADS* simulation becomes even more

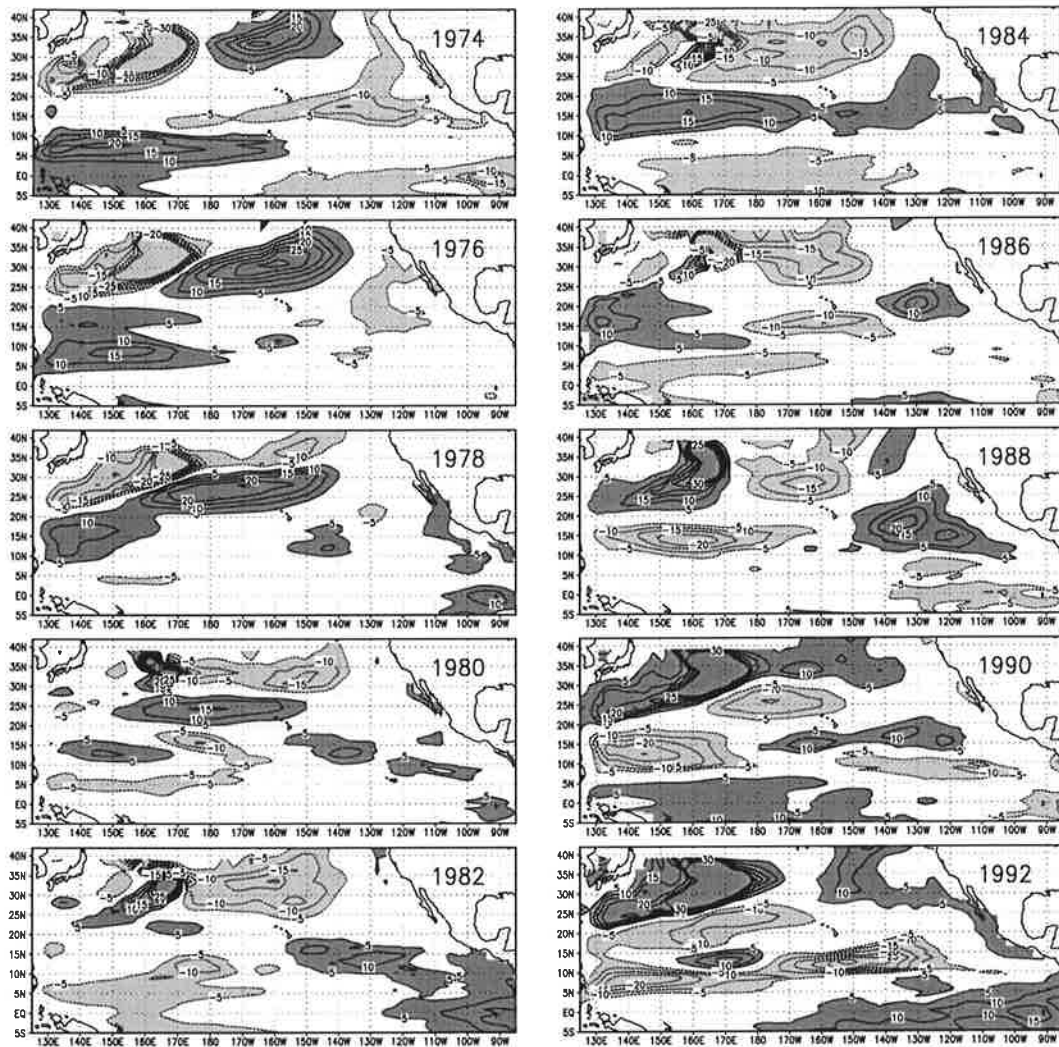


Figure 3.27: Snapshots of depth anomalies of the  $1025.5 \text{ kg m}^{-3}$  isopycnal surface as simulated in the COADS experiment. Dark shading represents positive depth anomalies.

evident in Fig. 3.28. This Hovmöller diagram shows the zonal average of depth anomalies of the  $1025.5 \text{ kg m}^{-3}$  isopycnal surface along the shaded path in Fig. 3.26. The path is marked by contours of potential vorticity (poleward of  $15^\circ\text{N}$ ) and the region of enhanced variance between the western coast of the Pacific and  $160^\circ\text{E}$ . Fig. 3.28a shows that at the same time when the positive depth anomaly originated in the central North Pacific and propagated southward to  $18^\circ\text{N}$ , an independent positive depth anomaly occupied the region south of  $18^\circ\text{N}$ . The maximum of the latter anomaly predated the arrival of the signal from the midlatitudes. The same applies to the cold anomaly that appeared in the early 1980s. Both events are

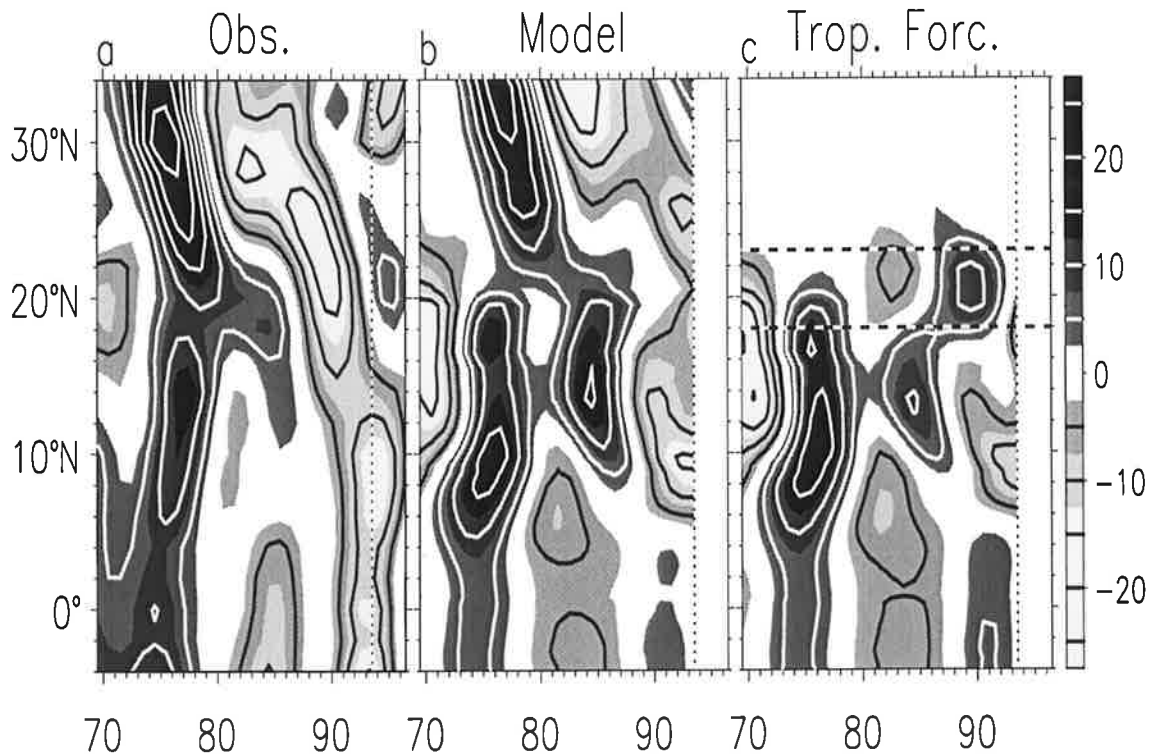


Figure 3.28: (a) Observed decadal anomalies of the depth [m] of the  $1025.5 \text{ kg m}^{-3}$  isopycnal surface zonally averaged in the shaded area shown in Fig. 3.26. (b) Same as (a) but as simulated in the COADS experiment. (c) Results from an experiment in which the anomalous forcing was restricted to the area equatorward of  $18^\circ$  as indicated by the dashed line. To avoid artificially generated curl of the wind stress a linear transition to zero anomalous forcing extended from  $18^\circ \text{ N}$  to  $23^\circ \text{ N}$ . The contour interval is 5m, light shading represents positive depth anomalies. The vertical dotted lines mark the end of the model experiment. The data has been low pass filtered to remove variance at periods shorter than 6.5 years.

simulated remarkably well in the COADS experiment (Fig. 3.28b). Differences of the simulation and observations in the tropics during the 1990s are smaller than those estimated from the differences between the COADS and the FSU (Florida State University - Stricherz et al., 1992, 1997) wind stress observations.

To test the hypothesis that low-latitude isopycnal depth anomalies are due to local wind forcing rather than due to the arrival of subducted anomalies from midlatitudes, an additional experiment was carried out in which the anomalous atmospheric forcing was restricted to the area equatorwards of  $18^\circ$  in both hemispheres. To avoid artificially generated wind stress curls, a linear transition to zero anomalous forcing extended from  $18^\circ$  to  $23^\circ$ . The resulting isopycnal depth anomalies are shown in

Fig. 3.28c. Poleward of  $18^{\circ}\text{N}$  they are indeed reduced to zero, while equatorward of  $18^{\circ}\text{N}$  the simulation is virtually unchanged. This demonstrates clearly that the observed decadal changes in the equatorial region are almost entirely caused by low-latitude wind forcing and do not depend on the inflow of thermal anomalies from midlatitudes.

Since the observed subsurface temperature record comprises only one warm and one cold event in midlatitudes, it is too short to unequivocally determine the importance of coupling of the central North Pacific and the tropics via the thermocline. The *COADS* experiment and the sensitivity experiment, however, cover additionally a period of 20 years prior to the observed record. During this period two further subduction events in midlatitudes were simulated in the *COADS* experiment (not shown). A warm anomaly subducted in the 1950s followed by a cold anomaly in the early 1960s. In the sensitivity experiment, decadal tropical and subtropical changes were again found to be independent of these midlatitudinal temperature anomalies. The above finding was confirmed by a longer time series obtained from an 140 year integration with the coupled GCM ECHO-2 (Frey et al., 1997; Venzke et al., 1998b). The model produces both realistic El Niño and decadal variability in the North Pacific. As described in detail in Schneider et al. (1998b), the simulated isopycnal depth anomalies equatorward of  $15^{\circ}\text{N}$  are independent of propagating anomalies originating in midlatitudes and are generated by the local wind stress.

In general, isopycnal depth anomalies can be generated by diabatic processes (e.g. subduction of temperature anomalies in the outcrop region) and adiabatic processes such as Ekman pumping. In the subtropics and tropics the latter seem to be dominant. Diabatically forced temperature anomalies on an isopycnal surface are compensated by salinity anomalies as density is defined to be constant. While no time-varying salinity data was available from observations and the uncoupled experiments, such are available from the simulation of the ECHO-2 model. Salinity compensated temperature anomalies are dynamically inactive, as no pressure perturbation is associated with them. Thus, they are advected like any passive tracer in the ocean. In a coordinate system that moves with the isopycnals, they are not affected by Ekman pumping. Tracing salinity compensated temperature anomalies on the  $1026\text{kgm}^{-3}$  isopycnal surface in the ECHO-2 data, Schneider et al. (1998b) found that these indeed propagate to the equatorial western Pacific. However, their magnitude south of  $10^{\circ}\text{N}$  is less than  $0.05\text{K}$ . This agrees very well with the findings from the idealised experiments in the previous section, in which isopycnal depth anomalies were purely diabatically driven.

In summary, the results presented in this section reveal that thermal anomalies in the midlatitudes of the North Pacific can only marginally affect the equatorial thermocline via oceanic teleconnections. It has been shown that decadal changes in the thermal structure of the subtropical and tropical Pacific can almost entirely be attributed to changes in low-latitude winds. Pierce et al. (1998) claim that decadal changes in these low-latitude winds can be viewed as a spatial expansion of major decadal changes in the atmospheric circulation over the North Pacific as discussed in section 2.4.

## Chapter 4

# Summary, conclusions, and outlook

This thesis has focused on aspects of ocean-atmosphere interactions that may contribute to the generation of decadal climate variability. Numerical integrations of an atmospheric and an oceanic general circulation model were carried out and analysed in order to estimate the relative importance of different processes that may generate decadal variability.

### Summary

In chapter 2 the sensitivity of the atmospheric circulation to decadal changes in the underlying SST has been estimated from an ensemble of atmospheric GCM integrations. Whether a consistent response of the extra-tropical atmosphere to decadal extra-tropical SST changes exists, and whether it yields the feedbacks required for the generation of decadal climate oscillations, are issues that are currently discussed controversially. Here, they have been addressed by using a novel approach to analyse an ensemble of six integrations of the Hadley Centre atmospheric general circulation model (HadAM1), all forced by observed SSTs and sea-ice extents for the period 1949-93. Forcing the atmospheric model by observed SSTs rather than idealised SST anomalies, as done in earlier studies, allows direct comparison with observations but leads to problems of signal-to-noise in a small ensemble. At the signal-to-noise levels typically encountered in the extra-tropics, conventional EOF analysis of the ensem-

ble mean of a variable such as MSLP yields only a good estimate of the true forced response if the internal variability is uncorrelated in space (i.e. is spatially white). This is never the case for atmospheric data. Using a pre-whitening transformation that includes information about the structure of the noise into the EOF analysis, a better estimate of the true forced response can be determined.

This method has been applied to North Atlantic low-pass-filtered seasonal mean MSLP anomalies and a common signal has been detected. This common signal could partly be attributed to oceanic changes associated with ENSO. After suppressing this influence, a detectable response remained for which the individual ensemble members track the ensemble mean consistently throughout the period considered. The same characteristic temporal evolution has also been obtained from observed MSLP data using the optimal filter pattern estimated from the ensemble of HadAM1 integrations. This indicates that it is a genuine signal and not an artefact of the analysis technique or the HadAM1 model. The best estimate of the spatial pattern associated with the dominant mode of the SST-forced variability over the North Atlantic exhibits a meridional dipole structure in MSLP and is related to a tripole of anomalous SST. Only over the tropical/subtropical Atlantic, however, does the forced response account for a substantial fraction of the total MSLP variance.

It has also been considered how the atmospheric response might feed back onto the ocean, in particular the SST tripole. If the response that has been detected is forced principally by SSTs in the Gulf Stream region, then the form of this response suggests that a change in the sign of Gulf Stream SST anomalies could be communicated through heat flux and wind stress changes to both the North Atlantic and the tropical Atlantic. This interpretation supports the idea of Grötzner et al. (1998) that a delayed negative feedback to Gulf Stream SSTs, which provides the decadal timescale for a coupled ocean-atmosphere mode of variability, could arise from oceanic advection of temperature anomalies from the tropical Atlantic. The results from the HadAM1 ensemble do not support the idea that wind stress curl anomalies are involved in the atmospheric feedback over the North Atlantic.

This is different for the atmospheric response over the North Pacific. Here, the individual ensemble members commonly exhibit a large-scale meridional wind stress curl dipole in response to both ENSO-related equatorial SST anomalies and extratropical decadal SST anomalies. Especially in winter, changes of the atmospheric circulation are dominated by ENSO. The Aleutian low deepens in response to anomalously warm tropical SSTs. In addition to the resulting wind stress curl dipole, this leads to enhanced westerly winds over the central and western North Pacific and

enhanced cooling of central North Pacific SSTs by latent and sensible surface heat fluxes.

Apart from the ENSO-related response a decadal SST-forced atmospheric signal has been detected which is independent of SST changes in the eastern equatorial Pacific. The decadal atmospheric changes are similar to those related to interannual tropical SST anomalies but also show marked differences. In association with cold central North Pacific SST anomalies low pressure extends from the Aleutian Islands equatorward over the entire central and eastern North Pacific. In parallel to the findings for the atmospheric response over the North Atlantic, the detected signal explains most MSLP variance over the tropical and subtropical regions. While a positive feedback of the atmosphere by anomalous surface heat flux changes is only marginal, a negative feedback may be provided by decadal wind stress curl anomalies.

The ocean dynamics involved in such a negative feedback have been studied in chapter 3. There, decadal wind stress anomalies have been used to force the HOPE model in the Pacific domain. The adjustment of the North Pacific to decadal wind stress curl changes is dominated by baroclinic Rossby waves. They propagate westward in the subtropics and midlatitudes in order to establish a new Sverdrup balance. This leads to changed oceanic heat transport along the Kuroshio extension, which has a strong effect on the upper-ocean temperatures of the central North Pacific. Although the westward propagating signal in the subtropics is much stronger than the one spreading eastward along the Kuroshio extension the latter is nevertheless important as it initiates a reversal of the SST tendency in the central North Pacific. However, as the atmospheric GCM integrations revealed, the required atmospheric feedbacks are not very strong. A coupled ocean-atmosphere oscillation relying on such a mechanism would therefore be strongly damped. When the HOPE model is forced by observed heat flux and wind stress data it nevertheless still exhibits during certain periods the characteristics of the gyre-adjustment. In particular, it has been shown in hindcast experiments that the cooling which occurred in the central North Pacific in the late 1970s could have been predicted from the state of the western North Pacific in the early 1970s. For the central North Pacific warming in the late 1980s, however, the hindcasts were less successful and quasi-simultaneous atmospheric circulation anomalies seem to be also relevant. In general, stochastic atmospheric variability limits the predictability but also supplies the energy to maintain damped coupled ocean-atmosphere oscillations and hence is essential for the generation of enhanced decadal climate variability.

In chapter 3 it has been shown that an alternatively suggested mechanism that relies on coupling of the midlatitudinal and equatorial Pacific via the oceanic thermocline is unlikely to contribute to enhanced decadal climate variability in the Pacific region. From observations, simulations with the HOPE model and coupled ocean-atmosphere model results it has become clear that the wind forcing in the tropics rather than the arrival of subducted anomalies from midlatitudes explains the decadal variability in the equatorial Pacific.

## Conclusions

The main objective of this thesis was to investigate how ocean-atmosphere interactions contribute to the generation of decadal climate variability in the North Atlantic and North Pacific regions. The above results lead to the following conclusions:

- (i) The estimated atmospheric response to decadal changes in North Atlantic SSTs largely fails to provide the feedbacks to the ocean that would be required in a coupled mode of decadal North Atlantic climate variability, as it was suggested by Grötzner et al. (1998). While such a coupled mode cannot be completely ruled out, the results from the HadAM1 ensemble do not provide convincing evidence to support it. Considering the high level of internal atmospheric variability, a preferred decadal timescale is more likely to result from the North Atlantic Ocean's response to stochastic atmospheric forcing. In the scenario of Saravanan and McWilliams (1998) this can be achieved by spatially coherent white noise heat flux forcing in concert with oceanic advection.
- (ii) Over the North Pacific, decadal changes in underlying SSTs cause at least a weak wind stress curl response that is consistent with the Latif and Barnett (1994) hypothesis of a coupled air-sea mode. It is, however, weak compared to ENSO-related and internal wind stress curl variability of similar spatial structure. Such a weak feedback is nevertheless sufficient to enhance the variability of the stochastically forced ocean-atmosphere system on decadal timescales. This scenario may be described by the concept of a stochastically forced weakly coupled ocean-atmosphere oscillator. The timescale is associated with the Rossby wave crossing time in the North Pacific and the subsequent change in transport along the Kuroshio extension. Furthermore, the deterministic component of decadal variability bears a potential for long-term climate

predictions in midlatitudes that could have been employed to predict e.g. the 1976/77 cooling in the central North Pacific several years in advance.

- (iii) Thermal anomalies in the midlatitudinal North Pacific can only marginally affect the equatorial thermocline via oceanic teleconnections. Instead, the changes in the thermal structure of the subtropical and tropical Pacific can almost entirely be attributed to changes in low-latitude winds. Hence, decadal variability in the North Pacific cannot be explained by a mechanism that relies on subduction of midlatitudinal temperature anomalies and their propagation to the equator in the oceanic thermocline.

## Outlook

Based on the above conclusions future work needs to be focused in four directions:

- (i) Better estimates of the true atmospheric response to decadal midlatitudinal SST anomalies have to be obtained by comparing results from ensemble integrations of different atmospheric GCMs. Preliminary results of integrations with the HadAM2 model have revealed already a higher sensitivity to North Atlantic SST forcing than found in this thesis for the HadAM1 ensemble. Insight into the physics behind SST-forced decadal atmospheric circulation anomalies could be gained from experiments that focus on the main regions of cyclogenesis.
- (ii) The predictability potential that arises from the gyre adjustment of the North Pacific needs to be more thoroughly examined in hindcast experiments that consider atmospheric feedbacks as well as stochastic atmospheric forcing. In analogy with studies of ENSO predictability, such experiments could be carried out by coupling an empirical atmosphere model to the HOPE model used in this thesis or by using fully coupled GCMs.
- (iii) Monitoring of the equatorial Pacific upper ocean temperatures with the TAO array moorings allows to identify equatorial Kelvin waves several months before they affect the eastern equatorial Pacific SSTs. An analogous monitoring system for the North Pacific does not exist yet. There are, however, satellite altimeter data (e.g. from Topex/Poseidon) available. These are currently being explored with regard to their usefulness for ENSO predictions. Once the available record is sufficiently long, it should be also possible to trace North

Pacific Rossby waves and upper ocean heat content anomalies associated with them over decadal timescales.

- (iv) The impact of the South Pacific Ocean on decadal changes in the equatorial thermocline needs to be investigated. As there exists no equivalent to the North Equatorial Countercurrent in the Southern Hemisphere (or only a very weak one), the advective influx of South Pacific water into the equatorial thermocline may provide a more important mechanism for changing the equatorial thermal structure than the influx of North Pacific water.

# Appendix A

## Derivation of the optimal detection algorithm

In section 2.2 an algorithm has been introduced which provides three diagnostics to describe the dominant spatio-temporal characteristics of a forced response in an ensemble of model integrations. Here, these diagnostics are derived:

### (i) The optimal filter

The data in the  $k^{\text{th}}$  ensemble member is represented as the matrix  $\mathbf{X}_k$ , where  $X_{ijk}$  is the data point at spatial location  $i$  ( $i = 1, \dots, \ell$ ) in year  $j$  ( $j = 1, \dots, m$ ) from ensemble-member  $k$  ( $k = 1, \dots, n$ ).

Each ensemble member  $\mathbf{X}_k$  is decomposed into an ensemble-mean component  $\mathbf{X}_M$  and the departures from that mean,  $\mathbf{X}_{Nk}$ :

$$\mathbf{X}_k = \mathbf{X}_M + \mathbf{X}_{Nk}. \quad (\text{A.1})$$

By definition, the forced response,  $\mathbf{X}_F = \mathcal{E}(\mathbf{X}_M)$ , where the expectation operator refers to an average taken over an hypothetical infinite ensemble, not over time.  $\mathbf{X}_F$  is therefore time-dependent, having the same dimensions as the  $\mathbf{X}_k$ . The ensemble mean,  $\mathbf{X}_M$ , is the best estimate available of the full spatio-temporal evolution of the forced response, but it will be heavily contaminated by noise due to the small size of the ensemble so that the highest-ranked EOF/PCs from standard EOF analysis fail to provide evidence for a consistent forced response. This, however, does not mean that no such response exists. To understand how the analysis can be improved to identify the most consistent aspects of the atmospheric response in an ensemble experiment, it helps to recall that the EOFs are the eigenvectors of the estimated

spatial covariance matrix,

$$\hat{\mathbf{C}}_M = \frac{1}{m-1} \mathbf{X}_M \mathbf{X}_M^T. \quad (\text{A.2})$$

Assuming that the ensemble members are independent and normally distributed, it is

$$\mathcal{E}(\hat{\mathbf{C}}_M) = \mathbf{C}_F + \frac{1}{n} \mathbf{C}_N, \quad (\text{A.3})$$

where  $\mathbf{C}_F$  and  $\mathbf{C}_N$  are the true (unknown) spatial covariances of the forced response and internal variability respectively. In the limit of an infinite ensemble,  $n \rightarrow \infty$  and  $\hat{\mathbf{C}}_M \rightarrow \mathbf{C}_F$ , but with small ensemble sizes the variance attributable to the forced response may well be  $O(\frac{1}{n})$  times the variance attributable to internal variability, so both terms on the RHS of equation (A.3) will have comparable magnitude, and both will contribute to the eigenvectors of  $\hat{\mathbf{C}}_M$ . The assumption that the forced response consists of a small number of spatial patterns implies that  $\mathbf{C}_F$  will be rank-deficient. The eigenvectors of  $\hat{\mathbf{C}}_M$ , or EOFs, provide an estimate of the eigenvectors of  $\mathbf{C}_F$  if and only if the internal variability is uncorrelated in space, or  $\mathbf{C}_N = \sigma^2 \mathbf{I}$ , since adding  $\sigma^2 \mathbf{I}$  to any matrix simply raises its eigenvalues by  $\sigma^2$  and does not change its eigenvectors. But the internal atmospheric variability is not uncorrelated in space. If EOFs which contain high variance in the ensemble mean also contain high variance in the deviations from that mean, one cannot expect these EOFs to be aligned even approximately with the EOFs of the true forced response (see figure 2.1). Allen and Smith (1997) resolve this problem by introducing a *pre-whitening transformation*,  $\mathbf{F}$ , such that  $\mathbf{F}^T \mathbf{C}_N \mathbf{F} \simeq n \mathbf{I}$  (i.e.  $\mathbf{F}$  removes spatial correlations, making the noise spatially white). The true covariance of internal variability,  $\mathbf{C}_N$ , is unknown, but an unbiased estimate can be obtained from the deviations from the ensemble mean:

$$\hat{\mathbf{C}}_N = \frac{1}{m(n-1)} \sum_{k=1}^n \mathbf{X}_{Nk} \mathbf{X}_{Nk}^T. \quad (\text{A.4})$$

If one defines the columns of  $\mathbf{E}_N^{(\kappa)}$  to be the  $\kappa$  highest-ranked normalised eigenvectors (EOFs) of  $\hat{\mathbf{C}}_N$ , and  $\mathbf{\Lambda}_N^{(\kappa)}$  the corresponding diagonal matrix of singular values, the pre-whitening transformation can be defined as

$$\mathbf{F} := n^{\frac{1}{2}} \mathbf{E}_N^{(\kappa)} (\mathbf{\Lambda}_N^{(\kappa)})^{-1}, \quad (\text{A.5})$$

and its transposed pseudo-inverse as

$$\mathbf{F}^{(-1)} := n^{-\frac{1}{2}} \mathbf{E}_N^{(\kappa)} \mathbf{\Lambda}_N^{(\kappa)}, \quad (\text{A.6})$$

so  $\mathbf{F}$  and  $\mathbf{F}^{(-1)}$  are  $\ell \times \kappa$  matrices. One is obliged to truncate because variance will generally be underestimated in the low-ranked EOFs of internal variability, so while

$\mathbf{F}^T \hat{\mathbf{C}}_N \mathbf{F} \equiv n\mathbf{I}$  for all  $\kappa$  by construction,  $\mathbf{F}^T \mathbf{C}_N \mathbf{F} \simeq n\mathbf{I}$  can only be expected if the analysis is confined to well-sampled EOFs. The same problem arises when optimal fingerprints are used for the detection of anthropogenic climate change (see, e.g. Hegerl et al., 1996). In order to specify the truncation level  $\kappa$  at which one avoids poorly-sampled noise EOFs while still retaining a high proportion of the expected signal, the ratio of the variance of  $\mathbf{X}_M$  and the  $\mathbf{X}_{N\kappa}$  in the directions defined by the columns of  $\mathbf{E}_N$  is computed. The truncation level  $\kappa$  is determined in a heuristic way as the number of noise EOFs for which the cumulative average of the above variance ratio stabilizes.

The pre-whitening transformation is applied to  $\hat{\mathbf{C}}_M$ , such that

$$\mathbf{C}'_M = \mathbf{F}^T \hat{\mathbf{C}}_M \mathbf{F} \simeq \mathbf{C}'_F + \mathbf{I} \quad (\text{A.7})$$

and diagonalised

$$\mathbf{C}'_M = \mathbf{E}' \mathbf{\Lambda}'^2 \mathbf{E}'^T, \quad (\text{A.8})$$

arranging the columns of  $\mathbf{E}'$ , as conventional, in order of decreasing eigenvalue. Since the transformed internal variability has equal variance in all state-space directions, the highest-ranked eigenvector  $\mathbf{e}'_1$  of  $\mathbf{C}'_M$  provides an estimate of the highest-ranked eigenvector of  $\mathbf{C}'_F$ . The elements of  $\mathbf{e}'_1$ , however, correspond to EOF indices rather than spatial locations, so it aids interpretation to convolve it with the pre-whitening transformation,  $\mathbf{F}$ , giving  $\tilde{\mathbf{E}} = \mathbf{F}\mathbf{E}'$ . The vector  $\tilde{\mathbf{e}}_1$  is the pattern which, for a given truncation, maximises the ratio of ensemble-mean variance to within-ensemble variance:

$$n \frac{\hat{\sigma}_M^2}{\hat{\sigma}_N^2} = n \frac{\tilde{\mathbf{e}}_1^T \hat{\mathbf{C}}_M \tilde{\mathbf{e}}_1}{\tilde{\mathbf{e}}_1^T \hat{\mathbf{C}}_N \tilde{\mathbf{e}}_1} = \tilde{\mathbf{e}}_1^T \hat{\mathbf{C}}_M \tilde{\mathbf{e}}_1 \quad (\text{A.9})$$

$$= \mathbf{e}'_1{}^T \mathbf{F}^T \hat{\mathbf{C}}_M \mathbf{F} \mathbf{e}'_1 = \mathbf{e}'_1{}^T \mathbf{C}'_M \mathbf{e}'_1 = \lambda_1'^2. \quad (\text{A.10})$$

where  $\hat{\sigma}_M^2$  and  $\hat{\sigma}_N^2$  are unbiased estimates of the expected variance of the ensemble mean and the internal variability. The vector  $\tilde{\mathbf{e}}_1$  is the optimal filter for characterising the forced response.

## (ii) Associated time series, or “optimised PCs”

Equivalently to conventional EOF analysis, the normalised pattern-amplitude time series of  $\tilde{\mathbf{e}}_1$  in the ensemble mean  $\mathbf{X}_M$ , is given by

$$\mathbf{p}_1 = \lambda_1'^{-1} \mathbf{X}_M^T \tilde{\mathbf{e}}_1. \quad (\text{A.11})$$

The projections of the individual ensemble members onto  $\tilde{\mathbf{e}}_1$ , are

$$\mathbf{p}_k = \lambda_1^{-1} \mathbf{X}_k^T \tilde{\mathbf{e}}_1. \quad (\text{A.12})$$

The algorithm reduces the spread between these time series and yields the optimised PC  $\mathbf{p}_1$ .

### (iii) Dominant spatial patterns

The spatial characteristics of the leading mode of the forced response are given by  $\hat{\mathbf{E}} = \mathbf{F}^{(-1)} \mathbf{E}'$ , where  $\mathbf{F}^{(-1)}$  is the transposed pseudo-inverse of the pre-whitening operator. To understand why this is the case suppose, for simplicity, that  $\mathbf{C}_F$  is of rank one (i.e. the forced response consists of a single pattern  $\mathbf{g}$ ). One can then write:

$$\mathbf{C}_F = \mathbf{g} \mathbf{g}^T \quad (\text{A.13})$$

$$\mathcal{E}(\mathbf{C}'_M) = \mathbf{F}^T \mathbf{g} \mathbf{g}^T \mathbf{F} + \mathbf{I} \quad (\text{A.14})$$

$$= \mathbf{g}' \mathbf{g}'^T + \mathbf{I}. \quad (\text{A.15})$$

Provided one has sufficient data that  $\mathbf{C}'_M \simeq \mathcal{E}(\mathbf{C}'_M)$  then because adding  $\mathbf{I}$  to any matrix does not change its eigenvectors,

$$\mathbf{e}'_1 = \alpha \mathbf{g}' \quad (\text{A.16})$$

$$= \alpha \mathbf{F}^T \mathbf{g} \quad (\text{A.17})$$

$$\hat{\mathbf{e}}_1 = \alpha \mathbf{F}^{(-1)} \mathbf{F}^T \mathbf{g} \quad (\text{A.18})$$

$$= \alpha \mathbf{E}_N^{(\kappa)} \mathbf{E}_N^{(\kappa)T} \mathbf{g}, \quad (\text{A.19})$$

where  $\alpha$  is a normalisation factor. The last equality follows from the definition of  $\mathbf{F}$  and  $\mathbf{F}^{(-1)}$ . The vector  $\hat{\mathbf{e}}_1$  therefore resembles  $\mathbf{g}$  to the extent that  $\mathbf{g}$  can be represented by the  $\kappa$  highest-ranked EOFs of the noise. The vector  $\hat{\mathbf{e}}_1$  provides an estimate of the first EOF of  $\mathbf{X}_F$ , the mean evolution of a hypothetical infinite ensemble, in the case that  $\mathbf{X}_F$  consists only of a single pattern.

A more direct way of obtaining  $\hat{\mathbf{E}}$  is by computing the patterns of regression coefficients of the original ensemble mean, filtered by projection onto the first  $\kappa$  EOFs of internal variability, onto the optimised PCs. Using the SVD of the pre-whitened ensemble mean  $\mathbf{F}^T \mathbf{X}_M = \mathbf{E}' \mathbf{\Lambda}' \mathbf{P}'^T$  and the definition of  $\tilde{\mathbf{E}}$  one can write

$$\mathbf{\Lambda}' \mathbf{P}'^T = \tilde{\mathbf{E}}^T \mathbf{X}_M. \quad (\text{A.20})$$

Pre- and post-multiplying by  $\hat{\mathbf{E}}$  and  $\mathbf{P}'$  yields

$$\hat{\mathbf{E}}\boldsymbol{\Lambda}' = \hat{\mathbf{E}}\tilde{\mathbf{E}}^T \mathbf{X}_M \mathbf{P}' \quad (\text{A.21})$$

$$= \mathbf{E}_N^{(\kappa)} \boldsymbol{\Lambda}_N \mathbf{E}' \mathbf{E}'^T \boldsymbol{\Lambda}_N^{(-1)} \mathbf{E}_N^{(\kappa)T} \mathbf{X}_M \mathbf{P}' \quad (\text{A.22})$$

$$= \mathbf{E}_N^{(\kappa)} \mathbf{E}_N^{(\kappa)T} \mathbf{X}_M \mathbf{P}' \quad (\text{A.23})$$

which, since  $\mathbf{P}'$  is orthonormal, is equivalent to regressing the filtered mean,  $\mathbf{E}_N^{(\kappa)} \mathbf{E}_N^{(\kappa)T} \mathbf{X}_M$ , onto the optimised PCs.

# Bibliography

- [1] Alexander, M. A. (1992a). Midlatitude atmosphere-ocean interaction during El Niño. Part I: The North Pacific Ocean. *J. Climate*, **5**, 944–958.
- [2] Alexander, M. A. (1992b). Midlatitude atmosphere-ocean interaction during El Niño. Part II: The Northern Hemisphere atmosphere. *J. Climate*, **5**, 959–972.
- [3] Allen, M. R., and L. A. Smith (1996). Monte Carlo SSA: Detecting irregular oscillations in the presence of colored noise. *J. Climate*, **9**, 3373–3404.
- [4] Allen, M. R., and L. A. Smith (1997). Optimal filtering in singular spectrum analysis. *Physics Letters*, **234**, 419–428.
- [5] Anderson, D. L. T., and A. E. Gill (1975). Spin-up of a stratified ocean, with applications to upwelling. *Deep-sea Res.*, **22**, 583–596.
- [6] Arakawa, A., and V. R. Lamb (1977). Computational design of the basic dynamical processes of the UCLA general circulation model. *Meth. Comput. Phys.*, **17**, 173–265.
- [7] Balmaseda, M. A., M. K. Davey, and D. L. T. Anderson (1995). Decadal and seasonal dependence of ENSO prediction skill. *J. Climate*, **8**, 2705–2715.
- [8] Barsugli, J. J., and D. S. Battisti (1998). The basic effects of atmosphere-ocean thermal coupling on midlatitude variability. *J. Atmos. Sci.*, **55**, 477–493.
- [9] Basnett, T. A., and D. E. Parker (1995). A provisional new global mean sea level pressure data set. In “*Workshop on simulations of the climate of the twentieth century using GISST*” Eds.: C. K. Folland and D. P. Rowell. Hadley Centre, *Clim. Res. Tech. Note No. 56*, 58–60.
- [10] Bjerknes, J. (1964). Atlantic air-sea interaction. *Advances in Geophysics.*, **10**, 1–82.

- [11] Bjerknes, J. (1966). A possible response of the atmospheric Hadley circulation to equatorial anomalies of the ocean temperature. *Tellus*, **18**, 820–828.
- [12] Bjerknes, J. (1969). The atmospheric teleconnections from the equatorial Pacific. *Mon. Wea. Rev.*, **97**, 163–172.
- [13] Cayan, D. R. (1992a). Latent and sensible heat flux anomalies over the northern oceans: The connection to monthly atmospheric circulation. *J. Climate*, **5**, 354–369.
- [14] Cayan, D. R. (1992b). Latent and sensible heat flux anomalies over the northern oceans: Driving the sea surface temperature. *J. Phys. Oceanogr.*, **22**, 859–881.
- [15] Cullen, M. J. P. (1993). The unified forecast/climate model. *Meteor. Mag.*, **122**, 81–94.
- [16] da Silva, A. M., C. C. Young, and S. Levitus (1994). Atlas of surface marine data. Available from NODC, NOAA/NESDIS E/OC21, Washington, D.C. 20335, USA.
- [17] Davies, J. R. , D. P. Rowell, and C. K. Folland (1998). North Atlantic and European seasonal predictability using an ensemble of multi-decadal AGCM simulations. *Int. J. of Climatology*, **17**, 1263–1284.
- [18] Deser, C., and M. L. Blackmon (1993). Surface climate variations over the North Atlantic ocean during winter: 1900-1989. *J. Climate*, **6**, 1743–1753.
- [19] Deser, C., M. A. Alexander, and M. S. Timlin (1996). Upper-ocean thermal variations in the North Pacific during 1970-1991. *J. Climate*, **9**, 1840–1855.
- [20] Deser, C., M. A. Alexander, and M. S. Timlin (1998). Evidence for a wind-driven intensification of the Kuroshio Current Extension from the 1970s to the 1980s. *J. Climate*, submitted.
- [21] Ekman, V. W. (1905). On the influence of the earth's rotation on the ocean currents. *Arkiv för Matematik, Astronomi och Fysik, Stockholm*, **2:11**, pp.52.
- [22] Frankignoul, C., and R. W. Reynolds (1983). Testing a dynamical model for mid-latitude sea surface temperature anomalies. *J. Phys. Oceanogr.*, **13**, 1131–1145.

- [23] Frankignoul, C., P. Müller, and E. Zorita (1997). A simple model of the decadal response of the ocean to stochastic wind forcing. *J. Phys. Oceanogr.*, **27**, 1523–1546.
- [24] Frey, H., M. Latif, and T. Stockdale (1997). The coupled GCM ECHO-2. Part I: The tropical Pacific. *Mon. Wea. Rev.*, **125**, 703–720.
- [25] Gates, W. L. (1992). AMIP: The atmospheric model intercomparison project. *Bull. Am. Met. Soc.*, **73**, 1962–1970.
- [26] Gill, A. E. (1982). Atmosphere-Ocean Dynamics. *Academic Press*, **30**, p.507.
- [27] Graham, N. E. (1994) Decadal-scale climate variability in the tropical and North Pacific during the 1970s and 1980s: observations and model results. *Climate Dynamics*, **10**, 135–162.
- [28] Grötzner, A., M. Latif, and T. P. Barnett (1998). A decadal climate cycle in the North Atlantic ocean as simulated by the ECHO coupled GCM. *J. Climate*, **11**, 831–847.
- [29] Gu, D., and S.G.H. Philander (1997). Interdecadal climate fluctuations that depend on exchanges between the tropics and the extra-tropics. *Science*, **275**, 805–807.
- [30] Hasselmann, K. (1976). Stochastic climate models. Part I: Theory. *Tellus*, **28**, 473–485.
- [31] Hasselmann, K. (1979). On the signal-to-noise problem in atmospheric response studies. In: “*Meteorologie over the Tropical Oceans*”, Shaw, D. B. (Ed.), *Roy. Met. Soc.*, 251–259.
- [32] Hasselmann, K. (1988). PIPs and POPs: The reduction of complex dynamical systems using Principle Interaction and Principle Oscillation Patterns. *J. Geophys. Res.*, **93**, 11015–11021.
- [33] Hasselmann, K. (1993). Optimal fingerprints for the detection of time-dependent climate change. *J. Climate*, **6**, 1957–1971.
- [34] Hegerl, G.C., H. von Storch, K. Hasselmann, U. Cubasch, B.D. Santer, and P.D. Jones (1996). Detecting Greenhouse-Gas-Induced Climate Change with an Optimal Fingerprint Method. *J. Climate*, **9**, 2281–2306.

- [35] Horel, J. D., and J. M. Wallace (1981). Planetary-scale atmospheric phenomena associated with the Southern Oscillation. *Mon. Wea. Rev.*, **109**, 813–829.
- [36] Hoskins, B. J., and D. J. Karoly (1981). The steady linear response of the spherical atmosphere to thermal and orographic forcing. *J. Atmos. Sci.*, **38**, 1179–1196.
- [37] Hurrell, J. W. (1995). Decadal trends in the North Atlantic Oscillation and relationships to regional temperature and precipitation. *Science*, **269**, 676–679.
- [38] Iselin, C. O'D. (1939). The influence of vertical and lateral turbulence on the characteristics of the waters at mid-depths. *Trans. Am. Geophys. Union*, **20**, 414–417.
- [39] James, I. N., P. M. James (1989). Ultralow-frequency variability in a simple circulation model. *Nature*, **342**, 53–55.
- [40] Kirtmann, B. P., and P. S. Schopf (1998). Decadal variability in ENSO predictability and prediction. *J. Climate*, *in press*.
- [41] Kushnir, Y., I. M. Held (1996). Equilibrium atmospheric response to North Atlantic SST anomalies. *J. Climate*, **9**, 1208–1220.
- [42] Latif, M. and T. P. Barnett (1994). Causes of decadal climate variability over the North Pacific and North America. *Science*, **266**, 634–637.
- [43] Latif, M., and T. P. Barnett (1996). Decadal climate variability over the North Pacific and North America - Dynamics and predictability. *J. Climate*, **9**, 2407–2423.
- [44] Latif, M., R. Kleemann, and C. Eckert (1997). Greenhouse warming, decadal variability or El Niño? An attempt to understand the anomalous 1990s. *J. Climate*, **10**, 2221–2239.
- [45] Lau, N. C., and M. J. Nath (1994). A modeling study of the relative roles of the tropical and extratropical SST anomalies in the variability of the global ocean-atmosphere system. *J. Climate*, **7**, 1184–1207.

- [46] Lean, J., J. Beer, and R. Bradley (1995). Reconstruction of solar irradiance since 1600: Implications for climate change. *Geophys. Res. Lett.*, **22**, 3195–3198.
- [47] Lemke, P., E. W. Trinkl, and K. Hasselmann (1980). Stochastic dynamic analysis of polar sea ice variability. *J. Phys. Oceanogr.*, **10**, 2100–2120.
- [48] Levitus, S. (1982). Climatological atlas of the worlds ocean. *NOAA, prof. paper no. 13, US Govt. printing office, Washington D.C., 173 pp, 17 microfiche.*
- [49] Liu, Z., S. G. H. Philander, and R. C. Pacanowski (1994). A GCM study of the tropical-subtropical upper-ocean water exchange. *J. Phys. Oceanogr.*, **24**, 2606–2623.
- [50] Liu, Z., and S. G. H. Philander (1995). How different wind-stress pattern affect the tropical-subtropical circulations of the upper ocean. *J. Phys. Oceanogr.*, **25**, 449–462.
- [51] Lorenz, E. N. (1956). Empirical Orthogonal Functions and Statistical Weather Prediction. *Scientific Report No.1, Massachusetts Institute of Technology; Department of Meteorology.*
- [52] Lorenz, E. N. (1963). Deterministic nonperiodic flow. *J. Atmos. Sci.*, **20**, 130–141.
- [53] Lu, P., and J. P. McCreary (1995). Influence of the ITCZ on the flow of thermocline water from the subtropical to the equatorial Pacific Ocean. *J. Phys. Oceanogr.*, **25**, 3076–3088.
- [54] Lu, P., J. P. McCreary, and B. A. Klinger (1998). Meridional circulation cells and the source water of the Pacific equatorial undercurrent. *J. Phys. Oceanogr.*, **28**, 62–84.
- [55] Luyten, J. R., J. Pedlosky and H. Stommel (1983). The ventilated thermocline. *J. Phys. Oceanogr.*, **13**, 292–309.
- [56] Mikolajewicz, U. and E. Maier-Reimer (1990). Internal secular variability in an ocean general circulation model. *Climate Dynamics*, **4**, 145–156.

- [57] Miller, A. J., D. R. Cayan, T. P. Barnett, N. E. Graham, and J. M. Oberhuber (1994). Interdecadal variability of the Pacific Ocean: model response to observed heat flux and wind stress anomalies. *Climate Dynamics*, **9**, 287–302.
- [58] Miller, A. J., D. R. Cayan, and W. B. White (1998a). A westward-intensified decadal change in the North Pacific thermocline and gyre-scale circulation. *J. Climate*, *in press*.
- [59] Miller, A. J., and N. Schneider (1998b). Interpreting the observed patterns of Pacific Ocean decadal variations. *Proceedings, Aha' Hulikoa Hawaiian Winter Workshop*, *in press*.
- [60] Montgomery, R. B. (1938). Circulation in upper layers of southern North Atlantic Ocean deduced with use of isentropic analysis. *Pap. Phys. Oceanogr. Meteorol.*, **2**, pp.55.
- [61] Münnich, M., M. Latif, S. Venzke, and E. Maier-Reimer (1998). Decadal oscillations in a simple coupled model. *J. Climate*, **11**, 3309–3319.
- [62] Neelin, J. D., M. Latif, and F.-F. Jin (1994). Dynamics of coupled ocean-atmosphere models: The tropical problem. *Ann. Rev. Fluid Mech.*, **26**, 617–659.
- [63] Palmer, T. N., and Z. Sun (1985). A modelling and observational study of the relationship between sea surface temperature in the northwest Atlantic and the atmospheric general circulation. *Quart. J. Roy. Met. Soc.*, **111**, 947–975.
- [64] Palmer, T. N., and D. L. T. Anderson (1994). The prospects for seasonal forecasting - a review paper. *Quart. J. Roy. Met. Soc.*, **120**, 755–793.
- [65] Parker, D. E., C. K. Folland, A. Bevan, M. N. Ward, M. Jackson, and F. Maskell (1995). Marine surface data for analysis of climate fluctuations on interannual to century time-scales. In: *"Natural Climate Variability on Decadal to Century Time scales."* edited by D. G. Martinson et al., National Academy Press., 241–250.
- [66] Peng, S., W. A. Robinson, and M. P. Hoerling (1997) The modeled atmospheric response to midlatitude SST anomalies and its dependence on background circulation states. *J. Climate*, **10**, 971–987.

- [67] Philander, S. G. H. (1990). El Niño, La Niña, and the Southern Oscillation. *Academic Press, San Diego*, pp. 293.
- [68] Phillips, T. J. (1994). A summary documentation of the AMIP models. *PCMDI Report No.18, Lawrence Livermore National Lab. Calif.*
- [69] Pierce, D. W., T. P. Barnett, and M. Latif (1998). Connections between the Pacific Ocean Tropics and Midlatitudes on decadal time scales. *J. Climate*, submitted.
- [70] Pitcher, E. J., M. L. Blackmon, and S. Muñoz (1988). The effect of North Pacific temperature anomalies on the January climate in a general circulation model. *J. Atmos. Sci.*, **45**, 173–188.
- [71] Renshaw, A. C., D. P. Rowell, and C. K. Folland (1998). ENSO responses and low frequency weather variability in the North Pacific/American sector 1943-93. *J. Climate*, **11**, 1073–1093.
- [72] Robertson, A. W., M. Ghil, and M. Latif (1998). Interdecadal Changes in Atmospheric Low-Frequency Variability with and without Boundary Forcing. *J. Atmos. Sci.*, submitted.
- [73] Roeckner, E., K. Arpe, L. Bengtsson, L. Dümenil, E. Kirk, F. Lunkeit, M. Ponater, B. Rockel, R. Sausen, S. Schubert, and M. Windelband (1992). Simulation of the present day climate with the ECHAM model: Impact of model physics and resolution. *Report No. 93, Available from MPI für Meteorologie, Bundesstr.55, 20146 Hamburg, Germany.*
- [74] Rogers, J.C. (1990). Patterns of low-frequency monthly sea level pressure variability (1899-1986) and associated wave cyclone frequencies. *J. Climate*, **3**, 1364–1379.
- [75] Robock, A. D., and J. Mao (1995). A volcanic signal in surface temperature observations. *J. Climate*, **8**, 1086–1103.
- [76] Ropelewski, R. W., and M. S. Halpert (1989). Precipitation patterns associated with the high index of the Southern Oscillation. *J. Climate*, **2**, 594–614.
- [77] Rowell, D. P. (1998). Assessing potential seasonal predictability with an ensemble of multi-decadal GCM simulations. *J. Climate*, **11**, 109–120.

- [78] Saravanan, R. and J. C. Mc Williams (1998) Advective ocean-atmosphere interaction: an analytical stochastic model with implications for decadal variability. *J. Climate*, **11**, 165–188.
- [79] Schneider, N., A. J. Miller, M. A. Alexander, and C. Deser (1998a). Subduction of Decadal North Pacific Temperature Anomalies: Observations and Dynamics. *J. Phys. Oceanogr.*, *in press*.
- [80] Schneider, N., S. Venzke, A. J. Miller, D. W. Pierce, T. P. Barnett, C. Deser, and M. Latif (1998b). Decadal coupling of the northern mid-latitude and equatorial Pacific Ocean via the thermocline?. *Nature*, *submitted*.
- [81] Stommel, H. (1948). The westward intensification of wind-driven currents. *Transactions American Geophysical Union*, **29**, 202–206.
- [82] Stommel, H. (1979). Determination of water mass properties of water pumped down from the Ekman layer to the geostrophic flow below. *Proc. Nat. Acad. Sci., USA*, **76**, 3051–3055.
- [83] Stricherz, J. N., J. J. O'Brien, and D. M. Legler (1992). Atlas of Florida State University tropical winds for TOGA 1976-1985. *The Florida State University, Tallahassee*, 261 pp.
- [84] Stricherz, J. N., J. J. O'Brien, and D. M. Legler (1997). TOGA pseudo-stress atlas 1986-1994. Volume II: Pacific Ocean. *The Florida State University, Tallahassee*, 158 pp.
- [85] Suarez, M.J., and P. S. Schopf (1988). A delayed action oscillator for ENSO. *J. Atmos. Sci.*, **45**, 3283–3287.
- [86] Sutton, R. T., and M. R. Allen (1997). Decadal predictability of North Atlantic sea surface temperature and climate. *Nature*, **388**, 563–567.
- [87] Sverdrup, H. U. (1947). Wind-driven currents in a baroclinic ocean, with applications to the equatorial currents in the eastern Pacific. *Proc. Natl. Acad. Sci. U.S.A.*, **33**, 318–326.
- [88] Talley, L. D. (1988). Potential vorticity distribution in the North Pacific. *J. Phys. Oceanogr.*, **18**, 89–106.

- [89] Tourre, Y. M., Y. Kushnir, and W. B. White (1998). Evolution of interdecadal variability in SLP, SST and upper ocean temperatures over the Pacific ocean. *J. Phys. Oceanogr.*, submitted.
- [90] Trenberth, K. E. and J. W. Hurrell (1994). Decadal atmosphere-ocean variations in the Pacific. *Clim. Dynamics*, **9**, 303–319.
- [91] Trenberth, K. E., and T. J. Hoar (1996). The 1990-1995 El Niño-Southern Oscillation event - The longest on record. *Geophys. Res. Lett.*, **23**, 57–60.
- [92] UNESCO (1983). Algorithms for the computation of fundamental properties of seawater. *UNESCO Technical Papers in Marine Science*, **44**.
- [93] Venzke, S., M. R. Allen, R. T. Sutton, and D. P. Rowell (1998a). The atmospheric response over the North Atlantic to decadal changes in sea surface temperature. *J. Climate*, accepted.
- [94] Venzke, S., M. Latif, and A. Villwock (1998b). The coupled GCM ECHO-2. Part II: Indian Ocean response to ENSO. *J. Climate*, submitted.
- [95] von Storch, H., G. Bürger, R. Schnur, and J.-S. von Storch (1995). Principle Oscillation Patterns: A review. *J. Climate*, **8**, 377–400.
- [96] Wang, M. C., and G. E. Uhlenbeck (1945). On the theory of the Brownian motion. *Rev. Mod. Phys.*, **17**, 323–342.
- [97] White, W.B., J. Lean, D.R. Cayan, and M.D. Dettinger (1997). Response of global upper ocean temperature to changing solar irradiance. *J. Geophys. Res.*, **102**, 3255–3266.
- [98] Willmott, C. J., C. M. Rowe, and Y. Minz (1985). A global archive of land cover and soils data for use in general circulation models. *J. Climatol.*, **5**, 119–143.
- [99] Wolff, J.-O., E. Maier-Reimer, and S. Legutke (1997). *HOPE, The Hamburg Ocean Primitive Equation Model. Technical Report No.10 available from DKRZ, Bundesstr.55, 20146 Hamburg, Germany.*
- [100] Xu, W., T. P. Barnett, and M. Latif (1998). Decadal variability in the North Pacific as simulated by a hybrid coupled model. *J. Climate*, **11**, 297–311.

- [101] Yin, F. L., and E. S. Sarachik (1995). On interdecadal thermohaline oscillations in a sector ocean general circulation model: Advective and convective processes. *J. Phys. Oceanogr.*, **25**, 2465-2484.
- [102] Zhang, R. H., and S. Levitus (1997). Structure and cycle of decadal variability of upper ocean temperature in the North Pacific. *J. Climate*, **10**, 710-727.
- [103] Zhang, R. H., L. M. Rothstein, and A. J. Busalacchi (1998). Origin of Upper-Ocean Warming and El Niño changes on Decadal scales in the Tropical Pacific. *Nature*, **391**, 879-883.